Fall 2016

Novel dictionary learning algorithm for accelerating multi-dimensional MRI applications

Sampada Vasant Bhave
University of Iowa

NOVEL DICTIONARY LEARNING ALGORITHM FOR ACCELERATING MULTI-DIMENSIONAL MRI APPLICATIONS

by

Sampada Vasant Bhave

A thesis submitted in partial fulfillment of the
requirements for the Doctor of Philosophy
degree in Electrical and Computer Engineering
in the Graduate College of
The University of Iowa

December 2016

Thesis Supervisor: Associate Professor Mathews Jacob

Graduate College
The University of Iowa
Iowa City, Iowa

CERTIFICATE OF APPROVAL

PH.D. THESIS

This is to certify that the Ph.D. thesis of

Sampada Vasant Bhave

has been approved by the Examining Committee for the thesis requirement for the Doctor of Philosophy degree in Electrical and Computer Engineering at the December 2016 graduation.

Thesis Committee: _____
Mathews Jacob, Thesis Supervisor

_____
Vincent A Magnotta

_____
Daniel Thedens

_____
Milan Sonka

_____
Raghuraman Mudumbai

ACKNOWLEDGEMENTS

I would like to express my gratitude towards my advisor Professor Mathews Jacob for this guidance, motivation and encouragement throughout the four years. I sincerely thank him for his support and patience. His technical advice has taught me innumerable lessons and insights about academic research in general.

I am grateful to my committee members: Dr. Vincent Magnotta, Dr. Dan Thedens, Dr. Milan Sonka and Dr. Raghuraman Mudumbai for their time, effort and valuable insights on my research.

I would also like to thank Dr. John Newell for their clinical collaborations and for his always encouraging words during our meetings. This clinical insights always helped me see the bigger picture of my research.

I would like to thank the MR research technologists at Magnetic resonance research facility - Marla kleingartner, Autumn Craig and Kori Rich for their help with the MR scans.

I am also thankful to my present and past labmates in Computational Biomedical imaging group - Sajan Goud Lingala, Yue Hu, Xuan Zhou, Ipshita Bhattacharya, Sunrita Poddar, Chen Cui, Arvind Balachandrasekaran, Sampurna Biswas, Greg Ongie, Yasir Mohsin, Merry Mani for a very friendly and collaborative environment in the lab.

I would like to specially thank my rooommate Namita Sawant for bearing me and my frustrations for over three crucial years of my PhD. I would like to thank my friends in Iowa city - Radhika Anaredy, Parin Shah, Vivek Sardeshmukh, Chaitanya

Kulkarni, Raghu Muddasani, Sandeep Bodduluri, Rahil Sharma, Preethi Issac and Shivangi Inamdar for all the fun times and for making 6 years in Iowa very very memorable and easy going.

There is no way I would be doing research and a PhD without the love, immense patience and support of my parents. They have always encouraged me and stood by me through thick and thin.

ABSTRACT

The clinical utility of multi-dimensional MRI applications like multi-parameter mapping and 3D dynamic lung imaging is limited by long acquisition times. Quantification of multiple tissue MRI parameters has been shown to be useful for early detection and diagnosis of various neurological diseases and psychiatric disorders. They also provide useful information about disease progression and treatment efficacy. Dynamic lung imaging enables the diagnosis of abnormalities in respiratory mechanics in dyspnea and regional lung function in pulmonary diseases like chronic obstructive pulmonary disease (COPD), asthma etc. However, the need for acquisition of multiple contrast weighted images as in case of multi-parameter mapping or multiple time points as in case of pulmonary imaging, makes it less applicable in the clinical setting as it increases the scan time considerably. In order to achieve reasonable scan times, there is often tradeoffs between SNR and resolution.

Since, most MRI images are sparse in known transform domain; they can be recovered from fewer samples. Several compressed sensing schemes have been proposed which exploit the sparsity of the signal in pre-determined transform domains (eg. Fourier transform) or exploit the low rank characteristic of the data. However, these methods perform sub-optimally in the presence of inter-frame motion since the pre-determined dictionary does not account for the motion and the rank of the data is considerably higher. These methods rely on two step approach where they first estimate the dictionary from the low resolution data and using these basis functions they estimate the coefficients by fitting the measured data to the signal model.

The main focus of the thesis is accelerating the multi-parameter mapping and 3D dynamic lung imaging applications to achieve desired volume coverage and spatio-temporal resolution. We propose a novel dictionary learning framework called the Blind compressed sensing (BCS) scheme to recover the underlying data from undersampled measurements, in which the underlying signal is represented as a sparse linear combination of basic functions from a learned dictionary. We also provide an efficient implementation using variable splitting technique to reduce the computational complexity by up to 15 fold. In both multi- parameter mapping and 3D dynamic lung imaging, the comparisons of BCS scheme with other schemes indicates superior performance as it provides a richer presentation of the data. The reconstructions from BCS scheme result in high accuracy parameter maps for parameter imaging and diagnostically relevant image series to characterize respiratory mechanics in pulmonary imaging.

PUBLIC ABSTRACT

Multi-dimensional MRI is a promising imaging modality. Since it is radiation free modality, it has advantages over other imaging modalities like computed tomography (CT), X-rays, etc. MRI acquisition is inherently slow due to hardware limitations that leads to peripheral nerve stimulation. The acquisition speed of MRI limits its diagnostic ability in clinics.

The quantification of multiple tissue parameters from MRI datasets is emerging as a powerful tool for tissue characterization. Parameters such as proton density, longitudinal and transverse relaxation times (denoted by T1 and T2), relaxation times in the rotating frame (T1ρ and T2ρ), as well as diffusion have been shown to be useful in diagnosis of various neurological diseases. Although a single parameter may be sensitive to a number of tissue properties of interest, it may not be specific. Acquiring additional parameters can improve the specificity.

Dynamic lung imaging enables the diagnosis of the abnormalities to the active and passive components involved in respiratory pumping including diaphragm paresis or paralysis, abnormal chest wall mechanics, and muscle weakness, resulting from neuromuscular, pulmonary, or obesity related disorders in dyspnea. It is a powerful non-invasive, non-contrast tool to access abnormalities in regional lung function in pulmonary diseases like chronic obstructive pulmonary disease (COPD), asthma, etc.

However, the need for acquisition of multiple contrast weighted images as in case of multi-parameter mapping or multiple time points as in case of pulmonary imaging increase the scan time considerably. The most common approach is to collect

fewer samples. Most MRI images are sparse in some transform domain. In order words they have only a few non-zero coefficients and hence they can be recovered from fewer samples.

Several researchers have developed various schemes for recovering the underlying data with fewer samples. However, they sub-optimal in multi-parameter mapping as well as dynamic pulmonary imaging applications for a number of reasons. Most of these methods make assumptions that are not realistic. For example, some methods assume the data to lie on a low dimensional space which might not true in the event of large interframe motion. Some methods rely on pre-determined information which poorly mimic the actual scenario.

The goal of this thesis is to recover the multi-dimensional MRI data from fewer samples by using a novel scheme called the blind compressed sensing (BCS) scheme. This scheme represents the underlying signal at every pixel as a linear combination of few atoms of the dictionary. The dictionary here is learned from the undersampled data and hence is subject specific. This thesis presents a fast implementation technique to improve the computation speed of the algorithm. The BCS scheme with its fast implementation has enabled several fold acceleration in acquisition without affecting the image quality. It has the ability to improve some state of the art algorithms used for accelerating multi-dimensional MRI applications.

TABLE OF CONTENTS

LIST OF TABLES

Table

LIST OF FIGURES

Figure

CHAPTER 1
INTRODUCTION

Magnetic Resonance Imaging (MRI) is a non-invasive imaging modality based on the principles of nuclear magnetic resonance (NMR). The use of MRI as imaging modality has been growing rapidly since its first commercial usage in 1981. Unlike other imaging modalities like positron emission tomography (PET) and computed tomography (CT) which use radiation, MRI uses radio-waves and strong magnetic fields to acquire images and hence does not require exposure to ionizing radiation. While X-rays provide detailed information about high density structures like bones, MRI provides good quality images of soft tissues and anatomical structures with high contrast. Like MRI, Ultrasound is also a non-ionizing imaging technique. It uses sound waves to acquire images. Though both imaging techniques provide high resolution images and are radiation free, Ultrasound can be sub-optimal in regions with interfaces between bone and air.

Another advantage of MRI as opposed to other imaging modalities is its ability to provide images with multiple tissue contrasts. These images are obtained by varying different parameters of the imaging sequence like echo time, repetition time, etc. For example, T1 weighted images differentiate between gray matter and white matter in the brain that helps in assessment of myelination, where as the T2 weighted images enhance contrast for myocardial edema. Diffusion MRI helps in detection of neuronal fibre tracts. Fig. 1.1 shows different contrast images in brain MRI.

The ability of MRI to safely provide information about anatomical structure

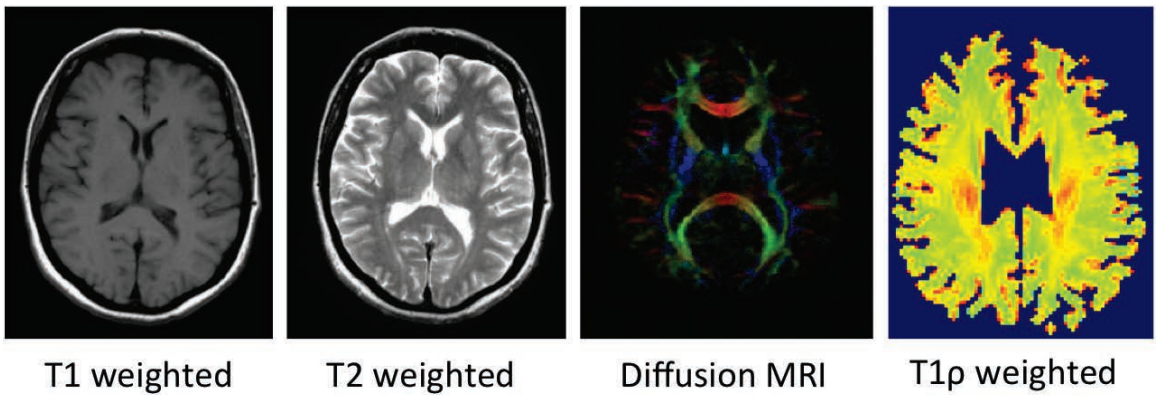

Figure 1.1: Brain images with different contrasts in MRI Brain images with different contrasts in MRI: Images with different contrast like T1 weighted, T2 weighted, Diffusion weighted and T1ρ are shown here

as well as physiological behavior makes it a promising diagnostic tool in several multi-dimensional applications like MR relaxometry, MR spectroscopy, CEST imaging, and dynamic imaging of the heart, lungs, liver, abdomen etc. (See Fig. 1.2). In this thesis we will discuss about dynamic lung imaging and multi-parameter mapping of the brain.

1.1 Motivation

One of the main challenges with MRI is its slow acquisition speed. The MRI images are acquired in Fourier space (k space) using Fourier domain encoding. This encoding is a slow process as it is limited by gradient amplitudes and gradient switching rates that could risk in peripheral nerve stimulation. [1, 2]. This makes it less applicable in the clinical setting especially in case of multi-dimensional MRI applications such as dynamic imaging of moving organs, dynamic imaging of contrast uptake

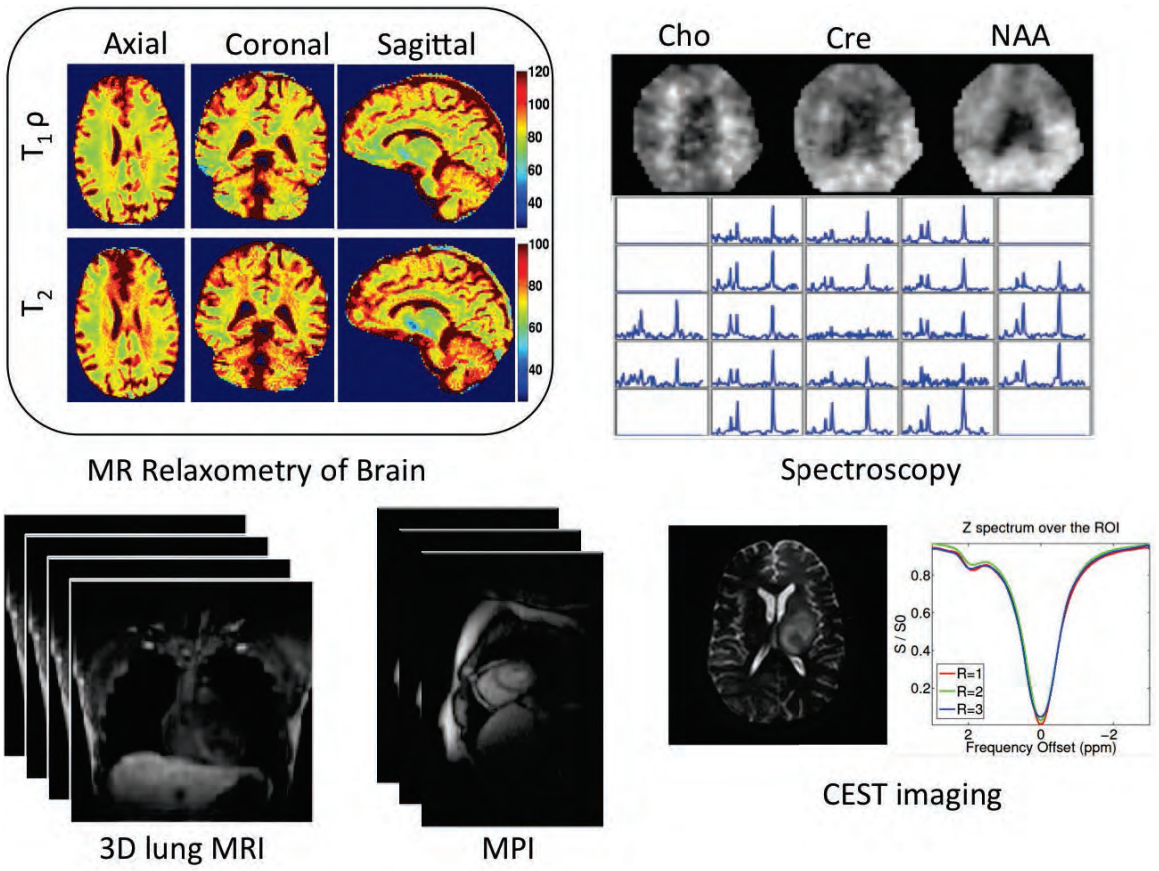

Figure 1.2: Multi-dimensional MRI applications Multi-dimensional MRI applications

through organs and characterization of tissue time relaxation parameters.

In multi-dimensional applications, multiple images are obtained as a function of time or parameters. For these applications, images need to be acquired with high spatio-temporal resolution and volume coverage in limited scan time while maintaining good image quality. For example, for multi-parameter mapping of the brain, the desirable acquisition parameters are whole brain coverage (≈128 slices), high spatial resolution ($< 2mm^3$) and multiple images at different parameters to accurately and precisely estimate the relaxation parameters. In case of dynamic pulmonary applica-

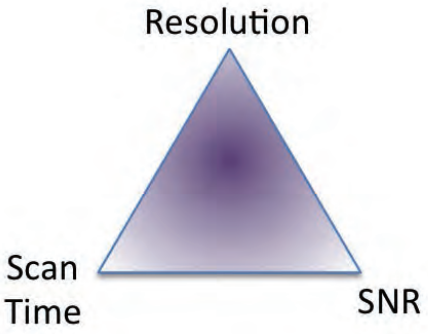

Figure 1.3: Tradeoffs in MRI Tradeoffs in MRI: MRI acquisitions are often limited by scan time, resolution and SNR.

tion, the desirable parameters are high temporal resolution ($\approx$ 500 ms), good spatial resolution to accurately delineate the diaphragm borders and whole lung coverage.

In order to acquire all the required data in clinical feasible scan times, clinicians are forced to compromise between spatial resolution, temporal resolution, volume coverage and signal to noise ratio. This results in sub-optimal diagnostic performance. The figure Fig. 1.3 shows the tradeoff between scan time, SNR and resolution. The SNR can be increased in two ways. The first one, by increasing the number of averages, however this directly affects the scan time. The other way, by increasing the thickness of the voxel, however this leads to reduction in the resolution. Since the images are acquired in k space, there exists an inverse relationship between image domain parameters and k space parameters. The Nyquist sampling theorem states that the resolution in image domain is determined by extent of k space region while

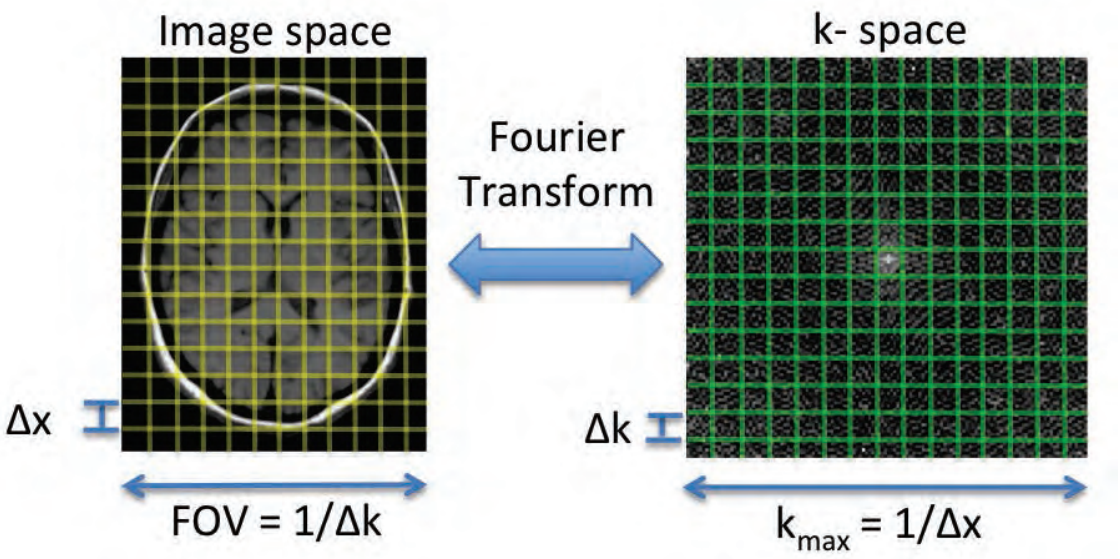

Figure 1.4: Relation between image space and k space Relation between image space and k space: The image domain and k space domain are related to each other by Fourier transform. The sampling parameters in both these domains are inversely proportional to each other. The maximum coverage of k space determines the spatial resolution and the field of view (FOV) limits the sampling density in k space.

the density of samples in the k space determines the field of view (FOV) in image domain as shown in Fig. 1.4.

Hence increasing the resolution also increases scan time. One way to reduce the scan time is to acquire fewer number of samples. However, sub-Nyquist sampling results in aliasing artifacts. Several researchers have proposed a number of techniques to reduce the aliasing artifacts using advance reconstruction methods. The image recovery from undersampled measurements is posed as an inverse problem. These problems are formulated as a linear combination of data consistency and regularization penalty. The regularization penalty makes use of the prior information like sparsity and low rank of the data. The advanced acceleration schemes have been

discussed in more detail in the following chapter.

1.2 Main focus

The main goal of this thesis is to develop an efficient reconstruction algorithm for accelerating multi-dimensional applications like multi-parameter mapping and dynamic lung imaging. We introduce novel adaptive dictionary learning scheme with fast implementations to accelerate whole brain multi-parameter mapping and 3D dynamic free breathing lung MRI.

The main contributions of the thesis is :

1. Multi-coil Blind compressed sensing algorithm and a variable splitting based fast implementation: We have introduce a novel algorithm which is a extended version of the blind compressed sensing (BCS) scheme. This algorithm incorporates coil sensitivity encoding for parallel imaging and is generalized to account for non - convex penalties. We developed an efficient algorithm which uses the augmented Lagrangian approach to solve for the dictionary and a majorize minimize approach to solve for the coefficients. The algorithm also employs efficient continuation strategies to minimize the local minima effects. We also developed a faster implementation of the algorithm to further reduced the computation time using the variable splitting approach. We adopt a double splitting in the data consistency term which separates the Fourier encoding, coil sensitivity encoding and the underlying signal to get an analytical solution for each of the subproblems. With the fast implementation of the multi-coil BCS algorithm, we

have achieved a speed up factor of up to ≈ 15 times. We have demonstrated that the image quality is comparable to the image quality obtained using the original conjugate gradient implementation. Related publications include Refs. [3, 4]

2. Application of the multi-coil BCS algorithm to accelerate whole brain multi-parameter mapping: We demonstrate the utility of BCS scheme to enable whole brain multi-parameter mapping. In this work, we looked at jointly reconstructing $T_1\rho$ and T_2 weighted acquisitions. We rely on Cartesian sampling schemes. A novel sampling strategy was introduced which is a combination of uniform pattern suitable for parallel imaging and variable density incohorent pattern suitable for compressed sensing. We also showed the advantages of multi-parameter mapping over single parameter mapping. Multi-parameter mapping can not only enable higher acceleration thus reduction in scan time but also improve the specificity of $T_1\rho$ which could be very useful in diagnosis (for eg. early detection of disease, categorizing disease progression). We observed superior image quality, improved parameter map accuracy and robustness to motion with BCS scheme as compared to other schemes at different acceleration factors. With the multi-coil BCS scheme and an acceleration factor of 8, we could enable whole brain 3D multi-parameter mapping with 1.7mm^3 isotropic resolution in clinically feasible scan time of 20min. Related publications include Refs. [5, 6]

3. Application of the multi-coil BCS algorithm to study the clinical evaluation of respiratory mechanics from 3D dynamic free breathing lung MRI: We demon-

strate the utility of the multi-coil BCS scheme to increase the spatial and temporal resolution of dynamic 3D MR imaging of diaphragm motion and lung volumes with whole lung coverage. We compare the reconstructions from BCS scheme with other schemes qualitatively and quantitatively on 8 healthy volunteers. Two expert cardio-thoracic radiologists qualitatively evaluate the reconstructed 3D datasets using a five-point scale on the basis of spatial resolution, temporal resolution and presence of aliasing artifacts. We also demonstrate the feasibility of the BCS scheme in calculating lung volume changes which could be useful to perform correlations with spirometry measurements. A temporal resolution of ≈500ms, spatial resolution of 2.7 x 2.7 x 10mm^3 with whole lung coverage (16 slices) was achieved using the BCS scheme. Related Refs. [7–9]

1.3 Outline of the thesis

The structure of the thesis is as follows:

- **Chapter 2: Background**: This chapter presents a brief overview of the different compressed sensing and dictionary learning based schemes used for accelerating multi-dimensional MRI applications

- **Chapter 3: A variable splitting based algorithm for fast multi-coil blind compressed sensing MRI reconstruction**: This chapter presents extensions of the Blind compressed sensing scheme to include parallel imaging and non-convex penalties along with a novel implementation. Using a variable splitting technique, this chapter presents an faster implementation which

reduces the computation time of the multi-coil BCS scheme by up to 15 fold.

- **Chapter 4: Accelerated whole brain multi-parameter mapping using blind compressed scheme**: In this chapter, we demonstrate the utility of multi-coil BCS scheme to enable whole brain $T_1\rho$ and T_2 parameter mapping. The chapter discusses considerations on sampling schemes and advantages of multi-parameter mapping as compared to single parameter mapping. Excessive comparisons against existing acceleration methods are presented.

- **Chapter 5: Blind compressed sensing enables 3D dynamic free breathing MR imaging of lung volumes and diaphragm motion**: In this chapter, we demonstrate the utility of multi-coil BCS scheme to enable 3D dynamic free breathing lung imaging. Clinical evaluations comparing the BCS scheme and other existing methods on a cohort of 8 healthy individuals are presented. Analysis of lung volume changes from the reconstructed datasets using image segmentation is presented in this chapter

- **Chapter 6: Summary and future work**: This chapter provides summary of the thesis and discusses further directions about the research.

CHAPTER 2
BACKGROUND

In this chapter, we will study few existing schemes to accelerate multi- dimensional applications. We mainly look at recent advances in signal representation which exploit the redundancy in the data. Several researchers have introduced different acquisition schemes which exploit the redundancy in the data as well as the advances in parallel imaging. The chapter is organized as follows: We will start by introducing the global signal model, followed by linear models and compressed sensing schemes. The later section describes the blind linear models and the blind compressed sensing scheme.

2.1 Global signal model

2.1.1 Recovery from undersampled measurements

As mentioned in the previous chapter, accelerated acquisitions for multi- dimensional MRI applications can help improve the tradeoffs between resolution and coverage. We represent the multi-dimensional signal as $\gamma(\mathbf{r}, d)$ where $\mathbf{r} = (x, y, z)$ are the spatial coordinates and d denotes the time or the parametric dimension depending upon the MRI application. The undersampled measurement in the $k - d$ space is expressed as:

$$b(k_{\mathbf{r}}, d_i) = \int_{\mathbf{r}} c_l(\mathbf{r}, d_i)\gamma(\mathbf{r}, d_i)exp(-jk_{\mathbf{r}}^T\mathbf{r})d\mathbf{r} + n(k_{\mathbf{r}}, d_i) \tag{2.1}$$

where $c_l(\mathbf{r}, d_i)$ denotes the space and time dependent coil sensitivity profiles, $k_\mathbf{r}, d_i$ denotes the i^{th} location in the $k_\mathbf{r}, d$ space and n denotes the additive noise. The expression in Eq. (2.1) can be compactly written as:

$$b = \mathcal{A}(\gamma) + n \tag{2.2}$$

where the operator $\mathcal{A}$ models the Fourier encoding on a specified sampling trajectory. It can also model the coil sensitivity information for parallel imaging. The goal is to recover the multi-dimensional data from these undersampled measurements b.

2.1.2 Partial separable (PS) model

Several models used for recovering undersampled signal utilize a single global signal model to represent the voxel profiles $\gamma(\mathbf{r}, d)$ and can be interpreted by the partial separability (PS) model. This partial separability model proposed by Liang et al. [10] represents the signal as shown below:

$$\gamma(\mathbf{r}, d) = \sum_{i=1}^{R} \gamma_i(\mathbf{r}, d) = \sum_{i=1}^{R} u_i(r) v_i(d) \tag{2.3}$$

where R denotes the total number of basis functions in the dictionary denoted by v_i. u_i denote the coefficients also referred to as spatial weights. The number of basis functions can be interpreted as the model order of the data.

Table 2.1: Overview of different acceleration schemes which use the partial separable model Overview of different acceleration schemes which use the partial separable model

	Type of basis functions	Number of basis functions	Sparsity on coefficients?
Linear models eg. DIME, k-t BLAST	Exponential	Few	No
Blind linear models eg.PSF, k-t PCA, k-t SLR	Learnt	Few	No
Compressed sensing eg. k-t SPARSE, k-t FOCUSS	Pre-determined	Many	Yes
Blind compressed sensing	Learnt	Many	Yes

2.2 PS model based schemes for accelerating multi-dimensional imaging

Based on the choices for number and type of basis functions, constraints on the model coefficients, several acceleration schemes have evolved over recent years as shown in Table 5.1.

2.2.1 Linear models

The linear models like DIME [11], UNFOLD [12, 13] and k-t BLAST [14] represent the signal as a linear combination of few exponential temporal basis functions. These models are suited for MRI applications which are periodic in nature. For example, in cardiac CINE imaging, the time domain signal is pseudo-periodic in nature and hence $x - f$ space has very few non-zero components as shown in Fig. 2.1

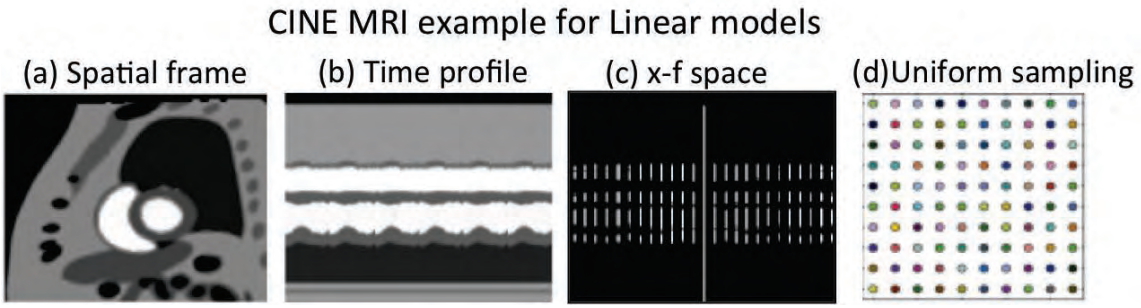

Figure 2.1: CINE data representation in temporal Fourier transform domain (x-f) CINE data representation in temporal Fourier transform domain (x-f): The figure shows a numerical cardiac CINE phantom. A spatial image, its time profile, the representation in $x - f$ space and sampling pattern is shown in (a-d). Note: The $x - f$ space has few a non-zeros entries.

The signal representation for linear models is:

$$\gamma(\mathbf{r}, t) = \sum_{i=1}^{R} u_i(\mathbf{r}) e^{j2\pi f_i t}; R < N \tag{2.4}$$

The recovery of signals under this model is a two step process. In the first step, the frequencies f_i are determined from training data (also called as navigator signals). Once the frequencies are known, the model coefficients u_i's can be estimated by fitting the data with the model in Eq.(2.4) in the least square sense. These methods which rely on coherent sampling patterns result in aliasing artifacts in form of signal overlaps. Since these models assume the signal to be periodic, such methods are not suited for applications with non-periodic signals (eg. Free breathing cardiac perfusion imaging). The inaccuracy in training data can result in mismatch between the data and the model.

2.2.2 Compressed sensing (CS)

In compressed sensing (CS) based techniques, the multi-dimensional signal is represented as a sparse linear combination of atoms from a pre-determined dictionary. The CS representation of a signal is as follows:

$$\gamma(\mathbf{r},d)=\sum_{i=1}^{R}\underbrace{u_i(\mathbf{r})}_{sparse}\underbrace{v_i(d)}_{pre-determined} \quad ;R\geqslant N \tag{2.5}$$

The basis functions $v_i(t)$ are pre-determined and they belong to an over-complete and not necessarily orthogonal dictionary. Unlike linear models, the dictionary is not limited to Fourier dictionary. Depending on the application, the dictionary can be formed from Fourier signals as in case of cardiac CINE imaging or from Bloch equations as in case of parameter mapping [15]. Unlike, linear models the sampling patterns in this model are incoherent. The CS scheme assumes the model coefficients $u_i(\mathbf{r})$ to be sparse. The analysis formulation for CS scheme is as follows:

$$\gamma(\mathbf{r},d)=\arg\min_{\gamma}\|\mathcal{A}(\gamma)-b\|_F^2+\lambda\|\psi(\gamma)\|_{\ell_1} \tag{2.6}$$

Here ψ is a sparsity inducing operator. For example, it can be chosen as a wavelet transform [16,17], finite difference [18,19], or Fourier transform operator [20,21]. This sparsity is enforced using an ℓ_1 norm. For example, as seen in Fig. 2.1(c), the $x-f$ sparsity in CINE imaging dataset is exploited by the CS scheme. CS scheme eliminates the need for training data, however, the performance is heavily dependent on the sparsifying operator and the pre-determined dictionary. For example, in param-

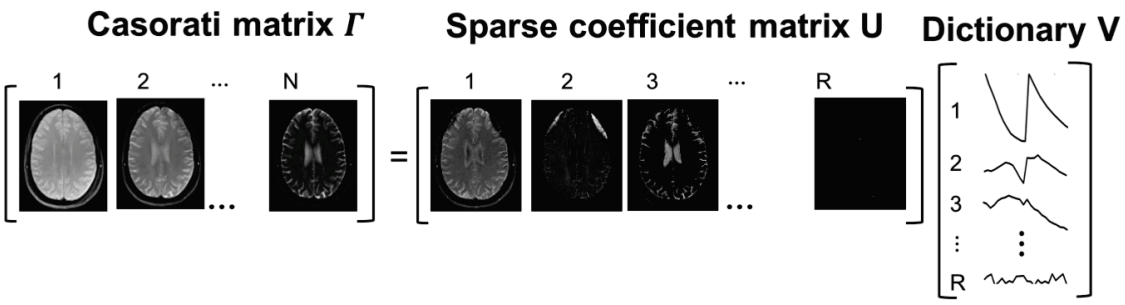

Figure 2.2: Casorati matrix representation of multi-parameter mapping dataset Casorati matrix representation of multi-parameter mapping dataset: The figure shows the Casorati matrix Γ where each of the contrast weighted images are stacked as column vectors.

eter mapping applications, the dictionary is formed from Bloch equations. However, in presence of motion during acquisition this dictionary is sub-optimal as it does not account for motion. This lead to further investigation of data adaptive representation which are discussed in the next sections.

2.2.3 Blind linear models

Blind linear models (BLM) are the adaptation of linear models to non-periodic multi-dimensional datasets (For example. Cardiac perfusion imaging, See Fig. 2.3(b)). BLM models assume the basis functions to be arbitrary instead of Fourier exponentials as in case of linear models. The basis functions are learnt from the data itself and hence is termed as blind linear models. The signal is represented as a linear combination of few arbitrary basis functions. In order to exploit the correlations within the data, the data is rearranged as a Casorati matrix [10] as shown below (See Fig. 2.2:

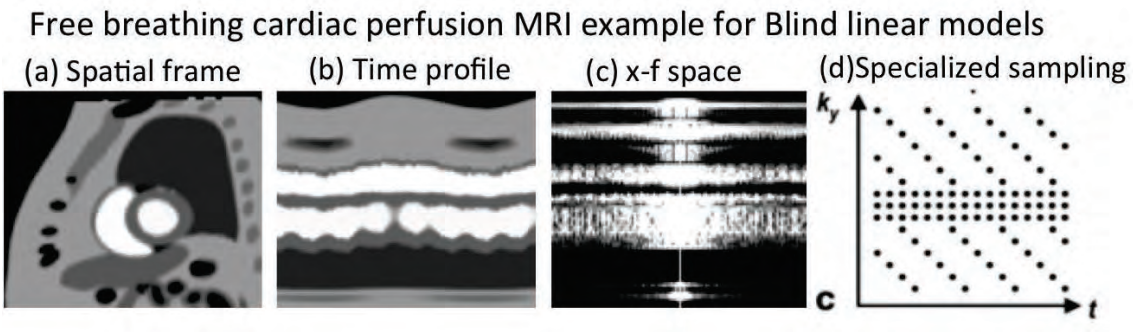

Figure 2.3: Representation of non-periodic signal in $x-f$ domain Representation of non-periodic signal in $x-f$ domain: A spatial frame, time profile, $x-f$ domain representation and the sampling pattern is shown for a numerical phantom that mimics a Cardiac perfusion MRI data (a-d). Since the cardiac perfusion data is non-periodic in nature, the $x-f$ space is no longer sparse. Note: The specialized sampling pattern in (d) are required in the two step approaches used in BLM/ low rank models.

$$\mathbf{\Gamma}_{M\times N} = \begin{pmatrix} \gamma(\mathbf{r}_1, d_1) & . & \gamma(\mathbf{r}_1, d_N) \\ . & . & . \\ . & . & . \\ \gamma(\mathbf{r}_M, d_1) & . & \gamma(\mathbf{r}_M, d_N) \end{pmatrix} \tag{2.7}$$

where M is the number of voxels in the image and N is the number of encoding parameters. This matrix Γ can be decomposed as $U_{M\times R}\Sigma_{R\times R}V^H_{R\times N}$. The signal representation with respect to PS model is as follows:

$$\gamma(\mathbf{r}, d) = \sum_{i=1}^{R} u_i(\mathbf{r})\, \underbrace{v_i(d)}_{learnt}; R << N \tag{2.8}$$

The basis functions $v_i(d)$ are the columns of the matrix V and the coefficients $u_i(\mathbf{r})$ are the row vectors of $U\Sigma$. These basis functions estimated by performing principal

component analysis (PCA), singular value decomposition (SVD) or Karhunen - Loeve transform (KLT) on the data itself to provide richer representations as compared to linear models. The signal recovery is a two step approach [10, 20, 22, 23] .

1. The first step is to estimate the basis functions $v_i(d)$ from training data using PCA/SVD/KLT. Low resolution spatial data is often used as training data. This data is obtained by taking the inverse fast Fourier transform (IFFT) of the center k-space and hence requires the center k-space to be sampled at Nyquist sampling rate.

2. Once the basis functions are estimated, the model coefficients $u_i\mathbf{r}$ are determined using least square fitting method from the undersampled data.

Even though, the BLM models provide a richer representation than linear models or CS based models, there have a few drawbacks. The BLM models assume that basis functions estimated from the low resolution data approximate the actual basis functions of the fully sampled data. Also, it requires specialized sampling patterns as show in Fig. 2.3(d) which sample the center k-space at Nyquist sampling rate and the outer k-space at sub-Nyquist sampling.

2.2.4 Low rank and sparse recovery

The low rank methods [24, 25] assume the data to lie on a low dimensional subspace and hence the Casorati matrix Γ in Eq. (2.7) can also be considered to have

a low rank. The low rank matrix recovery problem is formulated as follows:

$$\Gamma = \arg\min_{\Gamma} \|\mathcal{A}(\Gamma) - b\|_F^2 + \lambda\|\Gamma\|_* \tag{2.9}$$

Here the first term is the data consistency term. The nuclear norm penalty denoted by $\|\Gamma\|_*$ which is the sum of the singular values of Γ, is a convex relaxation for the rank constraint. This formulation jointly estimates the basis functions and the model coefficients and hence eliminates the need for training data. Some approaches also employ non-convex penalties like Schatten- p norm (p <1) to enforce low rank constraint [26].

The performance of low rank methods can be further improved by adding sparsity constraints. Some methods decompose the data as low rank plus sparse [27] while other methods employ joint low rank and sparsity constraints [26]. The k-t SLR scheme enforces the low rank penalty using the Schatten p-norm in addition to the spatio-temporal sparsity. The image recovery in k-t SLR scheme is formulated as:

$$\begin{aligned}\mathbf{\Gamma}^* = \arg\min_{\mathbf{\Gamma}} \|\mathcal{A}(\mathbf{\Gamma}) - b\|_2^2 + \lambda_1 \left(\sum_{i=1}^{\min(M,N)} (\Sigma_{i,i})^p \right) \\ +\lambda_2 \| \sqrt{|\bigtriangledown_x(\mathbf{\Gamma})|^2 + |\bigtriangledown_y(\mathbf{\Gamma})|^2 + \alpha|\bigtriangledown_t(\mathbf{\Gamma})|^2} \|_{\ell_1}\end{aligned} \tag{2.10}$$

where $\lambda_1, \lambda_2, \alpha$ are the regularization parameters. The second term enforces the low rank constraint where as the third term enforces sparsity through spatio-temporal total variation penalty.

The low rank and two step BLM methods assume the data to be globally low

rank. However since the voxel profiles are different at different anatomical regions the rank of the model would be different across these regions. Specifically, the rank of the dataset in regions with more motion (near the heart in case of cardiac imaging or near the chest wall or diaphragm in lung imaging) is higher than the rank of the dataset in static regions. Hence locally low rank models would provide a richer representation as compared to these low rank models or low rank and sparse models.

2.2.5 Blind compressed sensing

Like CS scheme, the voxel intensity profiles are modeled as a sparse linear combination of basis functions from a dictionary. However, the dictionary is learnt from the undersampled measurements unlike CS which uses pre-determined dictionary. Specifically, the Casorati matrix of the data $\mathbf{\Gamma}$ is modeled as $\mathbf{\Gamma} = \mathbf{UV}$. The proposed algorithm learns the dictionary basis functions $\mathbf{V}$, as well as their sparse coefficients $\mathbf{U}$, from the undersampled data by solving a constrained optimization problem. The recovery from the undersampled measurements is formulated as shown below:

$$\{\mathbf{U}^*, \mathbf{V}^*\} = \arg\min_{\mathbf{U},\mathbf{V}} \underbrace{\|\mathcal{A}(\mathbf{UV}) - \mathbf{b}\|_F^2 + \lambda \|\mathbf{U}\|_{l_1}}_{\mathcal{C}(\mathbf{U},\mathbf{V})} \text{ such that } \|\mathbf{V}\|_F^2 < 1. \tag{2.11}$$

The first term in Eq. [3.3] ensures data consistency. The $\mathcal{A}$ operator encodes the Fourier transform operator on a specified sampling trajectory. The second term promotes sparsity on the spatial coefficients $u_i(\mathbf{x})$ by utilizing a convex ℓ_1 norm prior on $\mathbf{U}$, which is given by $\|\mathbf{U}\|_{l_1} = \left(\sum_{i=1}^{M} \sum_{j=1}^{r} |u(i,j)|\right)$, and λ is the regularization

parameter. The optimization problem is constrained by imposing unit Frobenius norm on the over-complete dictionary $\mathbf{V}$, making the recovery problem well posed. Since the dictionary is subject-specific, this approach ensures that any deviations from the true parametric encoding, such as subject motion, field inhomogeneity and chemical shift artifacts, are learned by the basis functions. The BCS scheme uses a considerably larger dictionary of non-orthogonal basis functions, which provides a richer representation of the data compared to the smaller dictionary of orthogonal basis functions used in the k-t PCA and PSF schemes. The sparsity of the coefficients ensures that the number of active basis functions at each voxel are considerably lower than the rank of the dataset. Since the basis functions used at different spatial locations are different, the BCS scheme can be viewed as a locally low-rank scheme; the appropriate basis functions (subspace) at each voxel are selected independently. Since the number of basis functions required at each voxel is considerably lower than the global rank, the BCS scheme can provide a richer representation with lower degrees of freedom; this translates to better trade-offs between accuracy and achievable acceleration, especially in multi-dimensional MRI applications with inter-frame motion.

CHAPTER 3
A VARIABLE SPLITTING BASED ALGORITHM FOR FAST MULTI-COIL BLIND COMPRESSED SENSING MRI RECONSTRUCTION

3.1 Introduction

Recently, several researchers have proposed to jointly estimate the sparse representations and the dictionaries from the under sampled data at hand. Dictionaries containing atoms of one-dimensional non-orthogonal temporal bases [28] or two-dimensional spatial patches [29] have been proposed for dynamic and static applications. These schemes termed as blind compressed sensing (BCS) have shown considerable promise over conventional CS schemes in several MRI applications such as dynamic contrast enhanced MRI [28], functional lung [30], parametric, and high resolution static MRI [29].

The BCS scheme is formulated as a constrained optimization problem consisting of linear combination of data fidelity l_2 norm, and a sparsity promoting norm on the coefficients subject to a Frobenius norm constraint on the dictionary. The single coil BCS algorithmic implementation in [28] relies on iterations between quadratic update steps of the coefficient and dictionary update steps. These steps were solved using slow iterative conjugate gradient algorithms due to the complexity in constructing the inverses of the matrices resulting from the data fidelity. The large computational complexity encountered during the optimization pose a challenge in dealing with large practical datasets such as multi-coil and three-dimensional applications.

In this chapter, we propose to employ variable splitting strategies [31] to efficiently decouple the coefficient update and dictionary update steps from the data fidelity term. Through the decoupling, we develop a computational efficient algorithm that efficiently cycles between different steps that have analytical closed form solutions. We demonstrate through experiments on multi coil parametric MRI data, the proposed algorithm obtains a significant speed up factor of ten fold over the previous implementation.

3.2 Multi-coil BCS scheme

In multi-dimensional imaging, the k-space corresponds to several images acquired at different values of encoding parameters denoted by d. For example for multi-parameter mapping applications, multiple contrast weighted images are acquired by varying echo time, spin lock time, flip angle, repetition time depending on the underlying problem. In case of dynamic imaging applications, multiple images are acquired as a function of time to image moving organs.

We model the multi-coil undersampled measurement as:

$$\mathbf{b}(\mathbf{k},d) = \underbrace{\mathbf{SFC}}_{\mathcal{A}}[\gamma(\mathbf{x},d)] + \mathbf{n}(\mathbf{k},d), \tag{3.1}$$

where $\mathbf{b}(\mathbf{k},d)$ represents the concatenated vector of the $\mathbf{k}-d$ measurements from all the coils. $\gamma(\mathbf{x},d);(\mathbf{x}=(x_1,y_1))$ denote the underlying images pertaining to different contrasts; $\mathbf{n}$ is additive noise. $\mathcal{A}$ is the operator that models coil sensitivity $\mathbf{C}$ and Fourier encoding $\mathbf{F}$ on a specified $\mathbf{k}-d$ sampling trajectory $\mathbf{S}$. The dataset is represented as $M \times N$ Casoriti matrix [10] $\mathbf{\Gamma}_{M\times N}$

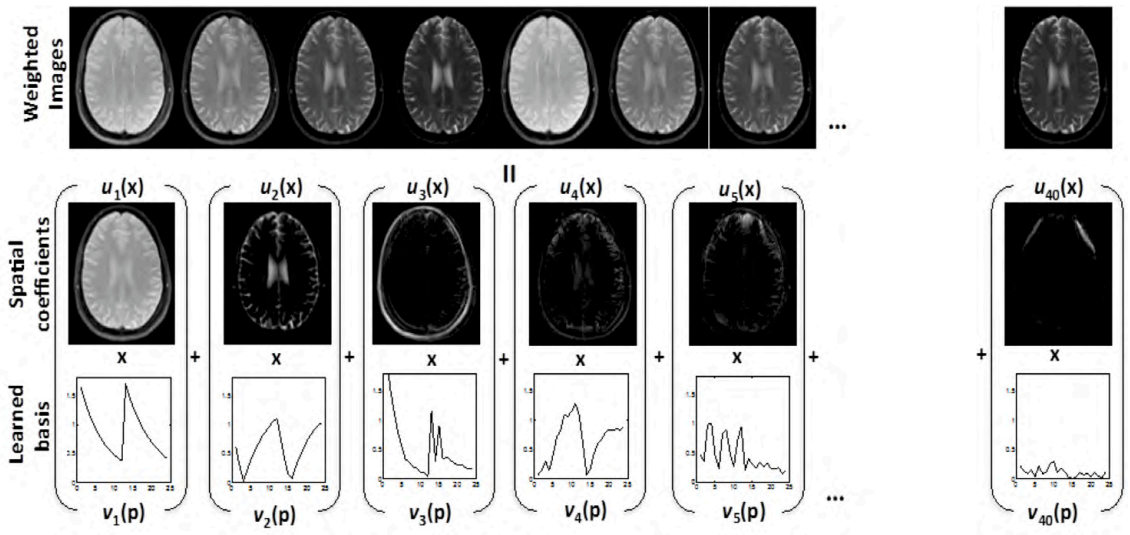

Figure 3.1: BCS model representation BCS model representation: The model representation of the multi-parameter signal of a single brain slice with 24 parametric measurements (12 TEs and 12 TSLs) is shown above. The signal $\mathbf{\Gamma}$ is decomposed as a linear combination of Spatial weights $\mathbf{u}_i(x)$ ($\mathbf{x}$ are the spatial locations (pixels)) and temporal basis functions in $\mathbf{v}_i(d)$ (d are the parametric measurements). We observe that only 3-4 coefficients per pixel are sufficient to represent the data. The Frobenius norm attenuates the insignificant basis functions.

$$\mathbf{\Gamma}_{M\times N} = \begin{pmatrix} \gamma(\mathbf{r}_1, d_1) & . & \gamma(\mathbf{r}_1, d_N) \\ . & . & . \\ . & . & . \\ \gamma(\mathbf{r}_M, d_1) & . & \gamma(\mathbf{r}_M, d_N) \end{pmatrix} \tag{3.2}$$

where M is the number of voxels in the image and N is the number of encoding parameters.

3.2.1 Image reconstruction

We model $\mathbf{\Gamma}$ as a product of spatial coefficients $\mathbf{U}_{M\times R}$ and dictionary $\mathbf{V}_{R\times N}$ as shown in Fig. 3.1. The joint recovery of $\mathbf{U}$, $\mathbf{V}$ is formulated as a constrained

optimization problem:

$$\arg\min_{\mathbf{U},\mathbf{V}} \underbrace{\|\mathcal{A}(\mathbf{UV}) - \mathbf{b}\|_F^2 + \lambda\|\mathbf{U}\|_{\ell_p}}_{\mathcal{C}(\mathbf{U},\mathbf{V})} \text{ s. t. } \|\mathbf{V}\|_F^2 < 1. \tag{3.3}$$

The first term in Eq. [3.3] ensures data consistency. The second term promotes sparsity on the spatial coefficients $u_i(\mathbf{x})$ by utilizing a convex ℓ_p norm prior on $\mathbf{U}$, which is given by $\|\mathbf{U}\|_{l_p} = \left(\sum_{i=p}^{M}\sum_{j=1}^{r}|u(i,j)|^p\right)^{1/p}$, $0 < p < 1$; and λ is the regularization parameter. The optimization problem is constrained by imposing unit Frobenius norm on the over-complete dictionary $\mathbf{V}$, making the recovery problem well posed. Note that we are jointly estimating the sparse coefficients $\mathbf{U}$ and the subject-specific dictionary $\mathbf{V}$ directly from the under-sampled $k-d$ data. Since the dictionary is subject-specific, this approach ensures that any deviations from the true parametric encoding, such as subject motion, field inhomogeneity and chemical shift artifacts, are learned by the basis functions. The number of active bases at a specified voxel depends on several factors that include partial volume effects, motion, and magnetization disturbances due to inhomogeneity artifacts. The spatial weights $u_i(\mathbf{x})$ are encouraged to be sparse since we expect only a few tissue types to be active at any specified voxel. The main difference of the proposed scheme from [28] is the use of an efficient algorithm and the extension to multi-coil formulation with incorporation of non-convex penalties which enables better recovery at high acceleration rates.

3.2.2 Algorithm 1: Without using variable splitting

We majorize an approximation of the ℓ_p penalty on $\mathbf{U}$ in Eq. (3.3) as $\|\mathbf{U}\|_{\ell_p} \approx \min_{\mathbf{L}} \frac{\beta}{2}\|\mathbf{U}-\mathbf{L}\|^2 + \|\mathbf{L}\|_{\ell_p}$, where $\mathbf{L}$ is an auxiliary variable. This approximation

becomes exact as $\beta \to \infty$. We use augmented Lagrangian optimization scheme to enforce the constraint $\mathbf{V} = \mathbf{Q}$, where $\mathbf{Q}$ is the auxiliary variable for $\mathbf{V}$. Thus, the optimization problem is given by

$$\begin{aligned}\{\mathbf{U}^*, \mathbf{V}^*\} = \arg\min_{\mathbf{U},\mathbf{V}} \min_{\mathbf{Q},\mathbf{L}} \|\mathcal{A}(\mathbf{UV}) - \mathbf{b}\|_F^2 + \frac{\beta\lambda}{2}\|\mathbf{U} - \mathbf{L}\|_F^2 \\ +\lambda\|\mathbf{L}\|_{\ell_p} \text{ s. t. } \|\mathbf{Q}\|_F^2 < 1, \mathbf{V} = \mathbf{Q}\end{aligned} \tag{3.4}$$

Here, $\mathbf{Q}$ is the auxiliary variable for $\mathbf{V}$. The constraint $\mathbf{V} = \mathbf{Q}$ is enforced by adding the augmented Lagrangian term $\frac{\alpha}{2}\|\mathbf{V} - \mathbf{Q}\|^2 + \langle \mathbf{\Lambda}, (\mathbf{V} - \mathbf{Q})\rangle$ to the above cost function. Here, $\mathbf{\Lambda}$ is the Lagrange multiplier term that will enforce the constraint. These simplifications enable us to decouple the optimization problem in (3.3) into different sub-problems. We use an alternating strategy to solve for the variables $\mathbf{U}, \mathbf{V}, \mathbf{Q}$ and $\mathbf{L}$ (See Fig. 3.2(a)). All of these sub-problems are solved independently in an efficient fashion as described below, assuming the other variables to be fixed. The sub-problems in $\mathbf{U}$ and $\mathbf{V}$ have the following update steps:

Update on $\mathbf{U}$: The sub-problem on $\mathbf{U}$, assuming the other variables to be fixed, can be written as

$$\mathbf{U}_{n+1} = \arg\min_{\mathbf{U}} \|\mathcal{A}(\mathbf{U}_n\mathbf{V}_n) - \mathbf{b}\|_2^2 + \frac{\lambda\beta}{2}\|\mathbf{U} - \mathbf{L}_{n+1}\|_2^2 \tag{3.5}$$

Since it is a quadratic problem, we solve it using a conjugate gradient (CG) algorithm. Here, $\mathbf{U}_n$, $\mathbf{V}_n$ and $\mathbf{L}_n$ are the variables at the n^{th} iteration.

Update on $\mathbf{V}$: Minimizing the cost function with respect to $\mathbf{V}$, assuming other vari-

ables to be constant yields

$$\mathbf{V}_{n+1} = \|\mathcal{A}(\mathbf{U}_{n+1}\mathbf{V}_n) - \mathbf{b}\|_F^2 + < \mathbf{\Lambda}_n, \mathbf{V}_n - \mathbf{Q}_{n+1} > + \frac{\alpha}{2} \|\mathbf{V}n - \mathbf{Q}_{n+1}\|_F^2 . \quad (3.6)$$

Iterative methods like conjugate gradient are required to solve these subproblems due to the enormous size of A. In addition, for the majorization to well approximate the ℓ_p penalty, β needs to be a high value. At higher values of β, the condition number of these subproblems is significantly high resulting in slow convergence as many iterations of CG are required.

3.3 Algorithm 2 : FastBCS using variable splitting

To improve convergence speed, Ramani and Fessler proposed the use of the technique of variable splitting to decouple the effect of coil sensitivities **C** and the regularization [31]. We introduce a novel optimization algortihm using variable splitting technique to accelerate the convergence of Eq. 3.4. First, we decouple the data fidelity term from sparse coefficients **U** and dictionary **V** by introducing a constraint $\mathbf{X} = \mathbf{UV}$ where **X** is the auxiliary variable for **UV**. The optimization problem is of the form

$$\underset{\mathbf{U},\mathbf{V},\mathbf{X}}{\arg\min} \|\mathbf{SFCX} - \mathbf{b}\|_F^2 + \lambda \|\mathbf{U}\|_{\ell_p} \text{ s. t. } \mathbf{X} = \mathbf{UV}, \|\mathbf{V}\|_F^2 < 1 \quad (3.7)$$

We further decouple the coil sensitivities from **X** by introducing another constraint **Z**=**CX** where **Z** is the auxiliary variable. The constrained optimization problem can

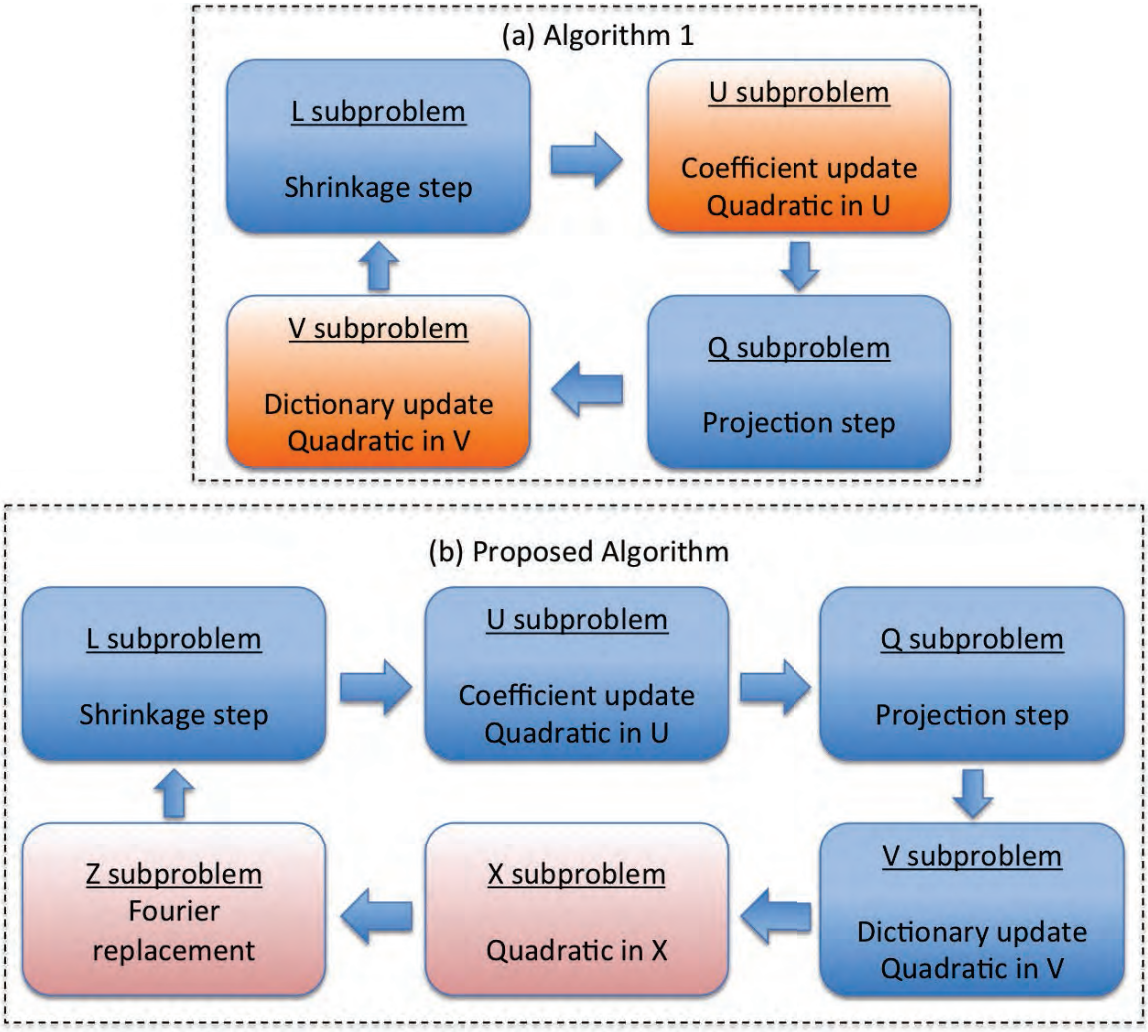

Figure 3.2: Flowchart of implementations for Algorithm 1 and proposed algorithm Flowchart of implementations for Algorithm 1 and proposed algorithm: The flowchart of the implementations for Algorithm 1 and proposed algorithm are shown in (a) and (b) respectively. The optimization problem in Algorithm 1 is solved by iterating between the 4 steps for algorithm 1 and 6 steps for proposed algorithm as shown. However the $\mathbf{U}$ and the $\mathbf{V}$ update steps use CG method making it slow where all the 6 sub-problems in proposed algorithm are solved analytically giving the speed up factor.

be written as

$$\begin{aligned} \underset{\mathbf{U},\mathbf{V},\mathbf{X},\mathbf{Z}}{\arg\min} \|SF\mathbf{Z} - \mathbf{b}\|_F^2 + \lambda \|\mathbf{U}\|_{l_p} \text{ s.t. } \mathbf{X} = \mathbf{UV}, \\ \|\mathbf{V}\|_F^2 < 1, \mathbf{Z} = \mathbf{CX} \end{aligned} \tag{3.8}$$

We majorize an approximation of the ℓ_p penalty on $\mathbf{U}$ in (3.3) as $\|\mathbf{U}\|_{\ell_p} \approx \min_{\mathbf{L}} \frac{\beta}{2}\|\mathbf{U}-\mathbf{L}\|^2 + \|\mathbf{L}\|_{\ell_p}$, where $\mathbf{L}$ is an auxiliary variable. We enforce the constraints in Eq. 3.8 by using an augmented Lagrangian (AL) framework [32]. The associated AL function is written as

$$\begin{aligned}\mathcal{L}(\mathbf{U},\mathbf{V},\mathbf{L},\mathbf{Q},\mathbf{X},\mathbf{Z}) = \|\mathbf{SFZ}-\mathbf{b}\|_F^2 + \frac{\beta_X}{2}\|\mathbf{X}-\mathbf{UV}\|_F^2 \\ +\mathbf{\Lambda}_X'(\mathbf{X}-\mathbf{UV}) + \lambda\|\mathbf{L}\|_{\ell_p} + \frac{\lambda\beta_U}{2}\|\mathbf{U}-\mathbf{L}\|_F^2 \\ +\frac{\beta_V}{2}\|\mathbf{V}-\mathbf{Q}\|_F^2 + \mathbf{\Lambda}_V'(\mathbf{V}-\mathbf{Q}) \\ +\frac{\beta_Z}{2}\|\mathbf{Z}-\mathbf{CX}\|_F^2 + \mathbf{\Lambda}_Z'(\mathbf{Z}-\mathbf{CX}) \text{ s. t. } \|\mathbf{Q}\|_F^2 < 1\end{aligned} \tag{3.9}$$

Here $\mathbf{Q}$ is the auxiliary variable for $\mathbf{V}$, $\mathbf{\Lambda}_X, \mathbf{\Lambda}_V$ and $\mathbf{\Lambda}_Z$ are the Lagrange multipliers. $\beta_X, \beta_V, \beta_U$ and β_Z are the penalty parameters. We use an alternating strategy to solve for the variables $\mathbf{U}, \mathbf{V}, \mathbf{Q}, \mathbf{L}, \mathbf{X}$ and $\mathbf{Z}$ (See Fig. 3.2(b)). All of these subproblems are solved analytically as described below, by minimizing the Eq. 3.9 with respect to these variables one at a time assuming the other variables to be fixed.

$\mathbf{L}$ subproblem: Ignoring all the terms independent of $\mathbf{L}$, Eq. 3.9 can be written as

$$\arg\min_{\mathbf{L}} \frac{\lambda\beta_U}{2}\|\mathbf{U}-\mathbf{L}\|_F^2 + \lambda\|\mathbf{L}\|_{\ell_p} \tag{3.10}$$

The $\mathbf{L}$ subproblem is solved using shrinkage rule as

$$\mathbf{L}_{n+1} = \frac{\mathbf{U}}{|\mathbf{U}_n|}\left(|\mathbf{U}_n| - \frac{1}{\beta}|\mathbf{U}_n|^{p-1}\right)_+ \tag{3.11}$$

where '+' represents the soft thresholding operator defined as $(\tau)_+ = \max\{0,\tau\}$ and β_U is the penalty parameter.

$\mathbf{U}$ subproblem: The minimization of Eq. 3.9 with respect to $\mathbf{U}$ results in a quadratic

subproblem which has an closed form solution given by

$$\arg\min_{\mathbf{U}} \frac{\beta_X}{2}\|\mathbf{X}-\mathbf{UV}\|_F^2 + \mathbf{\Lambda}_X'(\mathbf{X}-\mathbf{UV}) + \frac{\lambda\beta_U}{2}\|\mathbf{U}-\mathbf{L}\|_F^2 \tag{3.12}$$

The quadratic subproblem can be solved analytically as shown below.

$$\mathbf{U}_{n+1} = (\beta_{X_n}\mathbf{X}_n\mathbf{V}_n' + \mathbf{\Lambda}_X\mathbf{V}_n' + \lambda\beta_U\mathbf{L}_{n+1})\mathbf{H}_U^{-1} \tag{3.13}$$

$$\mathbf{H}_U = \beta_X\mathbf{V}_n\mathbf{V}_n' + \lambda\beta_U I \tag{3.14}$$

Q subproblem: The **Q** subproblem is obtained by minimizing Eq. 3.9 with respect to Q

$$\arg\min_{\mathbf{Q}} \frac{\beta_V}{2}\|\mathbf{V}-\mathbf{Q}\|_F^2 + \mathbf{\Lambda}_V'(\mathbf{V}-\mathbf{Q}) \text{ s. t. } \|\mathbf{Q}\|_F^2 < 1 \tag{3.15}$$

The above problem is solved using a projection scheme as specified in Eq. 3.16. If Frobenius norm of **Q** is less than unity, we set $\mathbf{Q} = \mathbf{V}$, else we scale **V** to have a unit Frobenius norm

$$\mathbf{Q}_{n+1} = \begin{cases} V_n & \|V_n\|_F^2 \leqslant 1 \\ \frac{1}{\|V_n\|_F}V_n & \text{else} \end{cases} \tag{3.16}$$

Note that $\mathbf{Q}_n$ is obtained by scaling $\mathbf{V}_n$ so that the Frobenius norm is unity.

V subproblem: The **V** subproblem is a quadratic subproblem as shown below.

$$\begin{aligned}\arg\min_{\mathbf{V}} \frac{\beta_X}{2}\|\mathbf{X}-\mathbf{UV}\|_F^2 + \mathbf{\Lambda}_X'(\mathbf{X}-\mathbf{UV}) \\ + \frac{\beta_V}{2}\|\mathbf{V}-\mathbf{Q}\|_F^2 + \mathbf{\Lambda}_V'(\mathbf{V}-\mathbf{Q})\end{aligned} \tag{3.17}$$

Minimization of the above equation with respect to **V** yields the following closed form solution

$$\mathbf{V}_{n+1} = \mathbf{H}_V^{-1}(\beta_X\mathbf{U}_{n+1}'\mathbf{X}_n + \mathbf{U}_{n+1}'\mathbf{\Lambda}_X + \beta_V\mathbf{Q}_{n+1} - \mathbf{\Lambda}_V) \tag{3.18}$$

$$\mathbf{H}_V = (\beta_X\mathbf{U}_{n+1}'\mathbf{U}_{n+1} + \beta_V I) \tag{3.19}$$

$\underline{\mathbf{X} \text{ subproblem:}}$ Dropping all the terms independent of $\mathbf{X}$ we get

$$\begin{aligned}\arg\min_{\mathbf{X}} \frac{\beta_X}{2}\|\mathbf{X}-\mathbf{UV}\|_F^2 + \mathbf{\Lambda}_X'(\mathbf{X}-\mathbf{UV}) \\ +\frac{\beta_Z}{2}\|\mathbf{Z}-\mathbf{CX}\|_F^2 + \mathbf{\Lambda}_Z'(\mathbf{Z}-\mathbf{CX})\end{aligned} \tag{3.20}$$

The closed form solution to the above minimization problem is given by

$$\mathbf{X}_{n+1} = \mathbf{H}_X^{-1}(\beta_X \mathbf{U}_{n+1}\mathbf{V}_{n+1} - \mathbf{\Lambda}_X + \beta_Z \mathbf{C}'\mathbf{Z}_n + \mathbf{C}'\mathbf{\Lambda}_Z) \tag{3.21}$$

$$\mathbf{H}_X = \beta_X I + \beta_Z \mathbf{C}'\mathbf{C} \tag{3.22}$$

$\underline{\mathbf{Z} \text{ subproblem:}}$ Writing the Eq. 3.9 with respect to $\mathbf{Z}$ (ignoring constants independent of $\mathbf{Z}$) we get,

$$\arg\min_{\mathbf{Z}} \|SF\mathbf{Z}-\mathbf{b}\|_F^2 + \frac{\beta_Z}{2}\|\mathbf{Z}-\mathbf{CX}\|_F^2 + \mathbf{\Lambda}_Z'(\mathbf{Z}-\mathbf{CX}) \tag{3.23}$$

This problem is a Fourier domain replacement problem which can be solved analytically as shown below.

$$\mathbf{Z}_{n+1} = \mathbf{F}'\left[\left(S+\frac{\beta_Z}{2}I\right)^{-1}\mathbf{F}\left(\frac{\beta_Z}{2}C\mathbf{X}_{n+1} - \frac{\mathbf{\Lambda}_Z}{2} + \mathbf{F}'\mathbf{Sb}\right)\right] \tag{3.24}$$

We update all the Lagrange multipliers using a steepest ascent method at each iteration as shown below.

$$\mathbf{\Lambda}_{V(n+1)} = \mathbf{\Lambda}_{Vn} + \beta_V\ (\mathbf{V}_{n+1} - \mathbf{Q}_{n+1}) \tag{3.25}$$

$$\mathbf{\Lambda}_{X(n+1)} = \mathbf{\Lambda}_{Xn} + \beta_X\ (\mathbf{X}_{n+1} - \mathbf{U}_{n+1}\mathbf{V}_{n+1}) \tag{3.26}$$

$$\mathbf{\Lambda}_{Z(n+1)} = \mathbf{\Lambda}_{Zn} + \beta_Z\ (\mathbf{Z}_{n+1} - \mathbf{C}_{n+1}\mathbf{X}) \tag{3.27}$$

The optimization algorithm in Eq. 3.8 is solved by cycling between the above subproblems. The matrix $\mathbf{H}_U$ and $\mathbf{H}_V$ are $R \times R$ and can be easily inverted. Since

$\mathbf{C}'\mathbf{C}$ is a diagonal, $\mathbf{H}_X$ matrix is also diagonal and is therefore easily inverted. Splitting the k-space and coil sensitivities ($\mathbf{F}$ and $\mathbf{C}$ components) from $\mathbf{UV}$ in the data fidelity term has led to separate matrix inverses involving $\mathbf{F}'\mathbf{F}$ and $\mathbf{C}'\mathbf{C}$ which are easier to compute. Since, all the steps can be solved analytically, the convergence is much faster than conventional iterative conjugate gradient steps. Although β_X and β_Z parameters do not affect the final solution, they can affect the convergence rate. These parameters were chosen empirically. Since we use the augmented Lagrangian framework for enforcing the constraint on the dictionary, it is not necessary for β_V to tend to ∞ for the constraint to hold, allowing faster convergence. The quality of reconstruction is affected by β_U parameters as the non-convex penalty is enforced using majorization. As discussed earlier, the majorization is only exact when $\beta_U \to \infty$. We initialize β_U to a small value and gradually increment it when the cost in Eq. 3.3 stagnates to a threshold level of 10^{-2}.

The pseudo-code of the algorithm is shown below.

Algorithm 3.3.1: FastBCS($\mathbf{S}, \mathbf{F}, \mathbf{C}, \mathbf{b}, \lambda$)

Input : $\mathbf{b}$, $\beta_X > 0$, $\beta_Z > 0$, $\beta_U > 0$

while $|\mathcal{C}_{\mathrm{n}} - \mathcal{C}_{\mathrm{n-1}}| > 10^{-5}\mathcal{C}_n$

do
- Initialize $\beta_V > 0$
- **while** $|\mathbf{V} - \mathbf{Q}|^2 > 10^{-5}$
  - **do**
    - Update $\mathbf{L} :\leftarrow Eq.[3.11]$
    - Update $\mathbf{U} :\leftarrow Eq.[3.13]$
    - Update $\mathbf{Q} :\leftarrow Eq.[3.16]$
    - Update $\mathbf{V} :\leftarrow Eq.[3.18]$
    - Update $\mathbf{Z} :\leftarrow Eq.[3.24]$
    - Update $\mathbf{X} :\leftarrow Eq.[3.21]$
    - Update $\mathbf{\Lambda}_V :\leftarrow Eq.[3.25]$
    - Update $\mathbf{\Lambda}_X :\leftarrow Eq.[3.26]$
    - Update $\mathbf{\Lambda}_Z :\leftarrow Eq.[3.27]$
    - $\beta_V = 5 * \beta_V$
- **if** $|\mathcal{C}_{\mathrm{n}} - \mathcal{C}_{\mathrm{n-1}}| < 10^{-2}\mathcal{C}_n$
  - **then** $\beta_U = 50 * \beta_U$

return $(\mathbf{U}, \mathbf{V})$

3.4 Experimental evaluation

To study the convergence rate of both the algorithms, we acquired a single slice fully sampled 2D dataset on a Siemens 3T Trio scanner using a turbo spin echo

(TSE) sequence with turbo factor (TF) of 8, matrix size = 128x128, FOV= 22x22cm^2, TR=2500ms, slice thickness =5mm, B_1 spin lock frequency=400Hz, bandwidth= 130Hz/pixel, and echo spacing of 12.2ms. A 12-channel phased array coil was used. $T_{1\rho}$ preparation pulse [33] and T_2 preparation pulse [34] were used prior to readout. The data was collected for 12 equispaced spin lock times (TSLs) and 12 equispaced echo times (TEs) values, both ranging from 10 ms to 120 ms. This provided a total of 24 parametric measurements. The dataset was undersampled using a Cartesian hybrid sampling pattern (acceleration of 1.5 using pseudo-random variable density sampling and an acceleration factor of 4 from uniform sampling pattern) giving a net acceleration of 6. The coil sensitivity maps were obtained using Walsh method for coil map estimation [35]. Both the algorithms were implemented in MATLAB on a quad core linux machine.

We compare the performance and convergence speed of both the algorithms using a Mean square error (MSE) metric given by

$$\text{MSE} = \left(\frac{\|\Gamma_{\mathbf{recon}} - \Gamma_{\mathbf{orig}}\|_F^2}{\|\Gamma_{\mathbf{orig}}\|_F^2} \right). \tag{3.28}$$

The regularization parameter λ of both the algorithms was chosen such that the error between reconstructions and the fully sampled data given by MSE was minimized. Comparisons were done for the optimal λ value of 0.05.

The reconstruction error vs CPU time is shown in Fig. 3.3(a). It is observed that proposed algorithm converges to almost the same solution in just 3 min. This is also demonstrated by the reconstructed images and $T_{1\rho}$ and T_2 parameter maps shown in Fig. 3.4. Every time, when the β in Eq. 3.4 is incremented, the condition

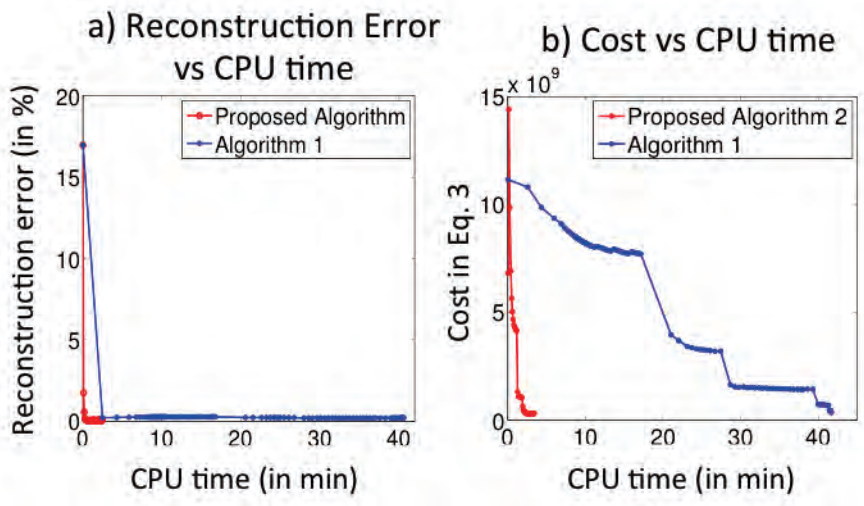

Figure 3.3: Convergence plots Convergence plots: Reconstruction error vs CPU time and the cost vs CPU time plots are shown in a) and b) respectively. It is observed that proposed algorithm converges to same solution in about 3 min where as the Algorithm 1 takes roughly 40 min to converge. Note the threshold in both algorithms was set to 10^{-6}

number of the $\mathbf{U}$ subproblem increases and the CG algorithm needs many iterations to converge thus increasing the reconstruction time considerably. This behavior can be seen in Fig. 3.3(b). In contrast the proposed algorithm takes much lesser time as it solves the subproblems analytically. The proposed algorithm converges in about 146 secs ($\approx$ 3 min) while the Algorithm 1 takes about 2500 secs ($\approx$ 40 min) resulting in 10 fold acceleration without much degradation in image quality.

3.5 Conclusion

In this paper , we have demonstrated the usage of simple splitting strategies to offer significant speed up in synthesis based dictionary learning optimization problems. We have demonstrated it to show considerable improvement in cases of parallel

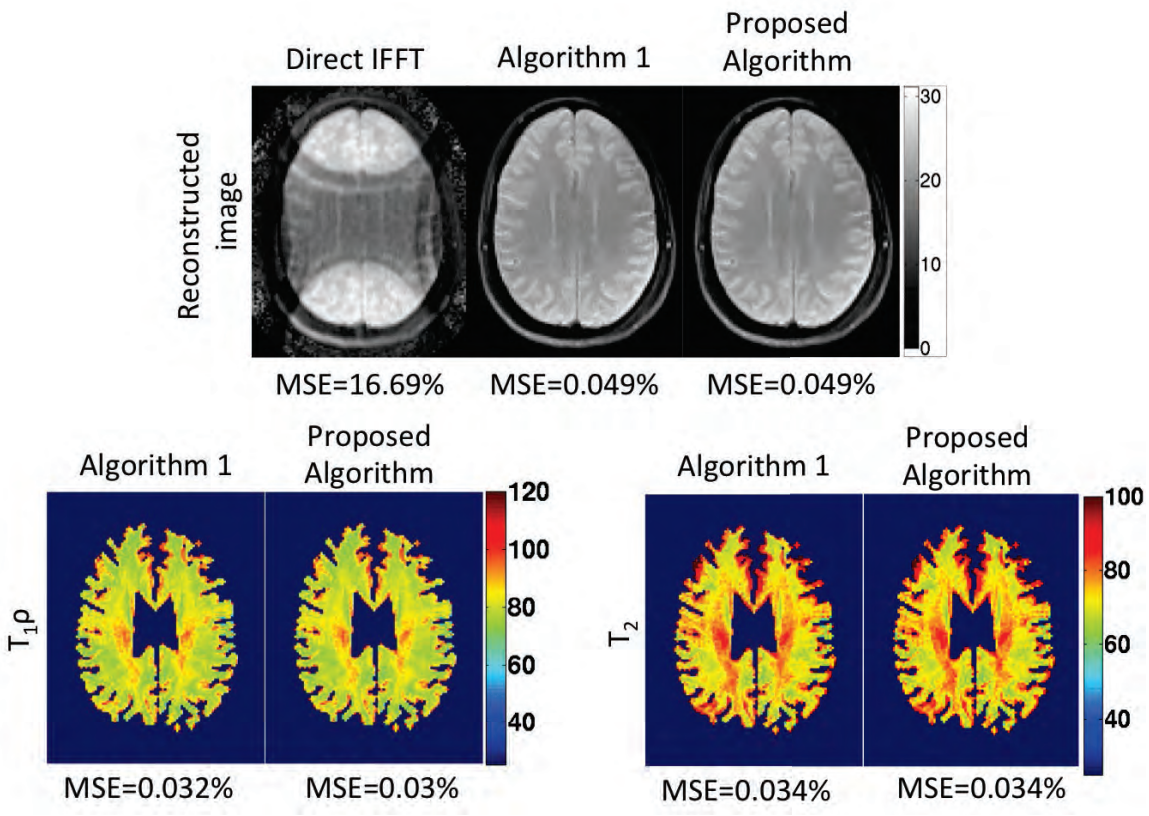

Figure 3.4: Qualitative results Qualitative results: The first row shows reconstructed images using Direct ifft, Algorithm 1 and the Proposed algorithm in a-c. The second and the third row show $T_{1\rho}$ and T_2 parameter maps for Algorithm 1 and proposed Algorithm respectively. It is seen that proposed algorithm converges 10 times faster without degradation in quality as compared to the Algorithm 1

MRI, at least a speed up factor of 10 fold.

CHAPTER 4
ACCELERATED WHOLE-BRAIN MULTI-PARAMETER MAPPING USING BLIND COMPRESSED SENSING

4.1 Introduction

In this chapter, we study the utility of multi-coil blind compressed sensing scheme introduced in the previous chapter to accelerate whole brain $T_1\rho$ and T_2 multi-parameter mapping. The quantification of multiple tissue parameters from MRI datasets is emerging as a powerful tool for tissue characterization [36–43]. Parameters such as proton density, longitudinal and transverse relaxation times (denoted by T_1 and T_2), relaxation times in the rotating frame ($T_1\rho$ and $T_2\rho$), as well as diffusion have been shown to be useful in diagnosis of various diseases including cerebral ischemia [44], Parkinson's disease [37–39], Alzheimer's disease [37,40,42], epilepsy [42] multiple sclerosis [41, 42], edema [43], necrosis [43], liver fibrosis [45], and intervertebral disc and cartilage degeneration [46–48]. Although a single parameter may be sensitive to a number of tissue properties of interest, it may not be specific. Acquiring additional parameters can improve the specificity. The main bottleneck in the routine clinical use of multi-parameter mapping is the long scan time associated with the acquisition of MR images with multiple weightings or contrast values. In addition, long scan times are likely to result in motion induced artifacts in the data.

In a parameter imaging, the k-space data corresponding to different image contrasts are often sequentially acquired by manipulating the sequence parameters (e.g. echo time, spin lock duration/amplitude and flip angle). The more the number

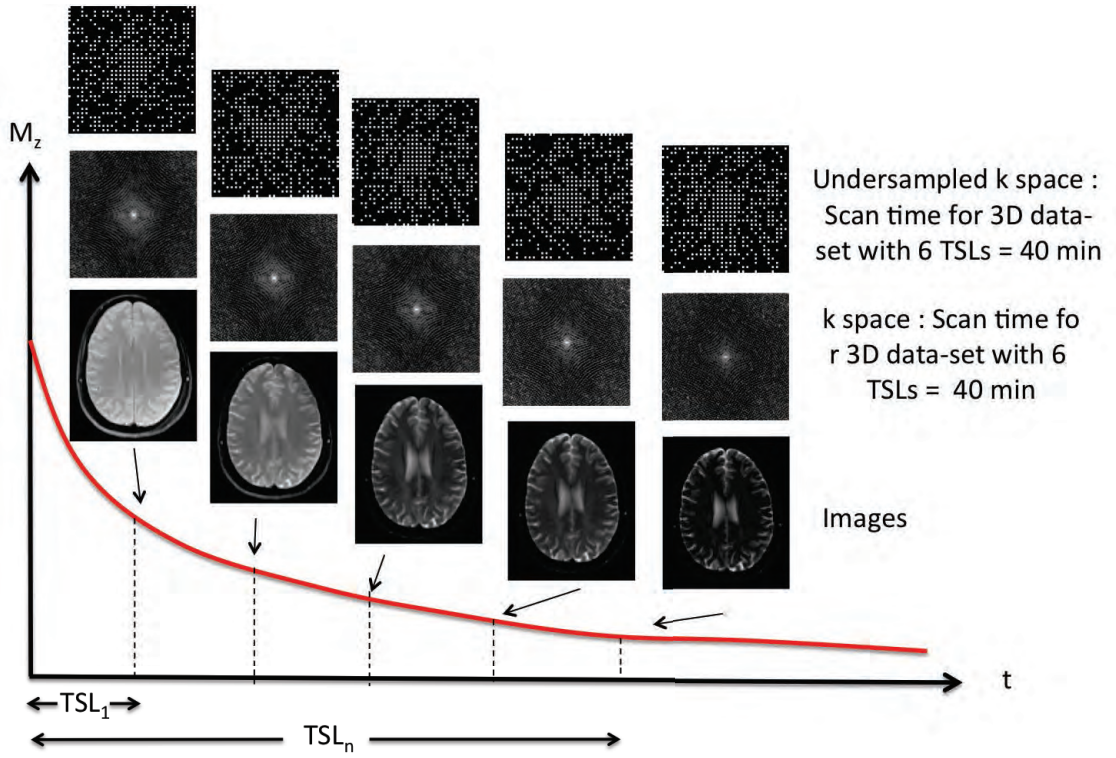

Figure 4.1: $T_1\rho$ imaging acquisition $T_1\rho$ imaging acquisition: The curve in red shows the exponential signal whose decay constant is $T_1\rho$. One image is acquired for each of the TSL values shown by dotted lines. Note: The fully sampled 3D acquisition takes $\approx$ 160 min while 8 fold undersampled acquisition takes 20 min.

of images along the exponential curve, the better the accuracy in the estimation of the decay constant. Fig. 4.1 shows an example of the acquisition process for $T_1\rho$ imaging. However, due to the limits in the scan time, there is often a tradeoff between spatial resolution and accuracy in parameter estimation.

A common approach to reduce the scan time is to limit the number of weighted images from which the parameters are estimated. However, this approach precludes the use of multi-exponential fitting methods, limits the accuracy of fits, and restrict the dynamic range of estimated tissue parameters. Several researchers have proposed

to accelerate the acquisition of the weighted images using parallel imaging, model-based compressed sensing, and low-rank signal modeling [10, 20, 23, 49–54]. The use of parallel imaging alone can only provide moderate acceleration factors [49]. Model-based compressed sensing methods rely on large dictionaries generated by Bloch equation simulations of all possible parameter combinations [55]. A challenge associated with this scheme is its vulnerability to patient motion, mainly because the dictionary basis functions cannot account for motion induced signal changes. Another problem with the direct application of this scheme to multi-parameter imaging is the rapid growth in the size of the dictionaries with the number of parameters, which also results in increased complexity of the non-linear recovery algorithm. In this context, methods such as k-t PCA and PSF models that estimate the basis functions from the measured data itself are more desirable; the basis functions can model motion induced signal changes and thus provide improved recovery of weighted images [23, 56].

The BCS algorithm [28] was inspired by the theoretical work on BCS by Gleichman et al. [57]. The work by Gleichman et. al. considers the same sensing matrix for all time frames, for simplicity of the derivations. The proposed scheme uses different sensing matrices for different frames. The experiments in [26, 28] clearly demonstrate the benefit of higher spatial and temporal incoherency offered by this sampling strategy. In addition, the algorithm used in [57] is fundamentally different from our setting. The proposed scheme is also motivated by and have similarities to the partial separable function (PSF) model introduced by Liang et al. [10, 56, 58]. However, there are several key differences between the PSF implementations and the

proposed scheme. For example, [56] uses the power factorization method to exploit the low-rank structure of $\mathbf{\Gamma}$. They jointly estimate $\mathbf{U}$ and $\mathbf{V}$ by alternating between two quadratic optimization schemes involving data consistency terms. Our previous work shows that the BCS scheme provides improved reconstructions than low-rank methods, including power-factorization [28, 56], mainly because of the richer dictionary and the lower degrees of freedom. Zhao et. al, assumes the data to be low-rank and pre-estimates the orthogonal basis set $\mathbf{V}$ from low resolution data [58]; they then estimate the coefficients using a sparsity penalty on $\mathbf{U}$. This approach can be seen as the first step of our iterative algorithm to jointly estimate $\mathbf{U}$ and $\mathbf{V}$. Specifically, the joint estimation of $\mathbf{U}$ and $\mathbf{V}$ will provide a richer dictionary with non-orthogonal basis functions, which provide sparser coefficients than the orthogonal basis functions in [58]. This is not unexpected since extensive research in image processing have shown that over-complete and non-orthogonal dictionaries/frames offer more compact representations than orthogonal basis sets.

We study the utility of the proposed BCS scheme to simultaneously recover $T_1\rho$ and T_2 maps from under-sampled weighted images. We rely on Cartesian sub-sampling schemes. The proposed scheme yields reasonable estimates from the whole-brain for eight fold under-sampling over the fully-sampled setup, thereby reducing the scan time to 20 min.

4.2 Methods

4.2.1 Data acquisition

To demonstrate the utility of the proposed BCS scheme in recovering $T_1\rho$, T_2 and S_0 parameters, healthy volunteers were scanned on a Siemens 3T Trio scanner (Siemens Healthcare, Erlangen, Germany) using a vendor provided 12-channel phased array coil. Written informed consent was obtained and the study was approved by the Institutional Review Board. The coil sensitivity maps were obtained using the Walsh method for coil map estimation [35].

To test the feasibility of the algorithm and to optimize the parameters, we first acquired a single-slice fully-sampled axial 2D dataset using a turbo spin echo (TSE) sequence, combined with $T_1\rho$ preparatory pulses [33] and T_2 preparatory pulses [34]. Scan parameters were turbo factor (TF) of 8, matrix size = 128x128, FOV= 22x22cm^2, TR=2500ms, slice thickness =5mm, B_1 spin lock frequency=330Hz, and bandwidth= 130Hz/pixel. $T_1\rho$ and T_2 weighted images were obtained by changing the duration of the $T_1\rho$ (referred as spin lock time) and duration of the T_2 preparation pulses (referred as echo time) respectively. The data was collected for 12 equi-spaced spin lock times (TSLs) and 12 equi-spaced echo times (TEs) values, both ranging from 10 ms to 120 ms. This provided a total of 24 parametric measurements. The scan time for this dataset was 16 min. Note that five or six spin lock times are sufficient for $T_1\rho$ estimation using a single exponential fit. However, our main motivation is the future use of this scheme for multi-parametric mapping (e.g. joint imaging of $T_1\rho$, T_2, $T_1\rho$ dispersion imaging, as well as time-resolved parametric mapping). The proposed

scheme will prove very useful in these settings. Moreover, larger number of parametric images are essential for more sophisticated models such as multi-exponential model to account for partial volume issues.

To demonstrate the utility of the approach in accelerated 3-D imaging, we acquired a prospective 3D dataset using a segmented 3D gradient echo sequence based on the 3D MAPSS approach [59]. Scan parameters were FOV = 22x22x22cm^3, matrix size = 128x128x128, 64 lines/segments, TR/TE=5.6/2.53ms, recovery time=1500ms, resolution 1.7mm isotropic, bandwidth= 260Hz/pixel, B_1 spin lock frequency =330Hz and constant flip angle=10^o. The readout (frequency encode) direction was (k_x), which enabled us to choose an arbitrary sampling pattern. TEs and TSLs of the T_2 and $T_1\rho$ preparation pulses were varied uniformly from 10 to 100ms providing 10 measurements of each. Scan time of the prospective 3D dataset was 20 min. To be consistent with the 2D dataset the phase encoding plane (phase encode, slice encode) was oriented along the axial ($k_y - k_z$) plane. We perform the recovery of each $y - z$ slice independently.

4.2.2 Optimization & validation of the algorithm using fully sampled 2-D acquisition

We used the fully sampled 2-D dataset to determine an optimal sampling pattern, optimize the parameters, and compare with other algorithms.

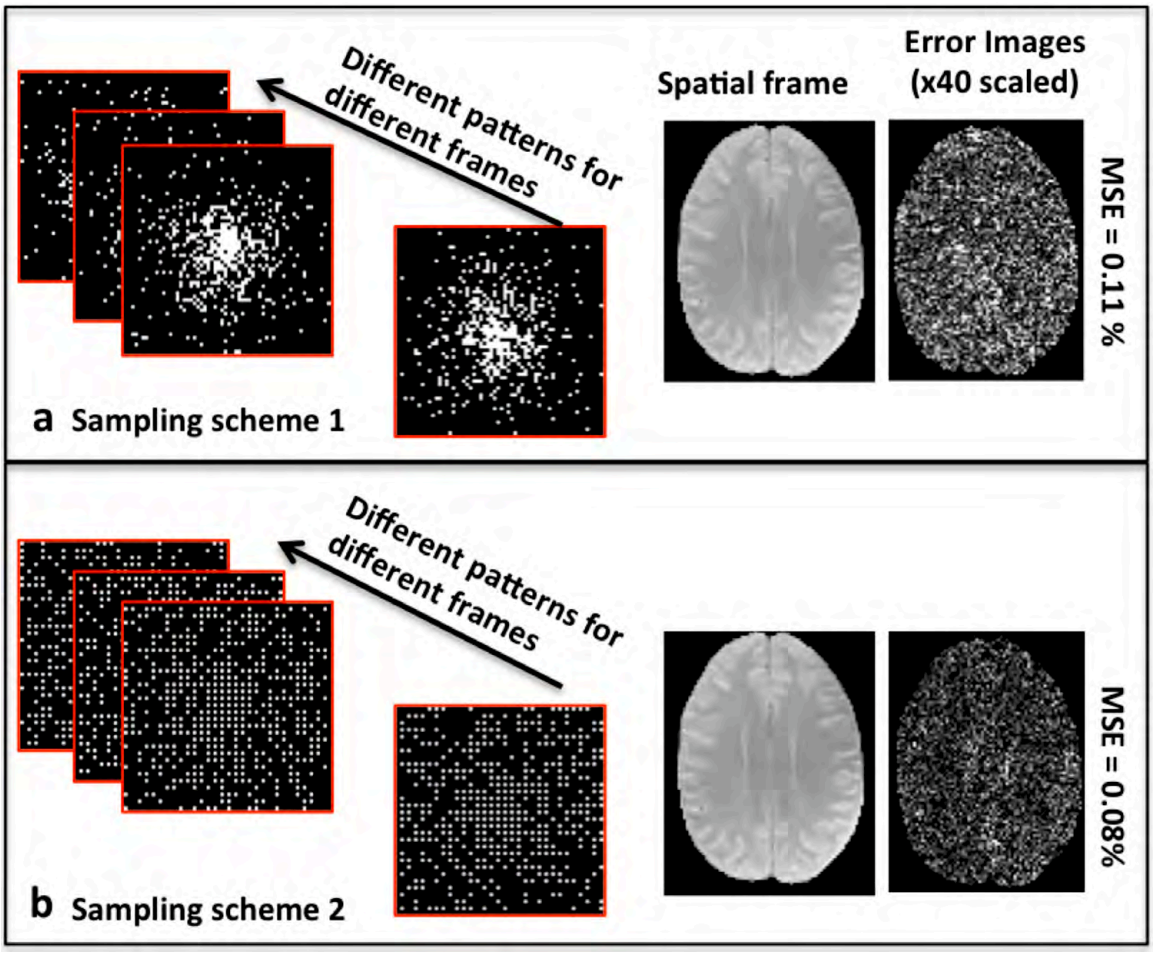

Figure 4.2: Choice of sampling trajectories Choice of sampling trajectories: The sampling patterns for a specific frame for the two choices of sampling schemes are shown in (a) and (b), respectively. The results are shown for an under-sampling factor of 8. The first sampling scheme (shown in (a)) is a pseudo-random variable density pattern, while the second sampling scheme (shown in (b)) is a combination of a uniform 2x2 under-sampling pattern and a pseudo-random variable density pattern. The second column shows one of the weighted images of the reconstructed data using BCS. As seen from the error images in third column, sampling scheme 2 yields better performance. Note that the sampling patterns are randomized over different parameter values to increase incoherency.

4.2.2.1 Determination of a sampling scheme

To choose an optimal sampling scheme that will work well with the multi-channel BCS scheme, we retrospectively under-sample the 2-D dataset using two

different under-sampling schemes shown in Fig. 4.2(a-b). Both patterns correspond to an 8 fold under-sampling. Fig. 4.2(a) shows the pseudo-random variable density trajectory which over-samples the center of k-space. The sampling scheme 2 as shown in Fig. 4.2(b) is a combination of a 2x2 uniform Cartesian under-sampling pattern and a pseudo-random variable density pattern as in Fig. 4.2(a). Acceleration factor of 6,8,10 and 12 were achieved as 4- fold uniform under-sampling and 1.5, 2, 2.5 and 3 fold random variable density under-sampling respectively. The 2x2 uniform sampling pattern for different frames is randomly integer shifted in the range $[x, y] = [-1, 1]\times[-1, 1]$ as done in [60] to achieve more incoherency. This sampling scheme may be replaced with Poisson disc sampling [61]. We compare the reconstructions provided by the proposed algorithm from the dataset under-sampled using both schemes.

4.2.2.2 Details of algorithms & determination of their parameters

We compare the BCS algorithm against compressed sensing (CS) [15] and k-t principal component analysis (PCA) [23] methods. A training dataset of 10000 exponentials is generated assuming the exponential model in Eq. [4.3] for the CS scheme. A dictionary of 1000 atoms is learned from the training dataset using k-SVD algorithm [62]. Specifically, we vary the T_2 and $T_1\rho$ values from 1ms to 300ms in steps of 3. The learned dictionary is then optimized for signal approximation with at most K atoms. The sparsity value K is chosen as 7 based on the model fit with respect to fully sampled dataset. The dictionary learned from the training phase is used in the reconstruction. The data is reconstructed using an iterative procedure,

which iterates between obtaining the K-term estimate of the signal using orthogonal matching pursuit (OMP) algorithm and minimizing data consistency as described in [15]. kt-PCA is implemented as a two step approach where the first step is to estimate the orthogonal basis functions from the training data. The basis functions are estimated from the center 9x9 grid of the fully-sampled k-space data using PCA. In the second step, the estimated basis functions are used in reconstruction of the data. We also compare the BCS algorithm with the kt-PCA method with ℓ_1 sparsity constraint enforced on the coefficients. The algorithms are implemented in MATLAB on a quad core linux machine with a NVDIA Tesla graphical processing unit. The regularization parameters of all the algorithms were chosen such that the error between reconstructions and the fully-sampled data specified by

$$\text{MSE} = \left(\frac{\|\Gamma_{\mathbf{recon}} - \Gamma_{\mathbf{orig}}\|_F^2}{\|\Gamma_{\mathbf{orig}}\|_F^2} \right) \tag{4.1}$$

is minimized. We iterate all algorithms until convergence (until the change in the criterion/cost function is less than a threshold which is 10e-6). With this setting, kt- PCA takes about 10-15 iterations, kt-PCA with ℓ_1 constraint takes 7-8 iterations, BCS takes 60-70 iterations while CS takes around 100 iterations to converge.

We also compare the BCS and kt-PCA methods for their compression capabilities. The 2D dataset with and without motion is represented using different number of basis functions in case of kt-PCA and different regularization parameters (and equivalently different sparsities) in case of BCS. For BCS model we considered

dictionary $\mathbf{V}_{us}$ estimated from 6 fold under-sampled data. To determine the model representation at different compression factors we solved for the model coefficients $\mathbf{U}$ using the following equation:

$$\hat{\mathbf{U}}_\lambda = \arg\min_{\mathbf{U}} \|\mathbf{\Gamma} - \mathbf{U}\mathbf{V}_{us}\|_2^2 + \lambda\|\mathbf{U}\|_{\ell_1} \tag{4.2}$$

We varied the range of λ and minimized the above problem to control the sparsity levels of $\hat{\mathbf{U}}_\lambda$, and hence the compression capabilities. A threshold of 0.1 % was applied on $\hat{\mathbf{U}}_\lambda$ to shrink the coefficients that were very small and were not fully decayed to zero during the above ℓ_1 minimization problem. The model approximation error is given by $\|\mathbf{\Gamma} - \mathbf{U}_\lambda\mathbf{V}_{\mathbf{us}}\|_F^2$.

4.2.2.3 Comparison of the algorithms

We estimate the parameters S_0, $T_1\rho$ and T_2 by fitting the mono-exponential model

$$M(p) = S_0 \,.\, \exp\left(\frac{-\mathrm{TE}(c)}{T_2}\right) \,.\, \exp\left(\frac{-\mathrm{TSL}(c)}{T_{1\rho}}\right) \tag{4.3}$$

to the reconstructed images on a pixel by pixel basis using a linear least-squares algorithm.The mean square error (MSE) of the parameter maps obtained from the BCS, CS and kt-PCA algorithms are compared to the ones obtained from the fully-sampled data. We mask the reconstructed images before computing the parameter maps to limit our evaluation of $T_1\rho$, T_2 and S_0 to the brain tissue.

The performance of the reconstruction scheme at higher acceleration was as-

sessed by retrospectively under-sampling the dataset at acceleration factors of 6, 8, 10, 12 & 15 using the sampling scheme shown in Fig. 4.2(b). To determine the robustness of the proposed scheme to motion, we constructed a simulated dataset with inter-frame motion by adding translational motion resulting in 1 pixel shift and rotational motion of 1 degree to frames 16-21 of the 2D dataset, out of 24 frames. The reconstructed images are aligned to compensate for inter frame motion, prior to fitting. To demonstrate the advantage of acquiring multiple parameters over single parameter, we compared the $T_1\rho$ maps obtained by applying BCS, kt-PCA and CS schemes on the combined dataset $(T_1\rho + T_2)$ and the $T_1\rho$ only dataset.

4.2.3 Validation of the BCS algorithm using prospective 3D acquisition

The prospectively under sampled 3-D dataset is recovered using the BCS scheme. The dataset was under-sampled on a Cartesian grid with a acceleration factor of R=8 using the under-sampling scheme 2. Each of the 128 slices in the dataset are recovered independently using BCS. The parameter maps are estimated from the pixels by fitting the mono-exponential model to the data. The MSE metric could not be used for the 3D experiments as the fully-sampled ground truth was not available. Hence, we determine the regularization parameter λ using the L-curve strategy [63].

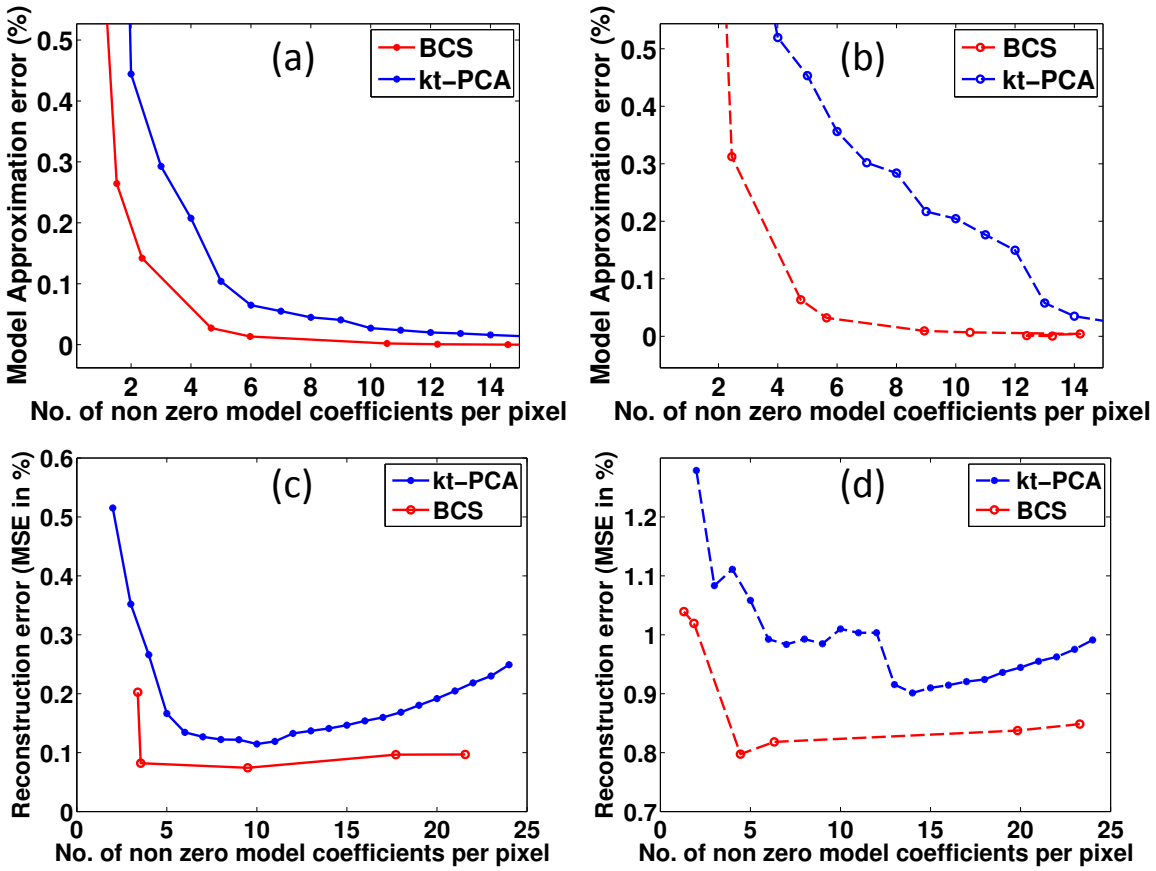

Figure 4.3: Comparison of BCS and kt-PCA model representation Comparison of BCS and kt-PCA model representation: (a) and (b) show the model approximation error against the number of non-zero coefficients per pixel of BCS and kt-PCA without and with motion respectively. (c) and (d) show the reconstruction error against the average number of non-zero model coefficients per pixel of BCS and kt-PCA models on the 2D dataset without and with motion respectively. We observe that BCS gives better reconstructions with less number of non-zero model coefficients than kt-PCA both in case of with and without motion. In other words the degree of freedom of BCS is less than that of kt-PCA. BCS model gives better compression than kt-PCA model as seen from (a) & (b). Note: For (a)&(b), the basis functions in case of BCS were estimated from 6 fold under-sampled data and the basis functions of kt-PCA were estimated from center of k-space of the fully sampled data.

4.3 Results

4.3.1 Fully sampled 2D acquisition

The comparisons of the two under-sampling patterns at acceleration factor of 8 is shown in Fig. 4.2. The MSE values and the error images in third column show that

sampling scheme 2 (shown in Fig. 4.2(b)) provides better reconstructions. Sampling scheme 2 samples outer k-space more than sampling scheme 1 (shown in Fig. 4.2(a)), which reduces blurring of the high frequency edges. In other words, the sampling scheme 2 is both randomly and uniformly distributed in k-space making it suitable for multi-channel compressed sensing applications. The aliasing introduced by the 2x2 uniform grid in sampling scheme 2 is resolved using information from multiple coils. Using different sampling patterns for different frames increases incoherency and thus helps in better reconstructions. We use sampling scheme 2 for all the subsequent experiments.

We demonstrate the choice of the parameters in BCS and k-t PCA schemes in Fig. 4.3 using 8 fold retrospectively under sampled data. The comparisons were done in two regimes: one where the subject was still, and one with head motion during part of the scan. In Fig. 4.3(a)&(b), we show the model approximation error as a function of number of non-zero coefficients per pixel while representing the 2D dataset without and with motion for BCS and kt-PCA using learned basis functions respectively. In case of BCS scheme, the basis functions learned from BCS reconstruction of 6-fold under-sampled data were used whereas in case of kt-PCA, basis functions estimated from center k-space of the fully sampled data were used. We observe that BCS provides better compression capabilities than kt-PCA. In other words, the model fitting error in BCS is lower with less number of non-zero coefficients per pixel as compared to kt-PCA. We observe from Fig. 4.3(c)&(d) that the better signal representation offered by BCS translates to better reconstruction. Specifically,

the optimal number of non-zero coefficients that yield minimum reconstruction errors in the kt-PCA model (10 in case without motion and 14 for case with motion) is considerably higher than that of BCS model (≈4 in case without motion and ≈5 in case with motion).

In Fig. 4.4, we compare the performance of BCS against k-t PCA scheme with and without sparsity constraint and CS schemes for different acceleration factors without motion (right) and in the presence of motion (left). We observe that BCS is capable of providing reconstructions with lower errors, compared with CS and k-t PCA schemes with and without sparsity constraint. The better performance of BCS in cases without and with motion can be attributed to the richer dictionary and lower degrees of freedom over other methods.

The ℓ_1 norm on the coefficients and Frobenius norm constraint on the dictionary attenuate the insignificant basis functions which model the artifacts and noise as shown in Fig. 4.5(a) and thereby minimize noise amplification. In contrast, since the model order (number of non-zero coefficients) in kt-PCA without sparsity constraint is fixed a priori, basis functions modeling noise are also learned, especially in the case with motion. This is demonstrated in Fig. 4.5(c). Imposing a sparsity constraint on $\mathbf{U}$ in kt-PCA method improves the results over kt-PCA without regularization. This scheme can be seen as the first iteration of the BCS scheme. The results in the paper clearly demonstrate the benefit in re-estimating the basis functions. Specifically, the BCS scheme enables the learning of non-orthogonal basis functions, which provide sparser coefficients. The CS method on the other hand exhibited motion artifacts as

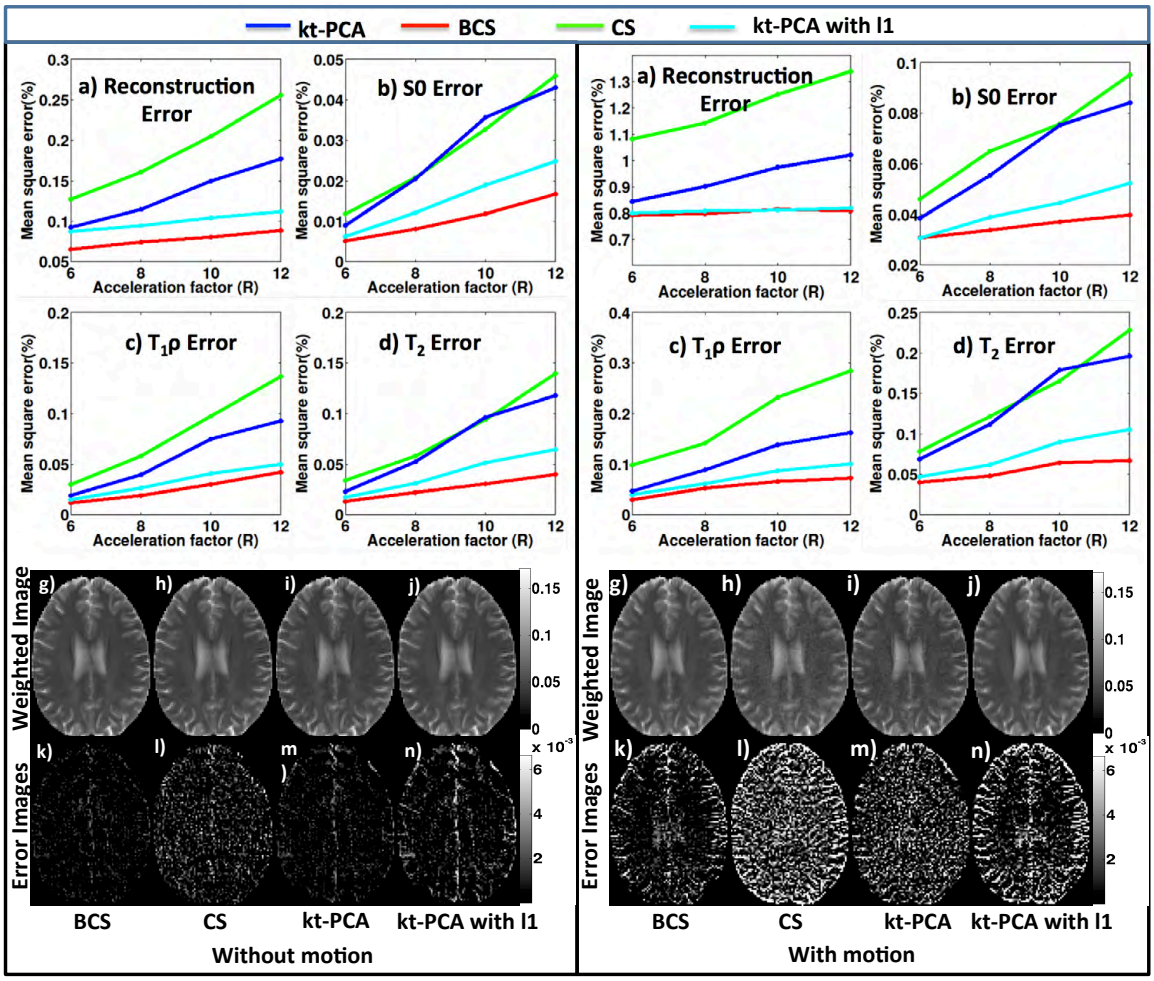

Figure 4.4: Comparison of the proposed BCS scheme with different reconstruction schemes on retrospectively under-sampled 2D dataset Comparison of the proposed BCS scheme with different reconstruction schemes on retrospectively under-sampled 2D dataset: The results for dataset without and with motion are shown in (i) and (ii) respectively. The plots for reconstruction error, S_0 map error, $T_1\rho$ map error and T_2 map error for BCS, CS, kt-PCA and kt-CPA with ℓ_1 sparsity schemes are shown in (a-d). It is observed that the BCS scheme provides better recovery in both cases. The images in (g-j) show one weighted image of the reconstructed dataset at acceleration factor of 8 using the 4 different schemes. We observe that the CS and kt-PCA schemes were sensitive to motion and resulted in spatial blurring as seen in (ii)- (h-j), which is also evident from the error images.

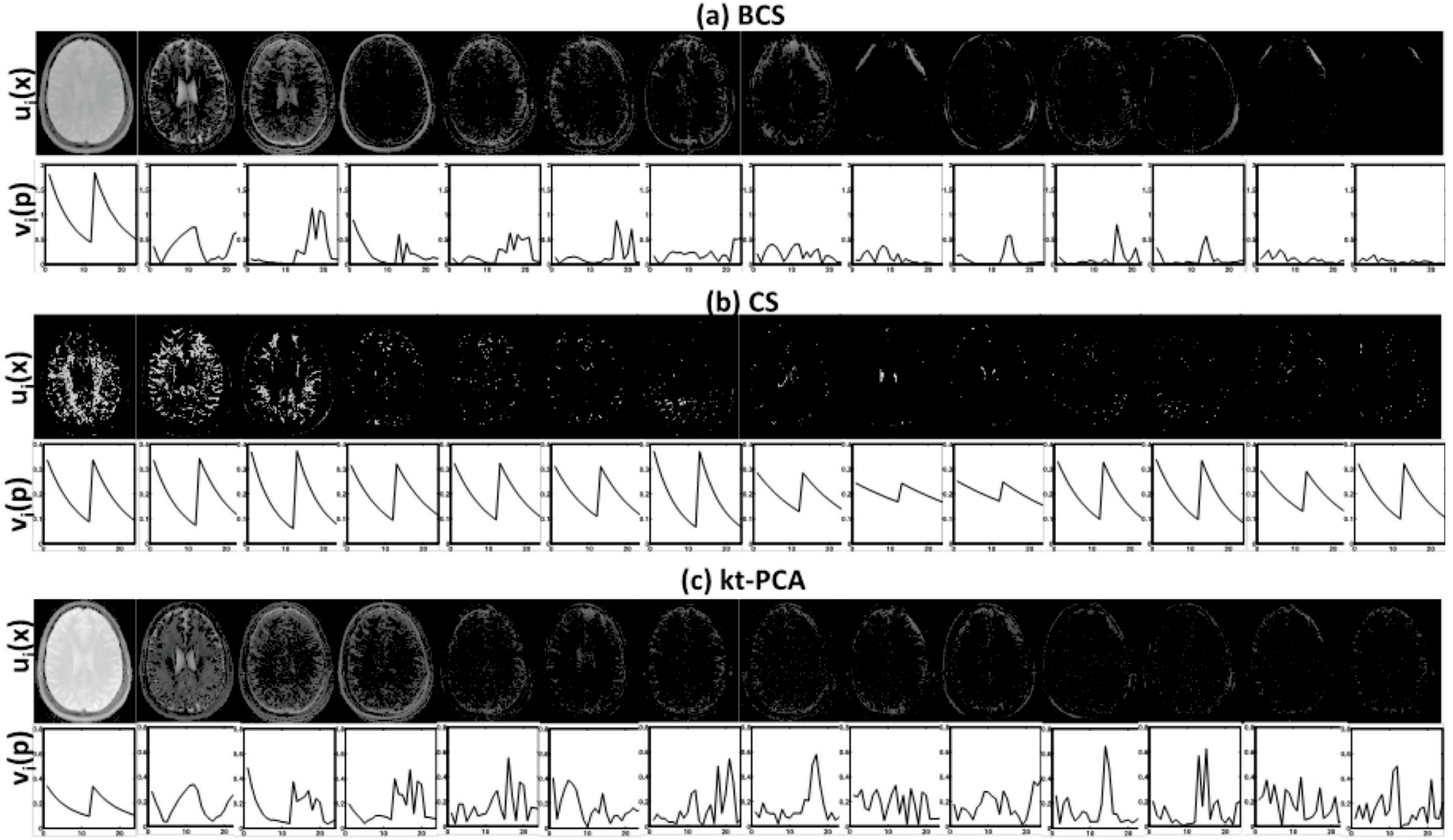

Figure 4.5: Model Coefficients and dictionary basis functions for the 2D data with motion Model Coefficients and dictionary basis functions for the 2D data with motion: Few spatial coefficients $\mathbf{u}_i(x)$ and their corresponding basis functions $\mathbf{v}_i(p)$ for BCS, CS and kt-PCA schemes are shown in a-c respectively. The product entries $\mathbf{u}_i(x)v_i(p)$ are sorted according to Frobenius norm and first 14 entries are shown here. Since the Frobenius norm constraint attenuates the insignificant basis functions BCS reconstructions have less noise amplification whereas the basis functions estimated using kt-PCA scheme are noisy.

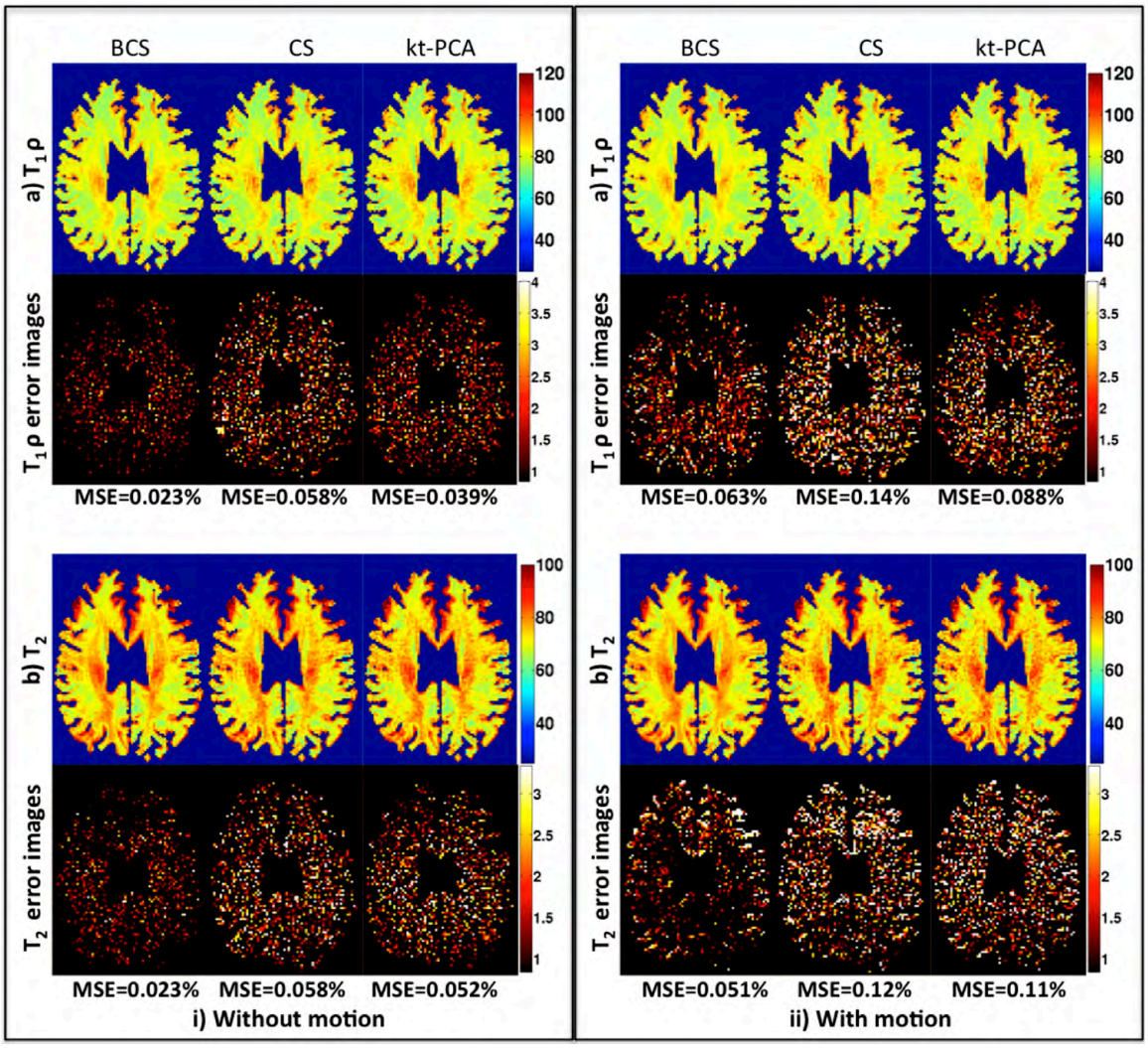

Figure 4.6: $T_1\rho$ and T_2 parameter maps for retrospectively under-sampled 2D dataset $T_1\rho$ and T_2 parameter maps for retrospectively under-sampled 2D dataset: The $T_1\rho$ and T_2 parameter maps obtained using BCS, CS and kt-PCA schemes on the 2D dataset with and without motion are shown in (i) and (ii) respectively. The maps are obtained at acceleration factor of 8. We observe that BCS scheme performs better than CS and kt-PCA schemes in both cases with and without motion. The noise in reconstructions using the kt-PCA and CS schemes propagates to the parameter maps and hence the degradation is higher in case of kt-PCA and CS as compared to BCS.

the dictionary is learned from the data model which does not contain signal prototypes that account for patient-specific motion fluctuations. The comparison of $T_1\rho$ and T_2

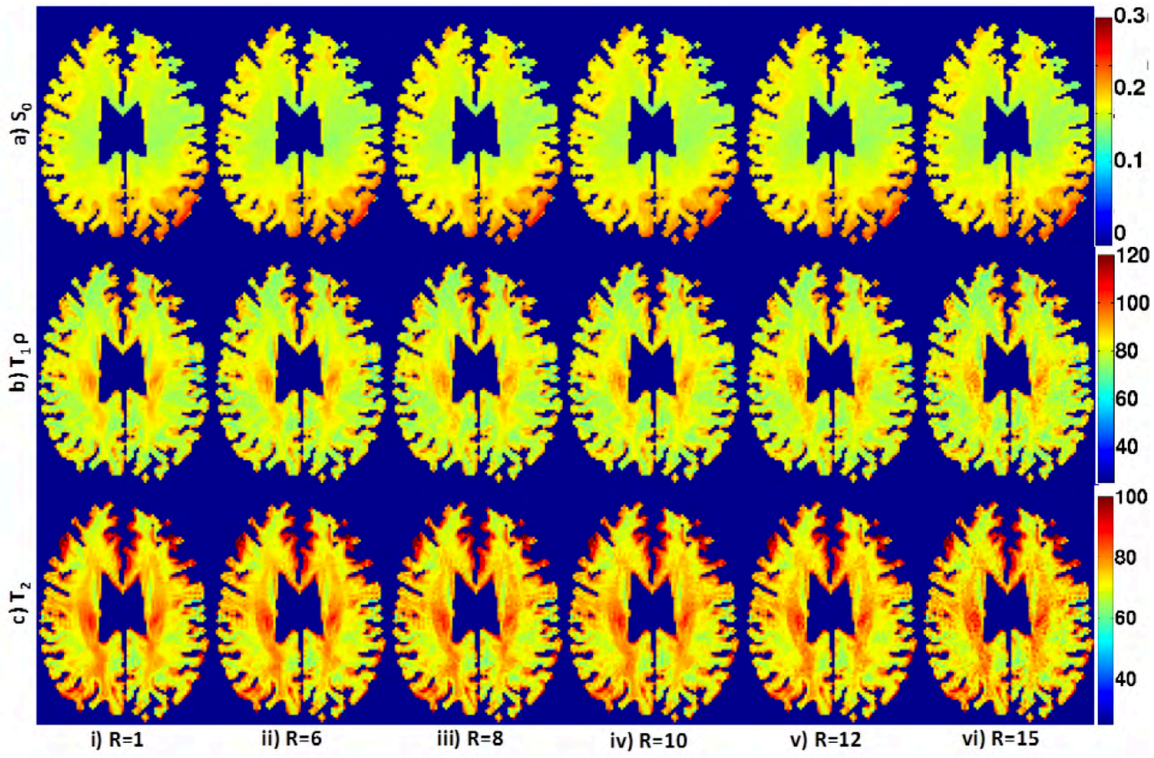

Figure 4.7: Parameter maps of a retrospectively under-sampled 2D dataset at different acceleration factors Parameter maps of a retrospectively under-sampled 2D dataset at different acceleration factors: S_0, $T_1\rho$ and T_2 parameter maps (a-c) at acceleration factors R=1, 6, 8, 10, 12 and, 15 are shown in (i-vi). We observe reasonable reconstructions for acceleration factors up to 15 with minimal degradation in contrast.

parameter maps at acceleration factor of 8 are shown in Fig. 4.6. We observe that BCS provides superior reconstructions which translate into better parameter maps as compared to other two schemes in both with and without motion datasets. Fig. 4.7 shows the parameter maps for different acceleration factors. Acceleration factors up to 15 were achieved with minimal degradation. All the schemes yield better $T_1\rho$ maps in case of the combined $(T_1\rho + T_2)$ dataset as compared to the only $T_1\rho$ dataset as seen in Fig. 4.8. In addition, we observe that BCS gives better performance than

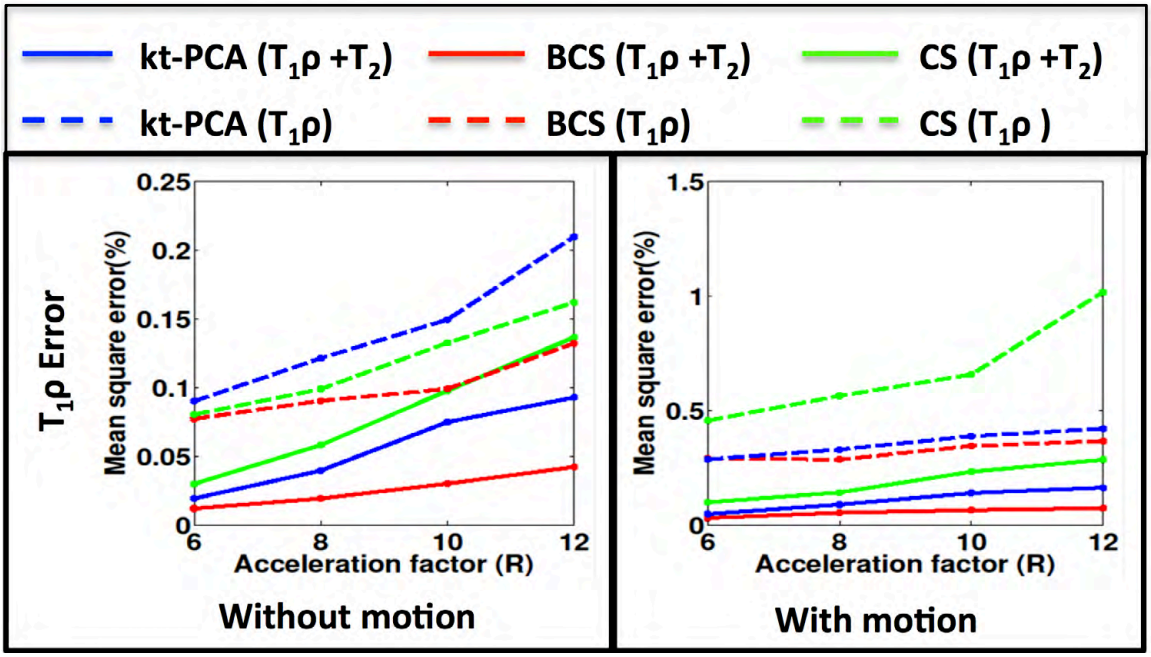

Figure 4.8: Comparison of $T_1\rho$ maps errors obtained from reconstructions of combined $(T_1\rho + T_2)$ dataset and the $T_1\rho$ only dataset Comparison of $T_1\rho$ maps errors obtained from reconstructions of combined $(T_1\rho + T_2)$ dataset and the $T_1\rho$ only dataset: The $T_1\rho$ maps errors at different accelerations for all the schemes on the combined dataset (solid lines) and only $T_1\rho$ dataset (dotted lines) are shown. The plot on left shows comparisons for the datasets without any motion and the plot on the right shows comparisons for datasets with motion. We observe in both cases that BCS performs better than CS and kt-PCA schemes. In other words combining the datasets improves the reconstructions.

other schemes, thus confirming that combining $T_1\rho$ and T_2 datasets does not affect the reconstructions, instead it enables to achieve higher acceleration and improves the specificity of $T_1\rho$.

4.3.2 Prospective 3D acquisition

The optimal regularization parameter is chosen using the L- curve method as shown in Fig. 4.9. The λ value of 0.07 is then used to recover all the slices. The

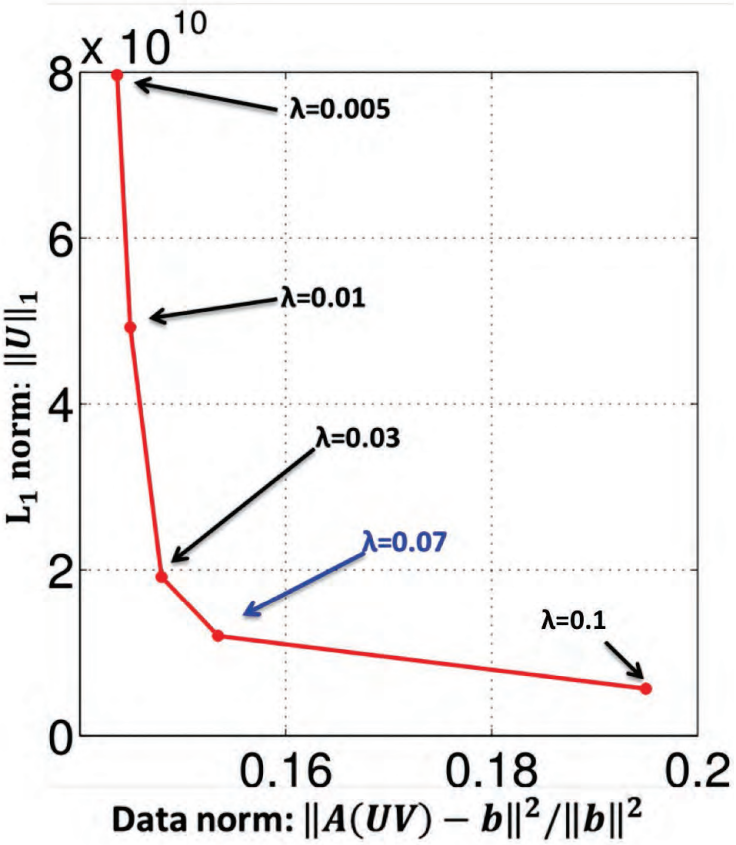

Figure 4.9: Choice of regularization parameter λ Choice of regularization parameter λ: The λ parameter was optimized using the L- curve strategy [63]. We change λ and plot the data consistency error against the smoothness penalty. λ value of 0.07 was chosen as the regularizing parameter for the 3D dataset.

parameter maps for the prospectively under-sampled 3D dataset recovered using the BCS scheme are shown in Fig. 4.10. We observe that the computation time for the 3D dataset using CG based algorithm 1 was >50 hours which is 10 times higher than the computation time using the variable splitting based algorithm. These results demonstrate that the BCS scheme yields good parameter maps with reasonable image quality in both cases. The acceleration factor of R=8 enables us to obtain reliable

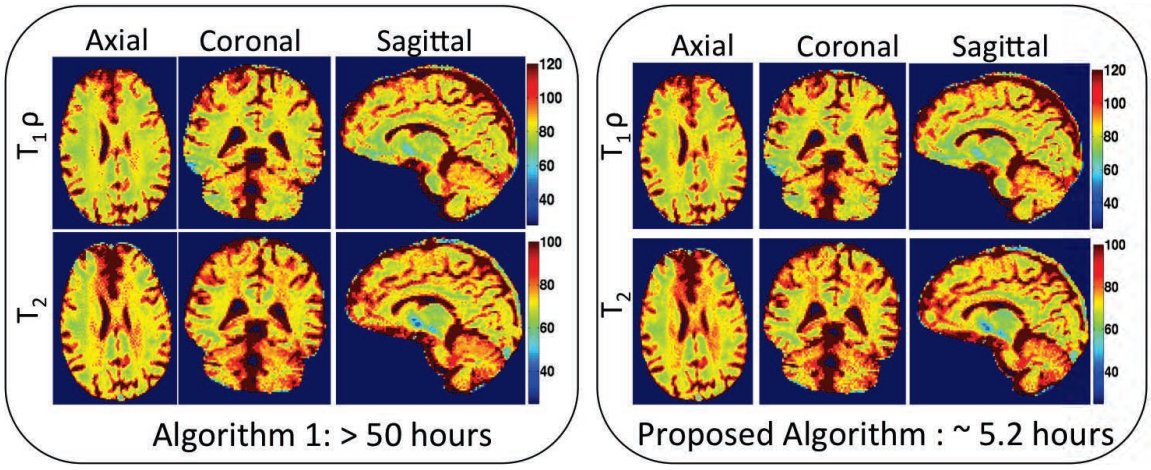

Figure 4.10: Parameter maps for 3D prospective under-sampled data at R=8 Parameter maps for 3D prospective under-sampled data at R=8: Axial, Coronal and Sagittal $T_1\rho$ and T_2 parameter maps estimated using reconstructions using Algorithm 1 (left) and proposed algorithm (right) are shown. With the acceleration of R=8, the scan time was reduced to 20 min. We observe that the proposed algorithm has a 10 fold speed up in computation time over the CG based algorithm 1 while maintaining same image quality. Note: All 128 slices were processed slice by slice to reconstruct the 3D parameter maps

$T_{1\rho}, T_2$ and S_0 estimates from the entire brain within a reasonable scan time (20 min).

4.4 Discussion

We have introduced a blind compressed sensing framework to accelerate multi-parameter mapping of the brain. The fundamental difference between CS schemes and the proposed framework is that BCS learns a dictionary to represent the signal, along with the sparse coefficients from the under-sampled data. This approach enables the proposed scheme to account for motion-induced signal variations. Since the number of different tissue types in the specimen is finite, this approach also enables use of smaller dictionaries, resulting in a computationally efficient algorithm. The main

difference of the proposed scheme vs. k-t PCA scheme is the non-orthogonality of the basis functions and the sparsity of the coefficients. The richer model and the fewer degrees of freedom due to the sparsity of the coefficients translate to lower artifacts at high acceleration factors.

Since the kt-PCA basis functions are estimated from the center 9x9 kspace of the fully sampled data, it does not exploit the redundancy due to parallel MRI. The kt-PCA performance may be further improved by a pre-reconstruction step, where the missing k-space data is interpolated from the known samples using GRAPPA [64] or SPIRiT [65], prior to estimating the basis functions. However, no such pre-reconstruction is necessary in BCS since the dictionary is updated iteratively with the coefficients in the reconstruction process. The kt-PCA reconstructions, specially in presence of motion can be improved by using the model consistency condition (MOCCO) technique [66] introduced recently. Such a model consistency relaxation could also be realized with the BCS model, which is yet to explored.

Our comparisons with kt-PCA and CS schemes in the case of subjects experiencing head motion shows that BCS is more robust to motion. This behavior can be attributed to the ability of the BCS scheme to learn complex basis functions that capture the motion-induced signal variations. The ability to be robust to motion induced signal variations is especially important in high-resolution whole-brain parameter mapping experiments, where the acquisition time can be significant.

Based on our work that combined low-rank and spatial smoothness priors [26], we observed that the use of spatial smoothness priors along with low-rank priors as

in Zhao et. al, ISMRM, 2012 can provide better reconstructions. While spatial smoothness priors can be additionally included with BCS to improve performance, this is beyond the scope of this paper.

Recently, a new scheme was proposed for accelerating $T_1\rho$ mapping which learns the dictionary from the principal component coefficients [67]. The k-SVD algorithm [62] is used to update the dictionary and the sparse representation. We had compared our BCS formulation with a similar scheme which used K-SVD algorithm to update the dictionary in the context of dynamic imaging [28]. The comparisons revealed that the k-SVD scheme is highly sensitive to local minima compared to the proposed scheme. The sensitivity can be attributed to the greedy nature of the k-SVD algorithm and the absence of continuation schemes. Another drawback of the k-SVD algorithm in the under-sampled setting is the likelihood of the dictionary atoms learning alias patterns at high acceleration factors [28]. The unit Frobenius norm constraint in our algorithm provides an implicit model order selection, thereby attenuating insignificant basis functions, unlike the unit column norm dictionary constraints used by k-SVD. The proposed algorithm is also considerably more computationally efficient than the alternating k-SVD method.

The proposed method can only compensate for inter-frame motion. We correct for the motion using registration of the images in the time series, prior to estimation of the parameter maps. An alternative to this approach is the joint estimation of motion and the low-rank dataset as in [68]. The improvement in the results comes from superior reconstruction of the image series, which translates into good quality

parameter maps.

The quality of the reconstructions depends on the regularization parameter λ. We used the L-curve method to optimize λ. We observed that the value of λ did not vary much across different datasets acquired with the same protocol. Therefore, in the practical setting, once the λ is tuned for one dataset, it could be used to recover other datasets that are acquired using the same protocol. In order for the majorize-minimize algorithm to converge, β should tend to infinity, and convergence of the algorithm is slow at higher values of β. Thus the continuation method plays a significant role in providing faster convergence. Currently, the reconstruction time for one slice is about 40 min on the GPU. We observed that the CG steps required to solve the quadratic sub-problems are time consuming. These CG steps can be avoided by additional variable splitting in the data consistency term as shown in [31, 69], which is a subject of further investigation.

The proposed scheme can be extended in several directions. First, in the current setting, we reconstruct the 3D data slice by slice, but the algorithm can be further modified to reconstruct the entire 3D data at once, thus exploiting the redundancies across slices. However, this will be computationally expensive. Second, additional constraints such as total variation penalty on the coefficients and sparsity of the basis functions [70] can be added to further improve the results. Third, spatial patches can be used to construct dictionaries to exploit the redundancies in the spatial domain [71, 72]. Lastly, we use a single exponential model to estimate the parameter maps. However several other models like multi-exponential model [73] which will

accommodate for partial volume effects or a Bloch equation simulation based approach can be used for parameter fitting. Since, these extensions are beyond the scope of this paper, we plan to investigate these in future.

4.5 Conclusion

We introduced a blind compressed sensing framework, which learns an over-complete dictionary and sparse coefficients from under-sampled data, to accelerate MR multi-parameter brain mapping. The proposed scheme yields reasonable parameter estimates at high acceleration factors, thereby considerably reducing scan time. The robustness of the BCS scheme to motion makes it well suited for multi-parameter mapping in a setting with high probability of patient-specific motion or in a dynamic setting like in cardiac applications.

CHAPTER 5
BLIND COMPRESSED SENSING ENABLES 3D DYNAMIC FREE BREATHING MR IMAGING OF LUNG VOLUMES AND DIAPHRAGM MOTION

5.1 Introduction

In this chapter, we study the clinical utility of the BCS scheme to enable free breathing lung MRI with full lung coverage. Dynamic imaging of respiratory mechanics plays an important role in the diagnosis of abnormalities to the active and passive components involved in respiratory pumping, including diaphragm paresis or paralysis, abnormal chest wall mechanics, and muscle weakness, which are a result of neuromuscular, pulmonary, or obesity related disorders [74, 75]. Clinically, these impaired respiratory mechanics are evaluated indirectly by respiratory inductive plethysmography, spirometry or magnetometer [76]. While these schemes can be collected with very high temporal resolution, they lack spatial information and hence can only detect global changes which occur only during the advanced stages of the disease [77]. Early detection and localization of the disease is very crucial for treatment planning.

Magnetic resonance imaging is gaining popularity over the above techniques because it provides a non-invasive and direct visualization of dynamic changes in diaphragm and chest wall [78–81] positions, without exposure to ionizing radiation. The evaluation of dynamic changes in lung volumes and diaphragm movement requires high spatial and temporal resolution, plus high volume coverage to cover the entire

thorax. Achieving entire volume coverage is especially challenging in obese subjects who are at a high risk for impaired diaphragm movement. The respiratory rate during tidal breathing is 12-16 cycles per min (5 sec per cycle), while the normal respiratory excursion of the diaphragmatic dome is about 1.5 cm [82]. The speed of the diaphragm is about 0.3 cm/sec. Thus considering a pixel size of 3 x 3 mm, the diaphragm position changes at a rate of 1 pixel/sec. To avoid motion-blurring, imaging time should be much shorter than 1 sec. While 2D imaging techniques can offer high temporal resolution, it is challenging to merge the information from multiple 2D slices for 3D visualization of the diaphragmatic dome and volume measurements because of the irregular nature of respiratory motion in most subjects.

Research has shown that three dimensional dynamic MRI (3D-DMRI) is a more suitable option to analyze respiratory mechanics [80, 83, 84] and is reported to have higher correlation with spirometry measurements than 2D-DMRI [85]. However, current 3D-DMRI implementations offer limited temporal/spatial resolution and volume coverage. While improved resolution and coverage may be achieved by acquiring 3D volumes at multiple breath-holds, this approach does not provide good estimates of respiratory dynamics or account for the hysteresis effect that the lung exhibits during normal breathing [74, 80, 82]. Furthermore, subjects with chronic obstructive pulmonary disease (COPD) have difficulty holding their breath making motion analysis difficult. Fast imaging techniques were introduced for 3D DMRI [85–87] but current schemes still compromise on either spatial resolution or the temporal resolution. For example, echo-planar imaging (EPI) based sequences provide a temporal resolution of

330ms/frame, but can only achieve low spatial resolution [87] and partial lung coverage. Similarly, 3D fast low-angle shot (FLASH) sequences with Cartesian undersampling, view-sharing, and parallel imaging was used to obtain whole lung coverage [85], at the expense of a poor temporal resolution of 1 second; these schemes can only be used to image the dynamics during slow and controlled breathing conditions, which limits the flexibility of experimental paradigms. More recently, higher spatiotemporal resolution was reported using a 128 channel coil array [88] with a Cartesian 3D-FLASH sequence and auto-calibrated parallel acquisition (GRAPPA) [64]. However, these custom-made 128 channel coils are not widely available which restricts the widespread utility of this scheme.

The main focus of this chapter is to evaluate the feasibility of blind compressed sensing (BCS) scheme, coupled with 3D stack of stars based golden angle radial trajectories, to enable the dynamic imaging of lung volumes and the diaphragm, with full coverage of the thorax, at the spatial and temporal resolution needed to image tidal breathing. We compare the BCS scheme against other state of the art compressed sensing schemes that model the voxel profiles such as nuclear minimization based low rank reconstruction, ℓ_1 Fourier sparsity based regularization [26,89–91] and the commonly used view-sharing reconstruction. We have two expert radiologists quantitatively score the reconstructions from all the schemes on a four-point scale to assess the diagnostic image quality.

5.2 Materials and methods

5.2.1 Image acquisition

The institutional review board at the local institution approved all the in-vivo acquisitions. All the volunteers were fully informed of the nature of the procedure and written consent was obtained. The subjects were scanned on the Siemens 3T Trio scanner (Siemens AG, Healthcare sector, Erlangen, Germany) with a 32-channel body array coil.

Retrospectively undersampled 2D acquisition: A fully sampled 2D dynamic dataset was collected on a normal subject using a gradient recalled echo (GRE) sequence with uniform radial sampling pattern. The sequence parameters were FOV: $350 \times 350\text{mm}^2$, slice thickness: 10mm, TR/TE: 2.67/1.17ms, and matrix size: 128×128. The spatial resolution was $2.7 \times 2.7 \times 10\text{mm}^3$. 180 frames were acquired with 256 radial spokes per frame, which resulted in a temporal resolution of 683ms.

Prospective 3D acquisition: 8 healthy volunteers (5 males and 3 females; median age: 28) without any evidence of pulmonary disease were included in this study. The 3D dynamic data was collected using a FLASH sequence with a 3D radial stack of stars trajectory as shown in Fig. 5.1 The 3D acquisition uses a golden angle radial trajectory in the axial plane (k_x, k_y) combined with a conventional phase encoding step in the k_z direction. The radial spokes were separated by the golden angle (111.25^0) to achieve incoherent sampling. The sequence parameters for 6 of the 8 datasets are: FOV= $350 \times 350\text{mm}^2$, TR/TE= 2.37ms/0.92ms, partial Fourier factor: 6/8, base matrix size: 128×128, and spatial resolution: $2.7 \times 2.7 \times 10\text{mm}^3$. A total of

3500 radial spokes were acquired per slice and a total of 16 slices were acquired to obtain whole lung coverage. The data was binned by considering 16 radial spokes per frame resulting in a temporal resolution of 492.96 ms/frame. The coil sensitivity profiles were estimated using an Eigen decomposition method [35]. The 7th dataset was acquired with a larger FOV: $400 \times 400\text{mm}^2$ that resulted in slightly lower spatial resolution of $3.1 \times 3.1 \times 10\text{mm}^3$. All the other scan parameters were the same as previous acquisitions. Two datasets were collected from the 8th subject, one while free breathing and one while breathing from functional residual capacity (FRC) to total lung capacity (TLC). The scan parameters for these two datasets were FOV= $350 \times 350\text{mm}^2$, TR/TE= 2.37ms/0.92ms, base matrix size: 128×128, spatial resolution: $2.7 \times 2.7 \times 10\text{mm}^3$. A total of 18 slices were acquired with 3500 radial spokes per slice. 16 radial spokes were binned for each frame, which gave a temporal resolution of 683 ms for these two datasets. The scan time for each of these datasets was less than 2 min.

5.2.2 Image reconstruction

In this work, we pre-interpolated the radial data points on a Cartesian grid points that were within 0.5 unit of the measured sample using linear interpolation. A similar pre-interpolation step is used in constrained reconstruction algorithms for other body part applications [19, 28, 89]. The pre-interpolation was done for all the schemes. This enabled us to use fast Fourier transforms (FFTs) and inverse FFTs in the forward and backward models of the algorithm. There was no noticeable change

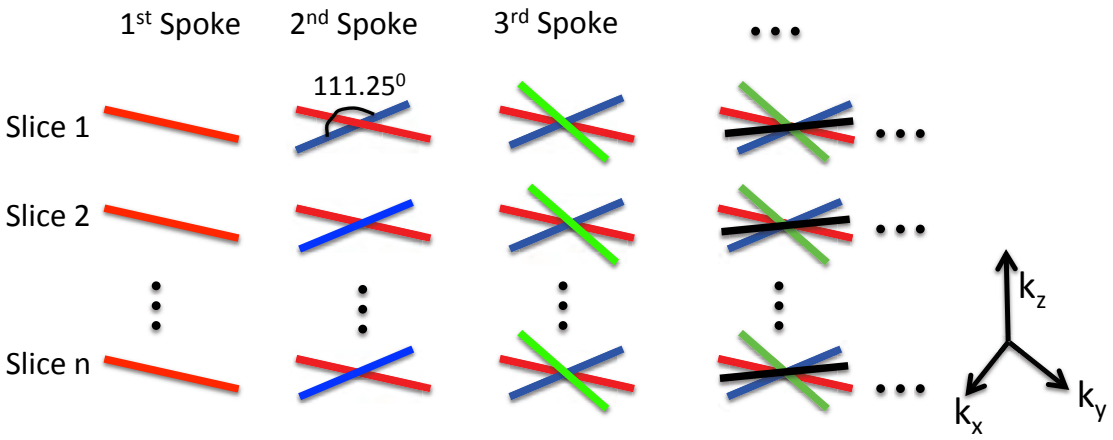

Figure 5.1: 3D golden angle radial stack of stars acquisition 3D golden angle radial stack of stars acquisition: The figure shows the 3D golden angle stack of stars trajectory. The 1st radial spoke is acquired for each slice, then the 2nd spoke is acquired for all slices followed by the third and so on. Each of the spokes are separated by the golden angle of 111.25^0 from the previous one. Note: The sampling pattern is the same for all the slices.

in the quality of reconstructions obtained from pre-interpolated data as compared to the ones obtained from non-Cartesian data with non-uniform data with non-uniform FFTs (NUFFTs) and INUFFTs.

5.2.2.1 Schemes under comparison

The goal of the reconstruction schemes is to recover the dynamic dataset $\mathbf{\Gamma}$ from its undersampled measurements. Here, $\mathbf{\Gamma}$ is an $M \times N$ Casorati matrix, where M is number of voxels in a single time frame and N is number of time frames. In other words, the columns of $\mathbf{\Gamma}$ represent the signal at every voxel. The measurements

are modeled as follows:

$$b_i = \mathcal{A}(\mathbf{\Gamma}) + n_i \quad ; \; i = 1, ..., N \tag{5.1}$$

where b_i is the undersampled measurement and n_i is the noise for the i^{th} time frame. $\mathcal{A}_i = S_i F C$, where S_i is the undersampling mask, F is Fourier operator and C are the coil sensitivities. The least squares reconstruction problem can be posed as:

$$\mathbf{\Gamma}^* = \arg\min_{\mathbf{\Gamma}} \underbrace{\|\mathcal{A}(\mathbf{\Gamma}) - b\|_F^2}_{\text{Data consistency term}} \tag{5.2}$$

The compressed sensing schemes considered in this paper enforce different priors on the temporal profiles of the data to make the problem well posed. We discuss each of the schemes in detail below.

- Low rank recovery using nuclear norm minimization [26, 90, 91]: This scheme assumes that the temporal profiles of pixels lie in a low dimensional space. Fig. 5.2(a) reveals the low rank structure of the data where the singular values rapidly decay to zero. The problem is formulated as a convex optimization problem given below:

$$\mathbf{\Gamma}^* = \arg\min_{\mathbf{\Gamma}} \underbrace{\|\mathcal{A}(\mathbf{\Gamma}) - b\|_F^2}_{\text{Data consistency term}} + \underbrace{\lambda \|\mathbf{\Gamma}\|_*}_{\text{Nuclear norm}} \tag{5.3}$$

  where λ is the regularization parameter. The nuclear norm, which is a convex relaxation of the matrix rank, is defined as $\|\mathbf{\Gamma}\|_* = \sum_{i=1}^{\min M,N} \sigma_i$, where σ_i are

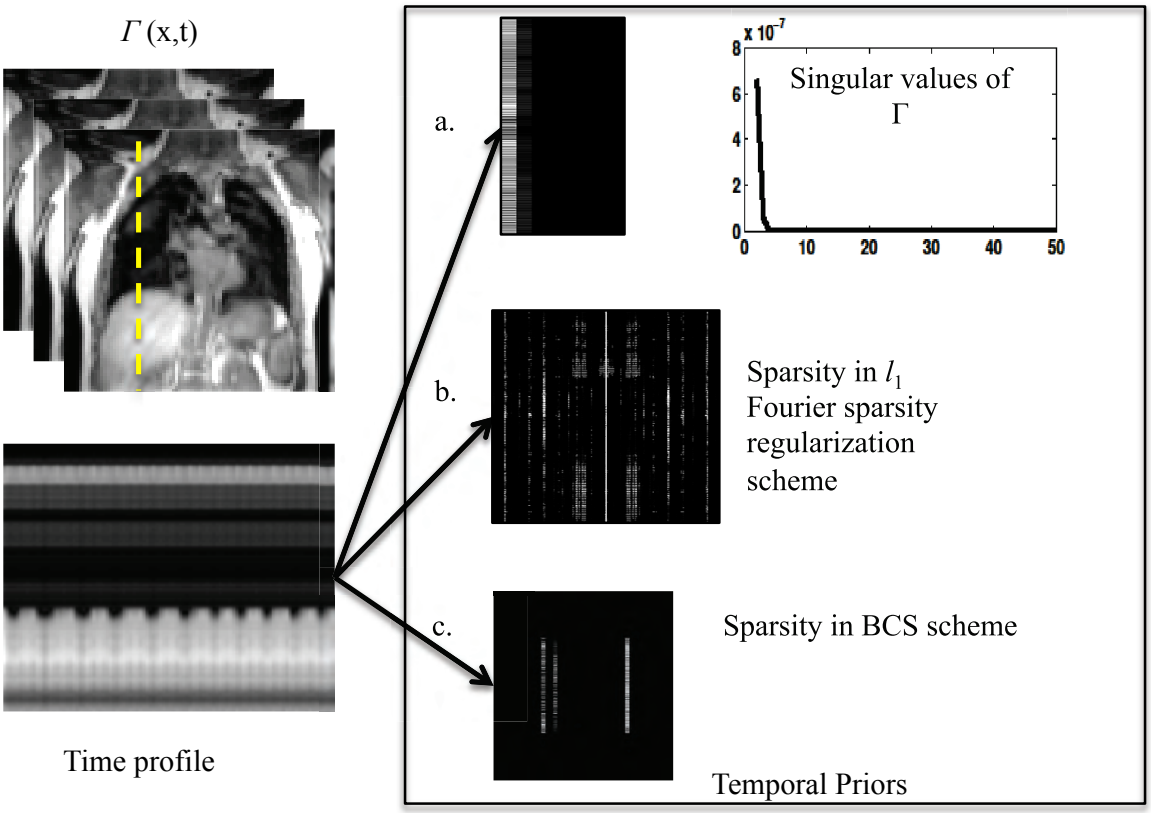

Figure 5.2: Illustration of the data representation in different transform domains Illustration of the data representation in different transform domains: The nuclear norm minimization scheme, the ℓ_1 Fourier sparsity regularization scheme, and the BCS scheme relies on constrained modeling of the intensity profiles of the voxels, specified by $\mathbf{\Gamma} = UV$. The nuclear norm minimization scheme capitalizes on the efficient representation of the voxel profiles using few basis functions. The coefficients in U, along with the singular values are shown in a. The singular values of the data ($\mathbf{\Gamma}$) decay rapidly to zero indicating that the data can be represented efficiently using few basis functions. The pseudo-periodicity of the data is exploited by ℓ_1 Fourier sparsity regularization scheme, using the sparse representation of the intensity profiles in the temporal Fourier transform (x-f space) as seen in b. Figure c shows the sparse coefficients obtained from the BCS scheme. BCS, similar to nuclear norm minimization scheme, learns the dictionary of the basis functions from the data itself, thus adapting to the dynamic content of the time series. The adaptation of the dictionary to the signal provides sparser representations, which in turn translates to improved reconstructions.

the singular values of $\mathbf{\Gamma}$. The nuclear norm minimization scheme can be viewed as a direct alternative to classical two step low rank [10] schemes, which pre-learn the temporal basis functions from navigator data and use these functions to estimate the basis images.

- ℓ_1 Fourier sparsity regularization : This scheme exploits the sparsity of the data in the Fourier transform domain along the temporal dimension (x-f space) (see Fig. 5.2(b)). The convex optimization problem is formulated as:

$$\mathbf{\Gamma}^* = \arg\min_{\mathbf{\Gamma}} \underbrace{\|\mathcal{A}(\mathbf{\Gamma}) - b\|_F^2}_{\text{Data consistency term}} + \underbrace{\lambda\|\mathcal{F}_t(\mathbf{\Gamma})\|_{l_1}}_{\text{temporal Fourier sparsity}} \tag{5.4}$$

where $\mathcal{F}_t$ is the Fourier transform in the temporal direction. The ℓ_1 norm in the second term enforces sparsity on the Fourier coefficients along the temporal dimension. This approach is a widely used scheme and has similarities to k-t SPARSE [21, 92] and k-t FOCUSS [20, 93] schemes, while the specific algorithms used to solve them are different from our implementation. The recovery implicitly assumes that the intensity profiles of the voxels are sparse linear combinations of Fourier exponentials.

- Blind compressed sensing (BCS) [5, 28]: The temporal profile for each pixel is modeled as a sparse linear combination of a atoms from a learned dictionary. Since the dictionary that is learned from the undersampled measurements is subject specific, not necessarily orthogonal and may be over-complete, it provides a richer representation of the data. The sparsity enforced on the dictionary co-

efficients suggests that very few temporal basis functions are sufficient to model the temporal profiles at any pixel. This results in lower degrees of freedom and hence minimizes artifacts at high acceleration factors. The data $\mathbf{\Gamma}$ is modeled as a product of the sparse coefficient matrix U and dictionary V as shown in Fig. 5.3. The signal recovery from undersampled measurements is posed as a constrained optimization algorithm as shown below:

$$[\mathbf{U}^*, \mathbf{V}^*] = \arg\min_{\mathbf{U},\mathbf{V}} \underbrace{\|\mathcal{A}(\mathbf{UV}) - b\|_F^2}_{\text{Data consistency term}} + \underbrace{\lambda\|\mathbf{U}\|_{l_1}}_{\text{Sparsity on spatial weights}} \quad \text{such that } \|\mathbf{V}\|_F^2 < 1 \tag{5.5}$$

The second term is the sparsity promoting ℓ_1 norm on the coefficient matrix U. The optimization problem is constrained by imposing unit Frobenius norm on the over-complete dictionary V, which makes the recovery problem well posed and avoids scale ambiguity issues. Our experiments [28] show that the joint estimation of the basis functions and its coefficients from a golden angle radial trajectory is well-posed, thanks to the oversampling of center of k-space offered by radial trajectories.

- View-sharing: In this scheme, each frame of the dataset is reconstructed by combining information from a few adjacent frames. For this study we combined 200 radial spokes to reconstruct each frame with a step size of 16 to match the temporal resolution with other reconstruction schemes.

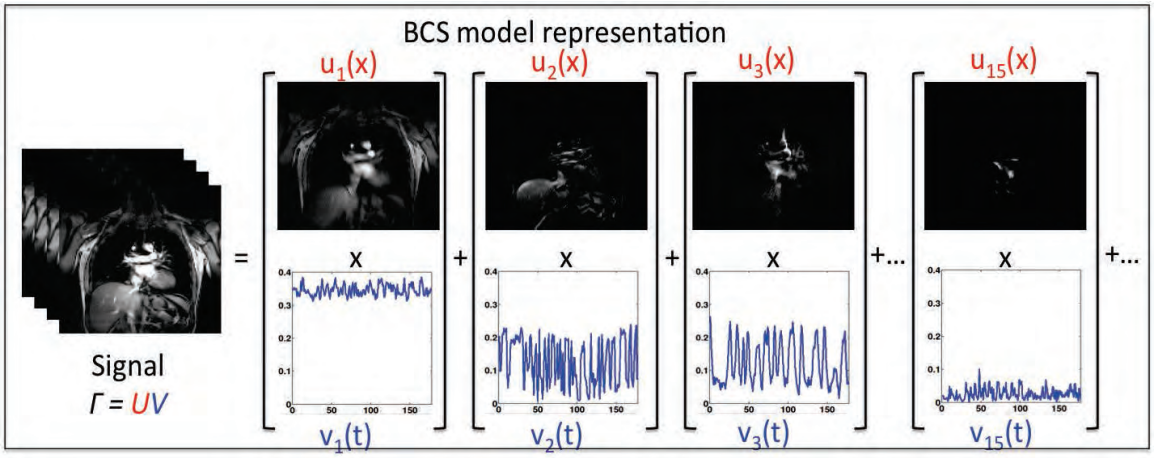

Figure 5.3: BCS model representation BCS model representation: The underlying signal is represented as a sparse linear combination of basis functions from a learnt dictionary $\mathbf{V}$. Here the Casorati matrix Γ is represented as product of spatial coefficients $\mathbf{U}$ and the learnt dictionary $\mathbf{V}$

5.2.2.2 Implementation of constrained algorithms

All the above constrained algorithms are implemented using alternating minimization algorithms; these schemes alternate between (a) a backward mapping from k-space to image space to enforce data consistency, and (b) a projection step, which is a shrinkage or projection operator. These algorithms are guaranteed to converge to the global minimum of the cost function, provided it is convex (nuclear norm and Fourier sparsity regularization, specified by Eq. (5.3) and (5.4), respectively). Due to non-linear nature of the above algorithms, coupled with a non-uniform k-space sampling, it is complex to analyze the spatial and temporal smoothing behavior of the algorithms. However, the projection step provides useful insights on how each of these schemes removes the aliasing patterns that results from the undersampling. We perform a brief analysis of the constrained algorithms to obtain more insights of the

tradeoffs involved in accelerating using these schemes in the appendix A.

The discussion in appendix A shows constrained schemes that model the temporal profiles reduce aliasing artifacts by non-local view-sharing. Specifically, they recover each pixel in the dataset as a weighted linear combination of other pixels in the dataset, possibly distant from it in time. Note that this approach is drastically different from classical view-sharing schemes that combine the data from nearby frames to recover each frame; we term such classical view-sharing schemes as local to differentiate them from the non-local ones discussed above. Non-local averaging combines information from images in similar respiratory phases that are distant in time thus minimizing the temporal blurring introduced by local view-sharing schemes, while achieving good suppression of noise-like aliasing artifacts. The analysis shows that the BCS and ℓ_1 Fourier sparsity regularization schemes perform spatially varying non-local view-sharing, while the nuclear norm minimization scheme performs space invariant non-local view-sharing. The adaptation of the view-sharing strategy with the spatial location enables BCS and ℓ_1 Fourier sparsity regularization to achieve improved denoising performance.

5.2.2.3 Experiment details

The fully sampled dataset (acquired with 256 radial spokes) was retrospectively undersampled using 16 radial spokes per frame, corresponding to an acceleration factor of 8. This retrospectively undersampled dataset was reconstructed with the above mentioned nuclear norm minimization scheme, ℓ_1 Fourier sparsity regu-

larization scheme, BCS, and standard view-sharing scheme. The reconstructed data was compared to the fully sampled acquisition. To study the performance of the BCS scheme as a function of acceleration, the 2D dataset undersampled using 20, 16, 12 and 10 radial spokes corresponding to acceleration factors of 6.4, 8, 10.2 and 12.8, respectively, was reconstructed using the BCS scheme. The slice-by-slice reconstruction was performed for all the 3D DMRI datasets using the above-mentioned schemes. All the reconstructions were performed in MATLAB on a desktop computer (Intel Xeon E5-1620 with 8 core CPUs, 3.6GHz processor and 32 GB RAM) with a 5.6 GB NVDIA graphical processing unit (GPU).

5.2.3 Image quality analysis

To compare reconstructions, we used the following metrics:

- Mean square error (MSE) :

  In the 2D experiments, the fully sampled ground truth data was used as reference to calculate the reconstruction errors. The optimal regularization parameter λ was chosen such that the error between reconstructions and the fully sampled data specified by

$$MSE = \frac{\|\mathbf{\Gamma}_{recon} - \mathbf{\Gamma}_{orig}\|_F^2}{\|\mathbf{\Gamma}_{orig}\|_F^2} \tag{5.6}$$

  was minimized. However, the MSE metric could not be used for the 3D experiments, as the fully sampled ground truth was not available. Hence to optimize

for λ, we used the L-curve strategy [63].

- Normalized high frequency error metric (HFEN):

  The HFEN metric [29] gives a measure of spatial blurring of the image and the quality of fine features and edges. The HFEN metric is defined as:

$$HFEN = \frac{1}{N}\sum_{i=1}^{N}\left(\frac{\|LoG(\mathbf{\Gamma}_{ref,i}) - LoG(\mathbf{\Gamma}_{recon,i})\|_2^2}{\|LoG(\mathbf{\Gamma}_{ref,i})\|_2^2}\right) \tag{5.7}$$

  where N is the number of pixels in the image and LoG is the Laplacian of the Gaussian filter that captures edges. The filter specifications are: kernel size 15×15 pixels, with a standard deviation of 1.5 pixels [29]. The regularization parameters for all the schemes were optimized using the HFEN and MSE values in case of 2D experiments.

- Qualitative evaluation: clinical scoring

  Each of the 3D dynamic reconstructions was evaluated for spatial resolution, temporal resolution and artifacts by two expert cardiothoracic radiologists using a four-point scale (4-Outstanding Diagnostic Quality, 3- Good Diagnostic Quality, 2- Average Diagnostic Quality, 1- Limited Diagnostic Quality and 0- un-interpretable). The image data sets were viewed using OsiriX.

5.2.4 Image post-processing to demonstrate the utility of 3D DMRI

To demonstrate the potential applications, the lung was segmented using a region-growing algorithm implemented in MATLAB after reconstructing the 3D dy-

namic data using the BCS scheme, the nuclear norm minimization scheme and the ℓ_1 Fourier sparsity regularization scheme. This analysis was done for the dataset collected with the tidal breathing maneuver on subject 8. The analysis was repeated for the same subject with deep breathing maneuver using the BCS reconstructed data. The lung volume was calculated in terms of the number of pixels within the lung region. The velocity maps of the diaphragm were obtained using optical flow method [94], which was implemented using a multi-scale approach.

5.3 Results

Dynamic 2D experiments: The performance of all the schemes was first evaluated by retrospectively undersampling a 2D fully sampled dataset. Fig. 5.4 shows a spatial frame from the dynamic 2D dataset (top row), the corresponding error images (middle row), and the time profile at a cross-section shown by the yellow line in spatial frame (last row). The columns correspond to the fully sampled dataset (first column) and the different reconstructions from retrospectively undersampled data. All the comparisons were done at an undersampling factor of 8 (using 16 radial spokes per frame). We observe that the reconstructions from the nuclear norm minimization and ℓ_1 Fourier sparsity regularization schemes suffer from spatio-temporal blurring, especially along the diaphragm borders, as indicated by the arrows in the error images. The local view-sharing scheme combines information from adjacent frames (13 adjacent frames were combined for reconstruction of each frame), which results in significant blurring of the respiratory motion as seen from the time profiles. The BCS

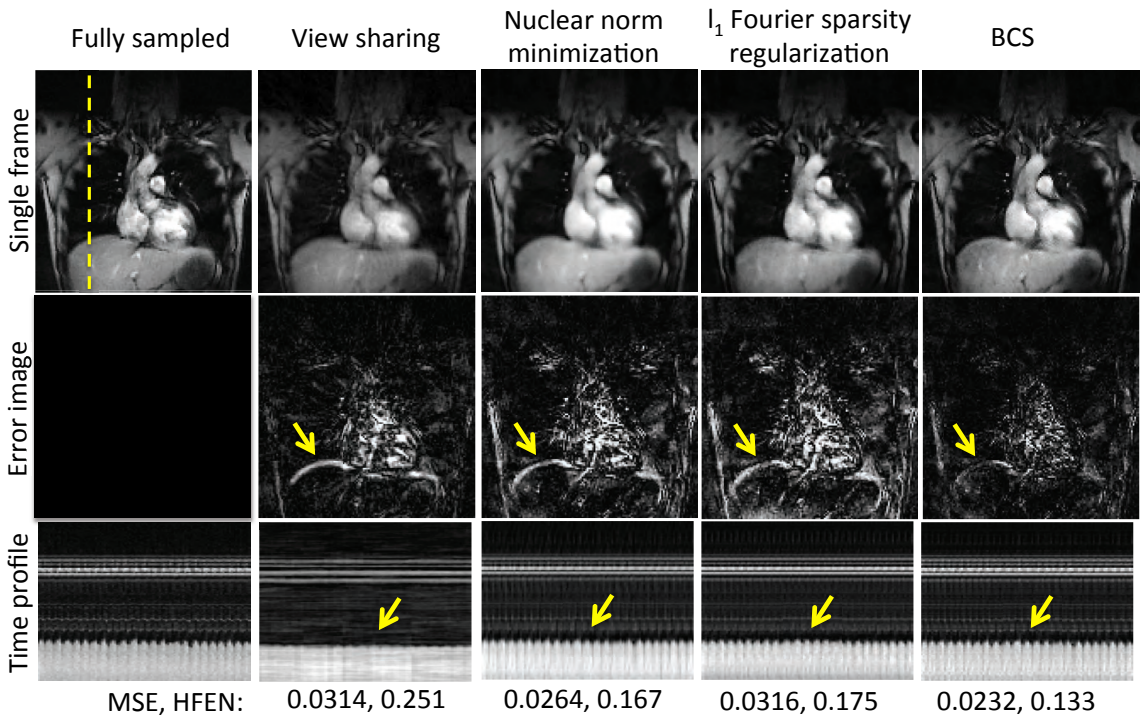

Figure 5.4: Comparison of different schemes on 2D fully sampled dataset Comparison of different schemes on 2D fully sampled dataset: The figure shows comparison of reconstructions obtained from view-sharing, nuclear norm minimization scheme, ℓ_1 Fourier sparsity regularization scheme, and BCS schemes with the fully sampled data. The top row shows a single frame for each of the schemes. The middle row shows the error images with respect to the fully sampled data and the last row shows the time profiles all the schemes at a cross section shown by the yellow dotted line. From the mean square errors (MSE) and the HFEN metric, we observe that BCS gives superior performance than other schemes. All the schemes except BCS suffer from spatio-temporal blurring as shown by the yellow arrows in the error images and time profiles.

scheme has the lowest MSE errors (0.0232) and HFEN values (0.133), which indicates superior reconstruction and less spatio-temporal blurring as compared to the other schemes.

Fig. 5.5 shows the comparisons of the reconstructions from 20, 16, 12 and 10 radial spokes per frame with the fully sampled data. We observe that BCS gives

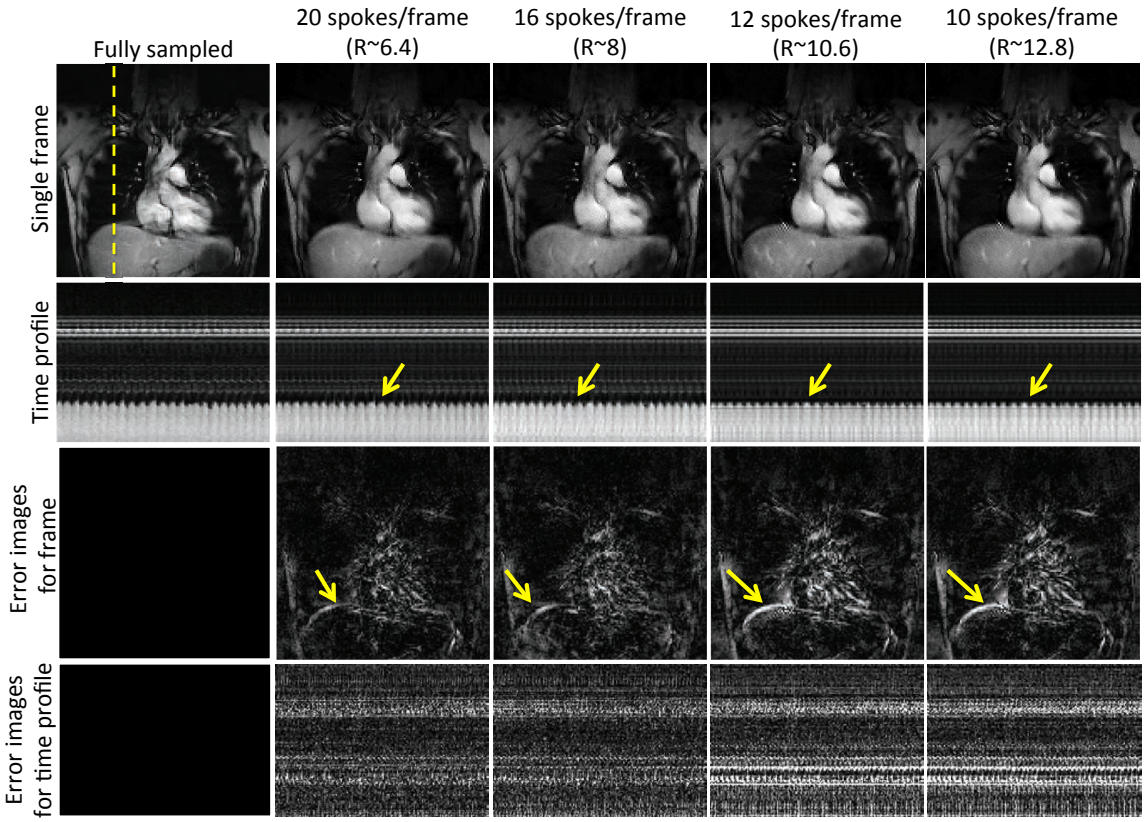

Figure 5.5: Performance of the BCS scheme at different acceleration factors Performance of the BCS scheme at different acceleration factors: The figure shows the single frame (row 1), the time profiles (row 2) and the corresponding error images (row 3-4) of reconstructions obtained by retrospectively undersampling the dataset with 20, 16, 12, and 10 radial spokes per frames resulting in acceleration factors (R) of 6.4, 8, 10.2, and 12.8 respectively. Reliable reconstructions are achieved up to R=8. Beyond R=8 we begin to observe temporal blurring as shown by the arrows in the error images. Note: All the images are in same scale.

reliable reconstructions with 20 and 16 radial spokes per frame. A reconstruction from 12 or 10 radial spokes results in temporal blurring as shown by the arrows. In the 3D experiments, we fixed the number of radial spokes per frame to 16 for all the schemes.

Dynamic 3D experiments: Fig. 5.6 shows the comparisons of the four schemes for two

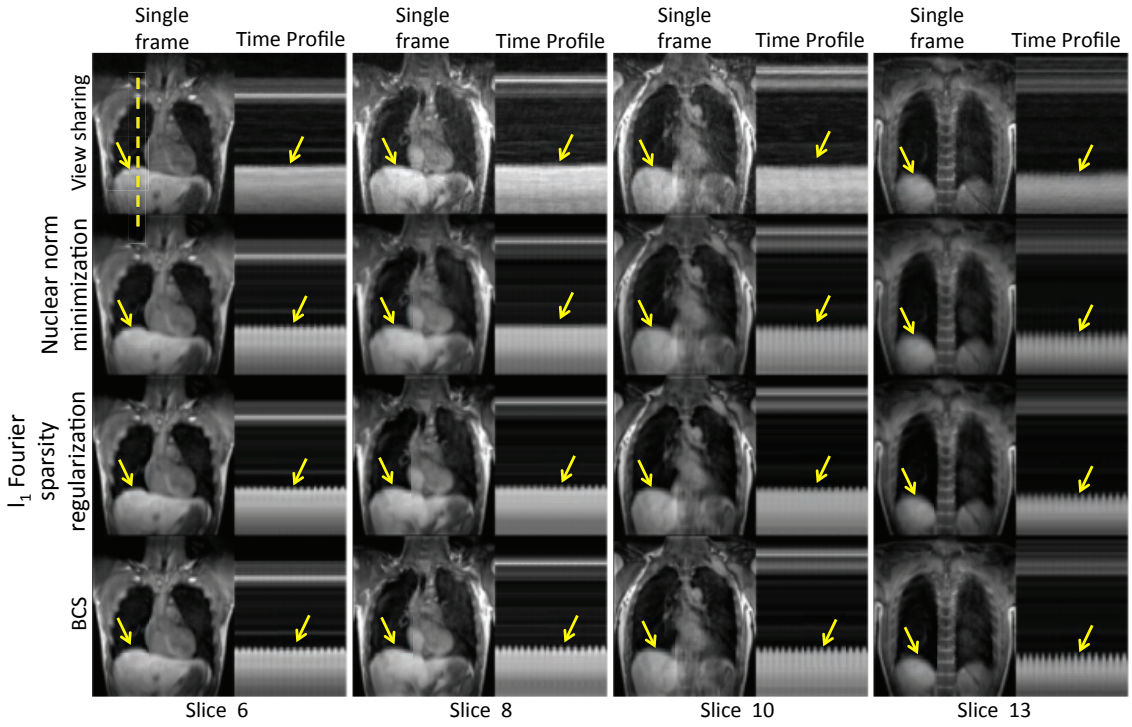

Figure 5.6: Comparison of different schemes on dynamic 3D free breathing Comparison of different schemes on dynamic 3D free breathing: The figure shows comparison between view-sharing, nuclear norm minimization scheme, ℓ_1 Fourier sparsity regularization scheme and BCS scheme (Rows 1-4) for 4 of the 16 slices on subject 2. We observe that the BCS gives better reconstructions than other schemes. It is seen that BCS shows superior spatio-temporal fidelity in comparison to the other schemes (see yellow arrows).

subjects. The figures show a single frame and a time profile along the cross section for 4 of the 16 slices. We observe that the local view-sharing scheme suffers from temporal blurring and aliasing artifacts. The nuclear norm minimization scheme provides better reconstructions than view-sharing, but it exhibits more spatio-temporal blurring than the BCS reconstructions as shown by the arrows. Reconstructions from both the ℓ_1 Fourier sparsity regularization scheme and the BCS scheme show comparable image quality in the spatial domain as seen from the spatial frames in both the figures.

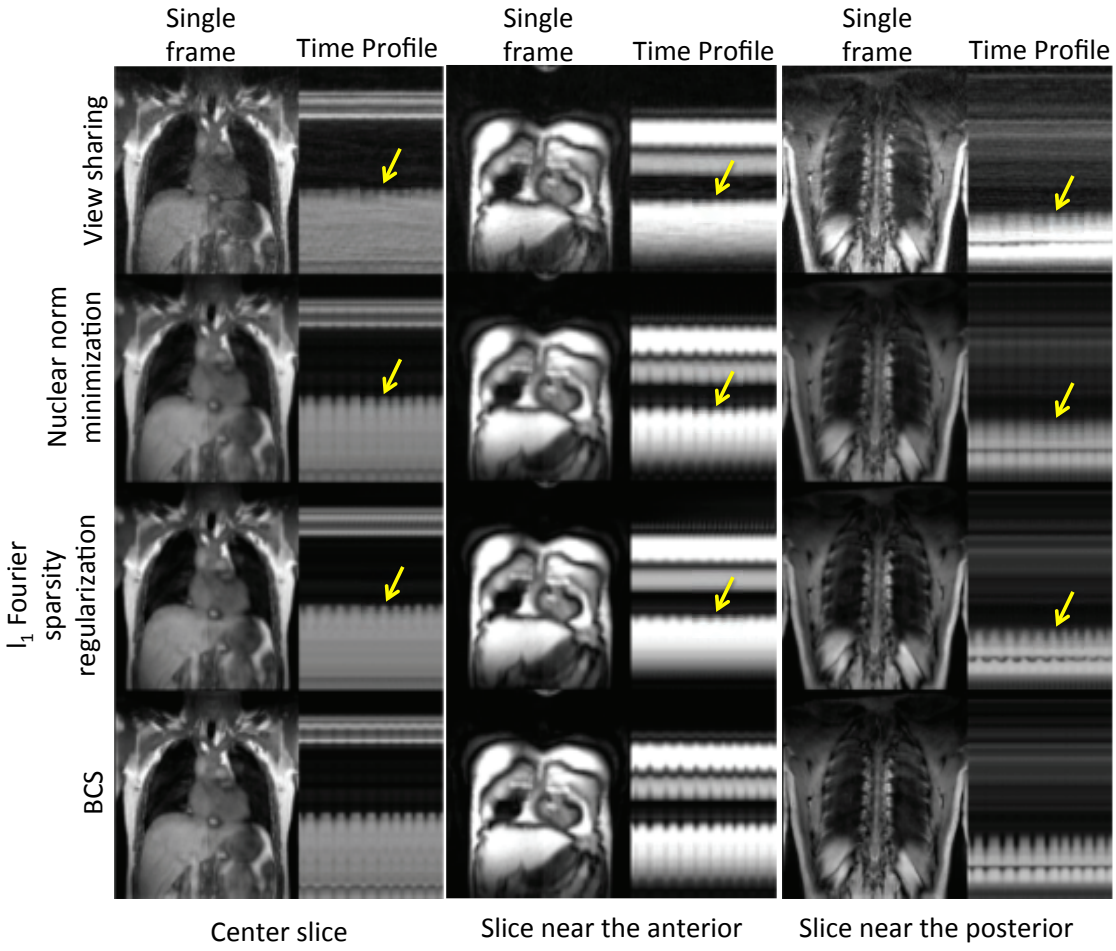

Figure 5.7: Performance of all the schemes as a function of slice position Performance of all the schemes as a function of slice position: The figure shows comparison between view-sharing, nuclear norm minimization scheme, ℓ_1 Fourier sparsity regularization scheme and BCS scheme (Rows 1-4) for slices positioned at the center (1st column), anterior (2nd column), and posterior (3rd column) of the lung. We observe that all schemes except the BCS scheme suffer from higher temporal blurring in the slices at anterior and posterior regions of the lung than those in the center region. BCS scheme is relatively insensitive to the slice position as compared to other schemes.

However, the ℓ_1 Fourier sparsity regularization scheme results in higher temporal blurring than BCS. In slices where the tissue motion is very subtle (slice 6 in Fig. 5.6), BCS preserves the motion whereas all other schemes result in blurring of temporal

details. One of the radiologists carefully analyzed the performance of all the schemes as a function of slice position while clinical scoring as shown in Fig. 5.7 and found that, the performance of the BCS scheme was relatively insensitive to the slice position compared to other schemes. Specifically, the reconstructions of the anterior and posterior slices of the lung (2nd and the 3rd column of Fig. 5.7), obtained by the other schemes, showed higher degradation in image quality than the more central slices (1st column of Fig. 5.7) especially in terms of spatial and temporal blurring (pointed by arrows).

Tables 5.1, 5.2, 5.3 shows the visual scores of all the four schemes by both the radiologists (denoted as R1 and R2) based on three different factors: Aliasing artifacts, Temporal blurring and Spatial blurring respectively. The scores from both the radiologists suggest that the BCS scheme performs better than other schemes in the temporal blurring (Table 5.2) and spatial blurring (Table 5.3) categories. The improved performance of BCS can be attributed to the spatially varying non-local averaging feature and its ability to adapt to the cardiac and respiratory patterns of the specific subject. The qualitative scores for aliasing artifacts are roughly the same for nuclear norm minimization scheme (3.75 ± 0.7, 2.62 ± 1.19) and BCS scheme (and 3.62 ± 0.51, 2.62 ± 0.91); the two figures within parentheses denote the mean scores from R1 and R2, respectively, and the number following $\pm$ is the standard deviation. We observe that the inter-observer variability is high for this category compared to the others. The scores for the view-sharing scheme are much lower than other three schemes for all the three categories from both radiologists.

In summary, the BCS scheme, the nuclear norm minimization scheme and the ℓ_1 Fourier sparsity regularization scheme perform comparably in terms of minimizing the aliasing artifacts.

However, BCS scheme out-performs all other schemes in terms of minimizing spatio-temporal blurring as compared to the other schemes.

Fig. 5.8 shows the lung volume as a function of time and the lung segmentation contours for the BCS, nuclear norm minimization and ℓ_1 Fourier sparsity regularization schemes on one subject with tidal breathing maneuver. The change in lung volume for BCS (approximately 200 mL) was significantly different from that for the nuclear norm minimization scheme (around 150 mL) and ℓ_1 Fourier sparsity regularization scheme (<100 mL). The contours depict the boundary of the lung obtained from the segmentation of the reconstructions. The two time points (a and b) in the figure correspond to maximum inspiratory volume. From the contours, we observe that at maximum inspiration the boundary of the lung for nuclear norm minimization and ℓ1 Fourier sparsity regularization scheme is higher than that for the BCS scheme, which means the volume of the lung is less than that for the BCS scheme. This is attributed to higher temporal blurring in the other two schemes as compared to the BCS scheme. The time point c corresponds to maximum expiration. From the last row in the figure we observe that the segmentations from all the three schemes are the same. The tidal volume analysis could not be performed on the view-sharing scheme since the reconstructions in this case suffered from aliasing artifacts, which resulted in poor segmentation of the lungs.

Table 5.1: Clinical Scores: Aliasing Artifacts Clinical Scores: Aliasing Artifacts

Subjects	BCS		Nuclear norm minimization		$\ell_1 Fourier$ sparsity		View sharing	
	R1	R2	R1	R2	R1	R2	R1	R2
Subject 1	4	1	4	1	3	1	1	1
Subject 2	3	3	4	3	2	3	1	1
Subject 3	4	4	4	4	4	4	1	2
Subject 4	4	3	2	3	3	3	1	2
Subject 5	4	3	4	3	2	3	1	2
Subject 6	4	2	4	2	4	2	1	1
Subject 7	3	3	4	4	3	2	1	1
Subject 8	3	2	4	1	3	1	1	0
Average scores	3.62 ± 0.51	2.62 ± 0.91	3.75 ± 0.7	2.62 ± 1.9	3 ± 0.76	2.37 ± 1.06	1 ± 0	1.25 ± 0.7

Table 5.2: Clinical Scores: Temporal Blurring Clinical Scores: Temporal Blurring

Subjects	BCS		Nuclear norm minimization		$\ell_1 Fourier$ sparsity		View sharing	
	R1	R2	R1	R2	R1	R2	R1	R2
Subject 1	**4**	**4**	2	3	3	3	0	0
Subject 2	**4**	**4**	3	4	3	4	2	1
Subject 3	**4**	**4**	1	3	2	3	1	1
Subject 4	**4**	**4**	2	3	3	3	1	1
Subject 5	**4**	**4**	3	4	2	4	0	1
Subject 6	**4**	**3**	2	2	2	2	1	1
Subject 7	**4**	**4**	1	2	2	2	0	1
Subject 8	**4**	**4**	3	3	2	3	0	0
Average scores	**4 ± 0**	**3.87 ± 0.35**	2.21 ± 0.83	3 ± 0.75	2.37 ± 0.51	2.5 ± 1.3	0.62 ± 0.74	0.75 ± 0.46

Table 5.3: Clinical Scores: Spatial Blurring Clinical Scores: Spatial Blurring

Subjects	BCS		Nuclear norm minimization		$\ell_1 Fourier$ sparsity		View sharing	
	R1	R2	R1	R2	R1	R2	R1	R2
Subject 1	**4**	**4**	2	3	3	3	1	4
Subject 2	**3**	**4**	2	4	3	2	1	3
Subject 3	**4**	**4**	2	4	3	3	1	4
Subject 4	**4**	**4**	2	4	3	3	1	4
Subject 5	**4**	**4**	3	4	3	2	1	4
Subject 6	**4**	**4**	3	4	3	2	1	4
Subject 7	**4**	**4**	2	4	3	3	1	3
Subject 8	**4**	**4**	2	4	3	3	1	3
Average scores	**3.87 ± 0.35**	**4 ± 0**	2.25 ± 0.46	3.87 ± 0.35	3 ± 0	2.63 ± 0.52	1 ± 0	3.62 ± 0.51

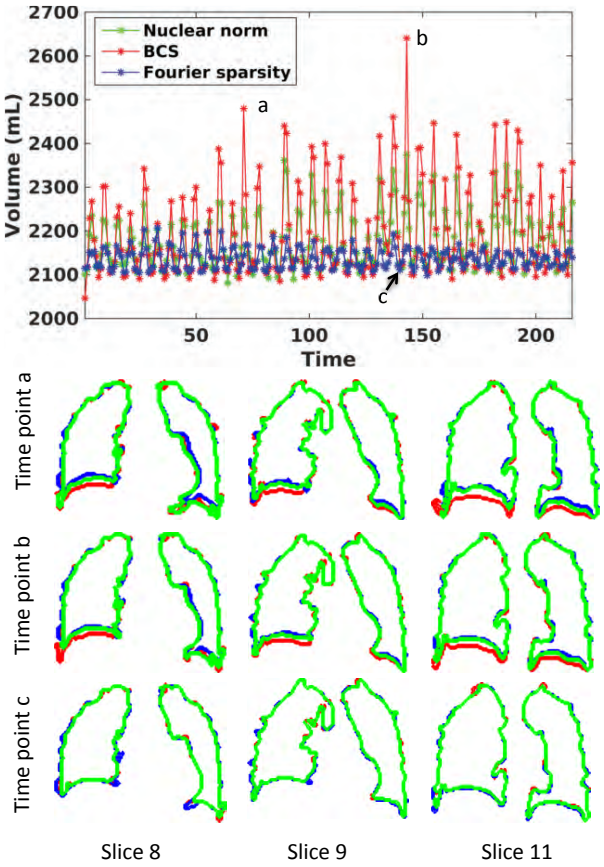

Figure 5.8: Comparison of BCS, Nuclear norm minimization and ℓ_1 Fourier sparsity regularization schemes for changes in lung volume as a function of time for Subject 8 Comparison of BCS, Nuclear norm minimization and ℓ_1 Fourier sparsity regularization schemes for changes in lung volume as a function of time for Subject 8: The plot shows the volume of lung (in mL) as a function of time obtained from reconstructions using BCS (in red), nuclear norm minimization (in green) and ℓ_1 Fourier sparsity regularization (in blue). The second, third and fourth rows show the lung segmentation contours for the three schemes at three time points a. and b. and c. respectively. The contours are shown for three of the 18 slices. From the plot as well as from the segmentations, we can see that the nuclear norm minimization and ℓ_1 Fourier sparsity regularization scheme suffer from considerable temporal blurring. Note: that the segmentations at time point c (peak expiration) are almost the same. This is expected because the position of the diaphragm changes more during inspiration than expiration.

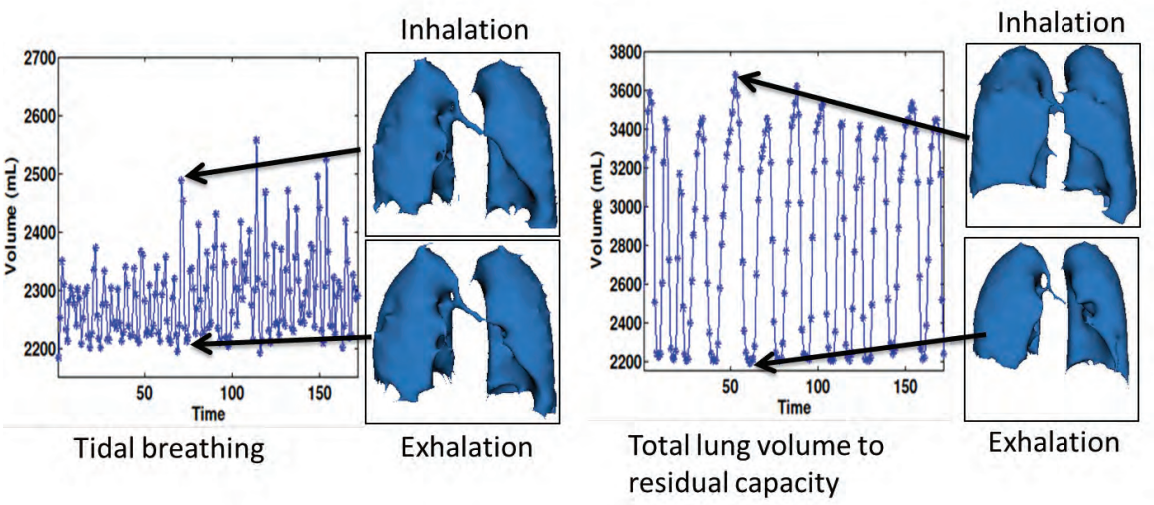

Figure 5.9: Changes in lung volume as function of time Changes in lung volume as function of time: The figure shows the changes in lung volumes as a function of time in case of tidal breathing maneuver (shown on the left) and deep breathing maneuver from total lung capacity (TLC) to functional residual capacity (FRC) (shown on the right). The segmented lung volumes during peak inhalation and peak exhalation are also shown for both breathing maneuvers. The tidal volume was measured to be approximately 200mL and the normal minute ventilation was around 4L/min. The supine inspiratory capacity was measured to be 1.5L. Note that these numbers are for supine position.

Fig. 5.9 shows the change in volume as a function of time and the segmented lung volumes for one subject with tidal breathing and deep breathing maneuvers. The lung was segmented from the reconstructions obtained using the BCS scheme. The change in lung volume was approximately 200mL. The normal minute ventilation was calculated as tidal volume x number of breathing cycles in a minute which was found to be 4L/min. In case of deep breathing maneuver we measured the supine inspiratory capacity, which was found to be 1.5L. This correlates well with the literature for normal subjects in the supine position.

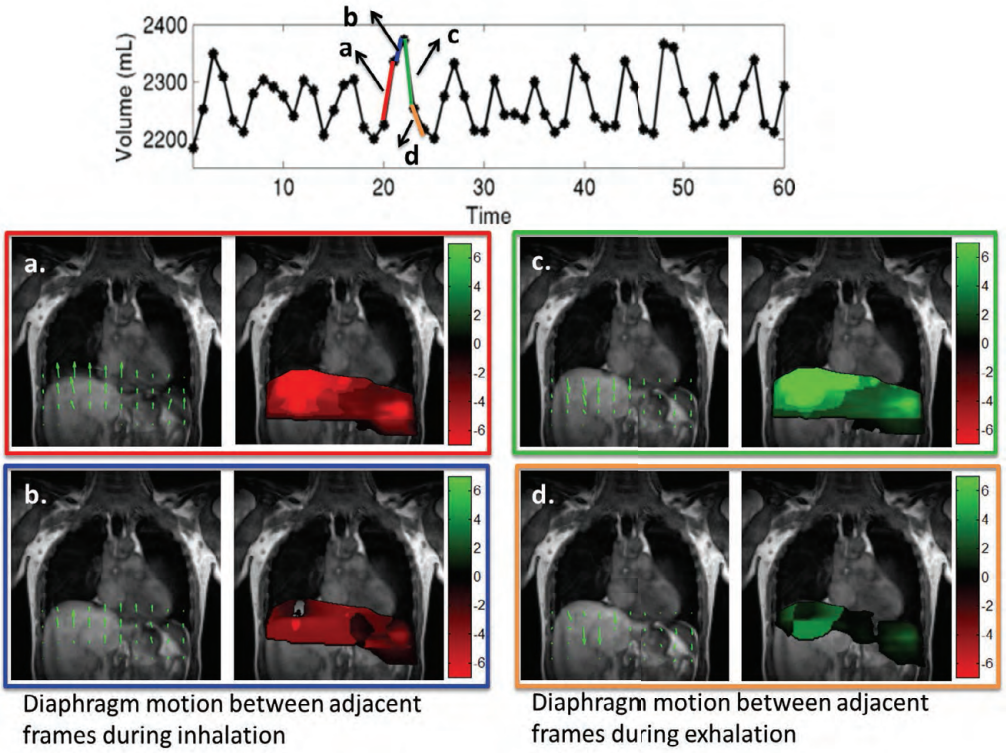

Figure 5.10: Tracking diaphragm motion using velocity maps Tracking diaphragm motion using velocity maps: The motion of the diaphragm was tracked at two time points between inspiration shown in (a-b) and two time points between expiration shown in (c-d). The velocity from inspiration to expiration is considered positive (in green) and velocity from expiration to inspiration is considered negative (in red). The velocity field maps and the color-coded velocity maps are shown for all four cases. The change in lung volume shown by blue segment is much lesser than the change in lung volume shown by red segment. This translates to higher diaphragm motion in frames in red segment as compared to the blue segment as seen from the color coded velocity maps in a and b. Similar results were observed during both inspiration and expiration.

The motion of the diaphragm as tracked using an optical flow method is shown in Fig. 5.10. Two sets of two frames each, one set with a large change in diaphragm position (red segment and blue segment) and one with little change in diaphragm

position (green segment and orange segment) were chosen during inspiration and expiration. The velocity vector maps and the color-coded velocity maps are shown in each of the cases. Fig. 5.10(a-b) shows the velocity maps during inspiration and Fig. 5.10(c-d) shows the velocity maps during expiration. From the color-coded velocity maps we observe that a higher displacement in the diaphragm position (higher diaphragm velocity) correlates well with the observed change in lung volume between the corresponding frames during both inspiration and expiration.

5.4 Discussion

The application of compressed sensing together with parallel imaging to accelerate 3D dynamic imaging of lung volumes and diaphragm motion has not been studied extensively in the past. We evaluated the performance of four different schemes (view-sharing, nuclear norm minimization scheme, ℓ_1 Fourier sparsity regularization scheme and BCS scheme) in accelerating 2D and 3D dynamic free breathing MRI of the thorax in 8 normal subjects. In both our 2D and 3D experiments, we observe that the BCS scheme yields superior reconstructions compared to other schemes qualitatively and quantitatively. The BCS scheme, along with golden angle sampling patterns, offered a temporal resolution of $\approx$ 500ms and a spatial resolution of 2.7 $\times$ 2.7 $\times$ 10mm^3 with whole lung coverage, while maintaining image quality. To the best of our knowledge, this is the first work, which demonstrates temporal resolution of less than 1 sec, along with whole coverage of the thorax, which enables 3D free breathing dynamic imaging of lung volumes and diaphragm motion.

We observe that the classical view-sharing scheme suffers from severe temporal blurring as it combines information from adjacent frames. Since the data acquired is free breathing, the respiratory motion between adjacent frames is very high. Hence, the view-sharing approach results in extensive blurring. In contrast, the constrained schemes can be thought of as non-local view-sharing schemes; their ability to combine information from frames/pixels that are highly similar enables them to reduce blurring. We observe that the ability of the BCS and the ℓ_1 Fourier sparsity regularization scheme to spatially adapt the non-local averaging depending on the dynamics enables them to provide better reconstructions than the nuclear norm minimization scheme. In dynamic datasets with regions corresponding to strikingly different dynamics (e.g. cardiac and respiratory motion), the ability to spatially adapt the non-local averaging can give improved results. The ℓ_1 Fourier sparsity regularization scheme is sensitive to irregular voxel profiles resulting from non-linear interactions between cardiac and respiratory motion. This is because irregular voxel profiles result in a higher number of non-zero Fourier coefficients, thus disrupting the sparsity assumption. The regularity of the breathing patterns will vary from subject to subject leading to inconsistent performance of the ℓ_1 Fourier sparsity regularization scheme. These schemes may not be reliable in the dynamic assessment of lung volumes during free breathing in patients suffering from emphysema or other causes of dyspnea. The patient specific dictionaries in the BCS scheme may be a better choice in patients that are short of breath; these learned basis functions will result in a sparser data representation and hence provide reliable recovery from fewer measurements. Additionally, incoherent

sampling by golden angle ordering aids in obtaining a sparser representation, leading to superior reconstructions. Other interleaved sampling patterns may also lead to similar accelerations however a thorough validation of this claim is beyond the scope of the manuscript. We observe that there are currently several different flavors of compressed sensing implementations, which may be applied to this specific problem. We have used the radial FLASH sequence to demonstrate the feasibility of the BCS scheme. However, this scheme can be combined with more efficient trajectories with longer readouts (e.g. multi-shot EPI, multi-shot spiral) to further improve spatial and temporal resolution and echo-time, which is the focus of this chapter. The acceleration provided by BCS can enable us to keep the readout duration small enough to minimize B0 induced distortions and losses.

The average scores from both the radiologists indicate good agreement for spatial and temporal blurring criteria. There is relatively higher inter-observer variability in scores for the aliasing artifact criterion, but the mean scores from both the radiologists suggest that the BCS scheme performs better. The post-scoring discussion revealed that one of the radiologists gave more importance to the blurring and artifacts that affected the diaphragm motion or diaphragm delineation. By contrast, the other radiologist rated the datasets based on the blurring and artifacts in the whole image rather than placing more emphasis on the diaphragm. This explains the bias in the scores pertaining to spatial blurring. The number of subjects is insufficient to perform statistical analysis for inter-observer agreement.

Our preliminary results using the BCS scheme for dynamic imaging of lung

volumes and diaphragm motion obtained from a single dataset appear promising. The normal minute ventilation in a resting adult in the upright position is about 5L/min to 8L/min [95]. However the normal minute ventilation in the supine position is less than in the upright position [96, 97] and all of our MRI images were obtained in the supine position. The measured minute ventilation of 4L/min is within the normal range for a supine subject. The measurement of minute ventilation is useful in a number of disease mechanisms that produce arterial hypercapnia [95]. The lung volumes were segmented using a simple region growing approach with minimal user interference. There are more sophisticated lung segmentation algorithms including the fuzzy-connectedness algorithm that could be performed to further improve our lung segmentation.

The proposed imaging protocol acquires 3D data with 16 partitions using the stack of stars trajectory; the sampling pattern is the same for all the partitions, which enables slice-by-slice recovery. While the number of slices is sufficient for good depiction of diaphragm and lung volume dynamics in normal subjects, it may not be sufficient for obese subjects. Improved slice coverage may be obtained using fully 3D recovery exploiting the spatial redundancies and using 3D trajectories. The current sequence uses a 3D stack of stars trajectory, where the sampling along the kz direction is uniform. Since the kz direction is fully sampled (except in some cases where partial Fourier recovery is used), we compute a Fourier transform along kz and recover each slice independently. We anticipate that using different angles for different kz planes as well as sampling different kz planes with different sampling density will provide a more

incoherent and appropriate sampling pattern. This strategy may result in improved recovery, but at the cost of higher computational complexity and memory demand, since we cannot decouple the problem to solve for each slice independently. The golden angle-sampling pattern was used to achieve incoherent sampling across time frames; however, other interleaved patterns can be used with BCS to provide these accelerations. Our future work will focus on these and other image reconstruction schemes that are optimized for individual patients suffering from respiratory disorders including COPD, asthma, and cystic fibrosis.

In conclusion, our study indicates that the blind compressed sensing (BCS) scheme gives individualized reconstructions with diagnostically useful image quality and minimal spatio-temporal blurring as compared to other accelerated imaging schemes. We showed 3D dynamic imaging of lung volumes and diaphragm motion with high spatial and temporal resolution is achievable using the BCS scheme.

CHAPTER 6
SUMMARY AND FUTURE WORK

6.1 Summary

Magnetic resonance Imaging (MRI) is a non-invasive, radiation free imaging modality. The ability of MRI to safely provide information about anatomical structure as well as physiological behavior makes it a promising diagnostic tool in several applications. However, MRI is a slow imaging modality. This makes it less applicable in the clinical setting especially in case of multi-dimensional MRI applications such as dynamic imaging of moving organs, dynamic imaging of contrast uptake through organs and characterization of tissue time relaxation properties. This is because the data acquisition is sequential in time and is limited by slow MRI device physics and the hardware of the scanners. Recently, several schemes have been developed to accelerate MRI acquisitions. Parallel MRI acquisition methods have considerably reduced the number of samples acquired. However, these methods give reasonable results for small acceleration factors, typically 3 or 4 fold, and are limited by noise amplification and aliasing artifacts at high acceleration factors. Compressed sensing (CS) in MRI has allowed for the recovery of the underlying image/signal with significantly lesser number of measurements. It assumes the underlying image/signal to be sparse in some transform domain i.e. that the signal has a sparse representation in a set of signals (or 'basis functions) called the dictionary. Current dictionary learning algorithms are non-adaptive i.e. they use a pre-determined dictionary (E.g. Fourier transform)

thus making them less subject specific.

The main hypothesis is that the use of adaptive dictionaries can better sparsify the underlying signal thus reducing the number of samples acquired and improving resolution and volume coverage of multi-dimensional MRI applications. This thesis develops novel dictionary learning based reconstruction framework to accelerate multi-dimensional MRI acquisition and reconstruction in the context of multi-parameter mapping and dynamic lung imaging applications. The main contributions of this thesis include:

- We have developed a multi-coil blind compressed sensing (BCS) scheme with extension to include non-convex penalties. The model represents the signal as a sparse linear combination of basis functions from an over-complete learned dictionary. The dictionary is learnt from the undersampled data itself making it subject specific and adaptive. We developed two different implementations to solve the multi-coil BCS optimization problem. We developed an efficient algorithm (Algorithm 1) which uses the augmented Lagrangian approach to solve for the dictionary and a Majorize minimize approach to solve for the coefficients. This algorithm requires CG solvers. We also developed a faster implementation of the algorithm to further reduced the computation time by using the variable splitting approach. The algorithm also employs efficient continuation strategies to minimize the local minima effects. From the comparisons on 2D fully sampled multi-parameter mapping dataset, we observe that the implementation with variable splitting technique has a speed up factor of up to $\approx$15 fold.

- The multi-coil BCS scheme enabled whole brain multi-parameter mapping of the brain. The parameters under consideration were $T_1\rho$ and T_2. The acceleration factor of 8 reduced the scan time to 20 min with the achieved spatial resolution of 1.7mm^3 isotropic and 12 encoding parameters for each $T_1\rho$ and T_2 imaging. 2D retrospectively undersampled experiments showed the superior performance of the BCS scheme in yielding good parameter maps and robustness of scheme to motion as compared to other schemes. We also demonstrated the advantage of multi-parameter mapping over single parameter mapping.

- We demonstrated the utility of the multi-coil BCS scheme with non- Cartesian sampling to enable 3D dynamic free breathing lung MRI imaging with whole lung coverage. A 3D stack of stars golden angle radial trajectory was used to acquire the lung imaging data. The non-orthogonal dictionary offers a richer representation of the signal and hence has significant improvement over the traditional CS and low rank schemes. The clinical evaluations from two expert cardio-thoracic radiologists, and the mean square error and high frequency error metrics showed that BCS scheme yields superior reconstructions as compared to CS, low rank and view sharing schemes. The estimation of lung volumes from all schemes showed significantly less spatio-temporal blurring in BCS reconstructions as compared to other schemes. The 3D lung function and respiratory mechanics estimates with a temporal resolution of 500ms, spatial resolution of 2.6x2.6mm^2 and whole lung coverage (16-20 slices) were obtained with an acceleration factor of 8.

6.2 Future work

The methods developed in this thesis are targeted towards clinical utility. The method was tested on a limited number of subjects for both the multi-parameter mapping and 3D dynamic lung imaging application. In order to assess the efficiency and reproducibility of the method, the method should be tested on a large cohort of healthy subjects as well as subjects suffering from diseases for both applications.

Extensions of the 3D radial stack of stars sampling to fully 3D radial or spiral sampling scheme or using a variable density stack of stars radial sampling would enable exploitation of redundancies across the slice direction. This would provide a more sparse representation and hence would enable higher acceleration factors. In the current work all the reconstructions were performed slice by slice. The joint recovery of the 3D + time dataset could provide better reconstructions than 2D + time reconstructions.

APPENDIX A
TEMPORAL POINT SPREAD FUNCTION ANALYSIS

A.1 Tradeoffs in image recovery using constrained algorithms

Tradeoffs in image recovery using constrained algorithms The nuclear minimization scheme, the ℓ_1 Fourier sparsity regularization scheme, and the BCS rely on modeling the temporal profiles/columns of the Casorati matrix. The sparsity priors on the coefficients U in BCS and on the Fourier coefficients in the ℓ_1 Fourier sparsity regularization scheme cause many of the coefficients to be zero. Hence these schemes use different basis functions at different pixels. The nuclear norm minimization scheme, in contrast, does not enforce any sparsity prior and hence uses the same basis functions at each pixel. The projection of the intensity profile at the pixel (x,y), denoted by the vector $\widehat{\rho_{(x,y)}}$, is obtained as

$$\widehat{\rho_{(x,y)}} = \mathbf{P}_{x,y}\rho_{x,y} \tag{A.1}$$

where the matrix $\mathbf{P}_{x,y}$ is the specified by

$$\mathbf{P}_{x,y} = \mathbf{V}'_{ac}(\mathbf{V}_{ac}\mathbf{V}'_{ac})^{-1}\mathbf{V}_{ac} \tag{A.2}$$

The rows of the matrix $\mathbf{V}_{ac}$ are the temporal basis functions that are active at the pixel. The above relation shows that the intensity at the i^{th} frame (i^{th} row of $\widehat{\rho_{(x,y)}}$) is obtained as the weighted linear combination of all the entries in $\rho_{x,y}$; the weights

are specified by the i^{th} row of $P_{x,y}$. We term the rows of the $P_{x,y}$ matrix in Eq. (A.2) as the temporal point spread function (TPSF) since it characterizes averaging across time performed by the above constrained schemes to remove aliasing, which is noise-like in case of radial undersampling (see Fig A.1). We observe that each row of the matrix gives the weights for the corresponding time point.

Since we use the ℓ_1 norm, which is a convex relaxation of ℓ_0 sparsity, the recovered coefficients are not exactly sparse, and have many small non-zero coefficients. Similarly, the recovered matrix is not exactly low rank in the nuclear norm setting. For visualization purposes, we truncate the coefficients whose magnitudes are less than 0.1% of the maximum in the Fourier sparsity regularization and BCS settings to generate Fig. A.1 . Similarly, we perform a singular value decomposition of the recovered matrix, followed by a truncation of singular values less than 0.1% of the maximum in the nuclear norm scheme. We stress that this truncation is only used for visualization; the actual algorithms do not use truncation. Fig. A.1 shows the TPSF for one time point corresponding to peak inhalation (specified by solid orange line) obtained from the reconstructed data and the corresponding signal profiles at three pixels. The pixel intensity at a specific pixel and time point in the denoised image is obtained as a weighted linear combination of pixels at all the time points at the same spatial location; the weights are specified by the value of the TPSF. We observe that the TPSF values are higher for frames with similar respiratory phase (marked by dotted orange markers), which implies that these pixels contribute to the summation heavily. We observe that the TPSF is spatially and temporally varying for

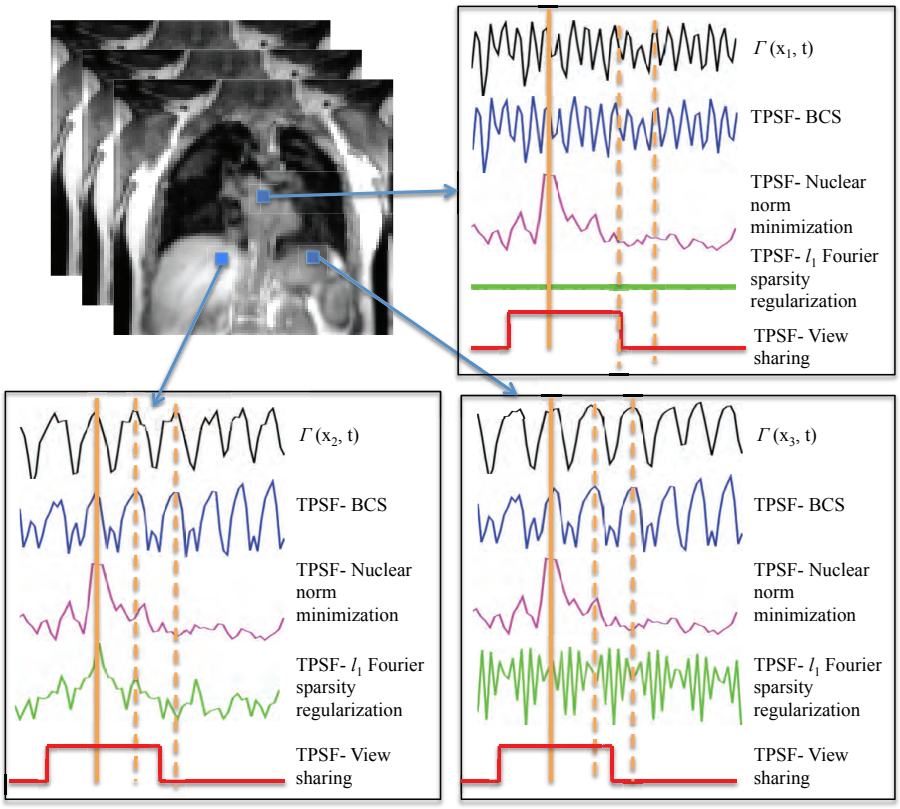

Figure A.1: Illustrations of different algorithms Illustrations of different algorithms: The TPSFs at a specific time frame at peak inhalation (shown by solid orange marker) and the underlying signal time profile are shown for three different pixels. The TPSF plots show that all the three constrained schemes provide non-local averaging of pixel values, thus offering good denoising without resulting in temporal blurring. However the TPSF of view sharing is spatially and temporally invariant and thus leads to significant temporal blurring. The TPSF of BCS and ℓ_1 Fourier sparsity regularization scheme are spatially varying, while the nuclear norm minimization scheme is spatially invariant. We see that the TPSF from BCS is in good correlation with the underlying time profiles (black curves) at the respective pixels. The TPSF for the time frames shown by the solid orange marker has high values corresponding to time frames in the similar respiratory phase (shown by dotted orange marker). These frames contribute predominantly to the recovery of the specific frame, since this recovery is a weighted combination of signal at other time frames and the weights are specified by TPSF.

BCS and ℓ_1 Fourier sparsity regularization scheme. Since the low-rank minimization scheme uses the same set of basis functions at each pixel, in this case the TPSF is

only temporally varying. The TPSF for view sharing method is both temporally and spatially invariant as seen in Fig. A.1.

REFERENCES

[1] C. Ham, J. Engels, V. de Wiel GT, and A. Machielsen, "Peripheral nerve stimulation by induced electric currents: exposure to time-varying magnetic fields," *Journal of Magnetic Resonance Imaging*, vol. 7, no. 5, pp. 933–937, 1997.

[2] J. Reilly, "Peripheral nerve stimulation by induced electric currents: exposure to time-varying magnetic fields," *Medical and Biological Engineering and Computing*, vol. 27, no. 2, pp. 101–110, 1989.

[3] S. Bhave, S. G. Lingala, and M. Jacob, "A variable splitting based algorithm for fast multi-coil blind compressed sensing MRI reconstruction," in *2014 36th Annual International Conference of the IEEE Engineering in Medicine and Biology Society*. IEEE, 2014, pp. 2400–2403.

[4] H.-Y. Heo, S. Bhave, M. Jacob, and J. Zhou, "Blind Compressed Sensing-based Ultrafast Chemical Exchange Saturation Transfer (CEST) Imaging," in *Proceedings of the Annual Meeting of ISMRM, Singapore*, 2016.

[5] S. Bhave, S. G. Lingala, C. P. Johnson, V. A. Magnotta, and M. Jacob, "Accelerated whole-brain multi-parameter mapping using blind compressed sensing," *Magnetic Resonance in Medicine*, 2015.

[6] S. Bhave, S. G. Lingala, J. D. Newell Jr, S. K. Nagle, and M. Jacob, "Whole brain multi-parameter mapping using dictionary learning," in *Proceedings in International Symposium on Magnetic Resonance in Medicine*, 2015.

[7] S. Bhave, S. G. Lingala, J. D. Newell Jr, S. K. Nagle, and M. Jacob, "Blind Compressed Sensing Enables 3-Dimensional Dynamic Free Breathing Magnetic Resonance Imaging of Lung Volumes and Diaphragm Motion," *Investigative radiology*, vol. 51, no. 6, pp. 387–399, 2016.

[8] S. Bhave, S. G. Lingala, A. Comellas, J. D. Newell Jr, and M. Jacob, "Dynamic 3D-MRI of the whole lung using constrained reconstruction with learned dictionaries," in *Proceedings in International Symposium on Magnetic Resonance in Medicine*, 2015.

[9] S. Bhave, S. G. Lingala, J. D. Newell Jr, S. K. Nagle, and M. Jacob, "Clinical Evaluation of Respiratory Mechanics using accelerated dynamic 3D free breathing MRI reconstruction," in *Proceedings in International Symposium on Magnetic Resonance in Medicine*, 2016.

[10] Z.-P. Liang, "Spatiotemporal imaging with partially separable functions," in *IEEE International Symposium on Biomedical Imaging: From Nano to Macro, 2007. ISBI 2007. IEEE*, 2007, pp. 988–991.

[11] Z.-P. Liang, H. Jiang, C. P. Hess, and P. C. Lauterbur, "Dynamic imaging by model estimation," *International journal of imaging systems and technology*, vol. 8, no. 6, pp. 551–557, 1997.

[12] B. Madore, "Using UNFOLD to remove artifacts in parallel imaging and in partial-Fourier imaging," *Magnetic resonance in medicine*, vol. 48, no. 3, pp. 493–501, 2002.

[13] B. Madore, G. H. Glover, N. J. Pelc, *et al.*, "Unaliasing by Fourier-encoding the overlaps using the temporal dimension (UNFOLD), applied to cardiac imaging and fMRI," *Magnetic Resonance in Medicine*, vol. 42, no. 5, pp. 813–828, 1999.

[14] J. Tsao, P. Boesiger, and K. P. Pruessmann, "k-t BLAST and k-t SENSE: Dynamic MRI with high frame rate exploiting spatiotemporal correlations," *Magnetic Resonance in Medicine*, vol. 50, no. 5, pp. 1031–1042, 2003.

[15] M. Doneva, P. Börnert, H. Eggers, C. Stehning, J. Sénégas, and A. Mertins, "Compressed sensing reconstruction for magnetic resonance parameter mapping," *Magnetic Resonance in Medicine*, vol. 64, no. 4, pp. 1114–1120, 2010.

[16] M. Lustig, D. Donoho, and J. M. Pauly, "Sparse MRI: The application of compressed sensing for rapid MR imaging," *Magnetic resonance in medicine*, vol. 58, no. 6, pp. 1182–1195, 2007.

[17] C. Vonesch and M. Unser, "A fast multilevel algorithm for wavelet-regularized image restoration," *IEEE Transactions on Image Processing*, vol. 18, no. 3, pp. 509–523, 2009.

[18] A. Chambolle and P.-L. Lions, "Image recovery via total variation minimization and related problems," *Numerische Mathematik*, vol. 76, no. 2, pp. 167–188, 1997.

[19] G. Adluru, C. McGann, P. Speier, E. G. Kholmovski, A. Shaaban, and E. V. DiBella, "Acquisition and reconstruction of undersampled radial data for myocardial perfusion magnetic resonance imaging," *Journal of Magnetic Resonance Imaging*, vol. 29, no. 2, pp. 466–473, 2009.

[20] H. Jung, K. Sung, K. S. Nayak, E. Y. Kim, and J. C. Ye, "k-t FOCUSS: A general compressed sensing framework for high resolution dynamic MRI," *Magnetic Resonance in Medicine*, vol. 61, no. 1, pp. 103–116, 2009.

[21] R. Otazo, D. Kim, L. Axel, and D. K. Sodickson, "Combination of compressed sensing and parallel imaging for highly accelerated first-pass cardiac perfusion MRI," *Magnetic Resonance in Medicine*, vol. 64, no. 3, pp. 767–776, 2010.

[22] H. Pedersen, S. Kozerke, S. Ringgaard, K. Nehrke, and W. Y. Kim, "k-t PCA: Temporally constrained k-t BLAST reconstruction using principal component analysis," *Magnetic resonance in medicine*, vol. 62, no. 3, pp. 706–716, 2009.

[23] F. H. Petzschner, I. P. Ponce, M. Blaimer, P. M. Jakob, and F. A. Breuer, "Fast MR parameter mapping using k-t principal component analysis," *Magnetic Resonance in Medicine*, vol. 66, no. 3, pp. 706–716, 2011.

[24] B. Recht, M. Fazel, and P. A. Parrilo, "Guaranteed minimum-rank solutions of linear matrix equations via nuclear norm minimization," *SIAM review*, vol. 52, no. 3, pp. 471–501, 2010.

[25] J. P. Haldar and D. Hernando, "Rank-constrained solutions to linear matrix equations using power factorization," *IEEE Signal Processing Letters*, vol. 16, no. 7, pp. 584–587, 2009.

[26] S. G. Lingala, Y. Hu, E. DiBella, and M. Jacob, "Accelerated dynamic MRI exploiting sparsity and low-rank structure: k-t SLR," *IEEE Transactions on Medical Imaging,*, vol. 30, no. 5, pp. 1042–1054, 2011.

[27] R. Otazo, E. Candes, and D. K. Sodickson, "Low-rank plus sparse matrix decomposition for accelerated dynamic MRI with separation of background and dynamic components," *Magnetic Resonance in Medicine*, vol. 73, no. 3, pp. 1125–1136, 2015.

[28] S. Lingala and M. Jacob, "Blind compressive sensing dynamic MRI," *IEEE Transactions on Medical Imaging*, vol. 32, no. 6, p. 1132, 2013.

[29] S. Ravishankar and Y. Bresler, "MR image reconstruction from highly undersampled k-space data by dictionary learning," *IEEE Transactions on Medical Imaging*, vol. 30, no. 5, pp. 1028–1041, 2011.

[30] S. G. Lingala, Y. Mohsin, J. D. Newell, J. C. Sieren, D. Thedens, P. Kollasch, and M. Jacob, "Accelerating dynamic imaging of the lung using blind compressed sensing," *Journal of Cardiovascular Magnetic Resonance*, vol. 16, no. Suppl 1, p. W27, 2014.

[31] S. Ramani and J. A. Fessler, "Parallel MR image reconstruction using augmented Lagrangian methods," *IEEE Transactions on Medical imaging*, vol. 30, no. 3, pp. 694–706, 2011.

[32] D. P. Bertsekas, "Multiplier Methods: a survey," *Automatica*, vol. 12, no. 2, pp. 133–145, 1976.

[33] S. R. Charagundla, A. Borthakur, J. S. Leigh, and R. Reddy, "Artifacts in T1ρ-weighted imaging: correction with a self-compensating spin-locking pulse," *Journal of Magnetic Resonance Imaging*, vol. 162, no. 1, pp. 113–121, 2003.

[34] J. H. Brittain, B. S. Hu, G. A. Wright, C. H. Meyer, A. Macovski, and D. G. Nishimura, "Coronary angiography with magnetization-prepared T2 contrast," *Magnetic Resonance in Medicine*, vol. 33, no. 5, pp. 689–696, 1995.

[35] D. O. Walsh, A. F. Gmitro, and M. W. Marcellin, "Adaptive reconstruction of phased array MR imagery," *Magnetic Resonance in Medicine*, vol. 43, no. 5, pp. 682–690, 2000.

[36] D. Ma, V. Gulani, N. Seiberlich, K. Liu, J. L. Sunshine, J. L. Duerk, and M. A. Griswold, "Magnetic resonance fingerprinting," *Nature*, vol. 495, no. 7440, pp. 187–192, 2013.

[37] M. Haris, A. Singh, K. Cai, C. Davatzikos, J. Q. Trojanowski, E. R. Melhem, C. M. Clark, and A. Borthakur, "T1rho (T1ρ) MR imaging in Alzheimer's disease and Parkinson's disease with and without dementia," *Journal of Neurology*, vol. 258, no. 3, pp. 380–385, 2011.

[38] I. Nestrasil, S. Michaeli, T. Liimatainen, C. Rydeen, C. Kotz, J. Nixon, T. Hanson, and P. J. Tuite, "T1ρ and T2ρ MRI in the evaluation of Parkinson's disease," *Journal of Neurology*, vol. 257, no. 6, pp. 964–968, 2010.

[39] S. Michaeli, D. J. Sorce, M. Garwood, K. Ugurbil, S. Majestic, and P. Tuite, "Assessment of brain iron and neuronal integrity in patients with Parkinson's disease using novel MRI contrasts," *Movement disorders*, vol. 22, no. 3, pp. 334–340, 2007.

[40] A. Borthakur, M. Sochor, C. Davatzikos, J. Q. Trojanowski, and C. M. Clark, "T1rho MRI of Alzheimer's disease," *Neuroimage*, vol. 41, no. 4, pp. 1199–1205, 2008.

[41] F. Zipp, "A new window in multiple sclerosis pathology: non-conventional quantitative magnetic resonance imaging outcomes," *Journal of Neurological Sciences*, vol. 287, pp. S24–S29, 2009.

[42] S. C. Deoni, "Quantitative Relaxometry of the Brain," *Top Magnetic Resonance Imaging*, vol. 21, no. 2, p. 101, 2010.

[43] A. L. Alexander, S. A. Hurley, A. A. Samsonov, N. Adluru, A. P. Hosseinbor, P. Mossahebi, D. P. Tromp, E. Zakszewski, and A. S. Field, "Characterization of cerebral white matter properties using quantitative magnetic resonance imaging stains," *Brain Connect*, vol. 1, no. 6, pp. 423–446, 2011.

[44] K. T. Jokivarsi, Y. Hiltunen, H. Gröhn, P. Tuunanen, O. H. Gröhn, and R. A. Kauppinen, "Estimation of the onset time of cerebral ischemia using T1ρ and T2 MRI in rats," *Stroke*, vol. 41, no. 10, pp. 2335–2340, 2010.

[45] M. Deng, F. Zhao, J. Yuan, A. Ahuja, and Y. J. Wang, "Liver T1ρ MRI measurement in healthy human subjects at 3 T: a preliminary study with a two-dimensional fast-field echo sequence," *Liver*, vol. 85, no. 1017, 2012.

[46] Y.-X. J. Wang, F. Zhao, J. F. Griffith, G. S. Mok, J. C. Leung, A. T. Ahuja, and J. Yuan, "T1rho and T2 relaxation times for lumbar disc degeneration: an in vivo comparative study at 3.0-Tesla MRI," *European Radiology*, vol. 23, no. 1, pp. 228–234, 2013.

[47] X. Li, D. Kuo, A. Theologis, J. Carballido-Gamio, C. Stehling, T. M. Link, C. B. Ma, and S. Majumdar, "Cartilage in Anterior Cruciate Ligament–Reconstructed Knees: MR Imaging T1ρ and T2—Initial Experience with 1-year Follow-up," *Radiology*, vol. 258, no. 2, p. 505, 2011.

[48] X. Li, A. Pai, G. Blumenkrantz, J. Carballido-Gamio, T. Link, B. Ma, M. Ries, and S. Majumdar, "Spatial distribution and relationship of T1ρ and T2 relaxation times in knee cartilage with osteoarthritis," *Magnetic Resonance in Medicine*, vol. 61, no. 6, pp. 1310–1318, 2009.

[49] P. M. Robson, A. K. Grant, A. J. Madhuranthakam, R. Lattanzi, D. K. Sodickson, and C. A. McKenzie, "Comprehensive quantification of signal-to-noise ratio and g-factor for image-based and k-space-based parallel imaging reconstructions," *Magnetic Resonance in Medicine*, vol. 60, no. 4, pp. 895–907, 2008.

[50] C. Huang, C. G. Graff, E. W. Clarkson, A. Bilgin, and M. I. Altbach, "T2 mapping from highly undersampled data by reconstruction of principal component coefficient maps using compressed sensing," *Magnetic Resonance in Medicine*, vol. 67, no. 5, pp. 1355–1366, 2012.

[51] J. P. Haldar and Z.-P. Liang, "Spatiotemporal imaging with partially separable functions: a matrix recovery approach," in *IEEE International Symposium on Biomedical Imaging: From Nano to Macro, 2010. ISBI 2010, IEEE*, 2010, pp. 716–719.

[52] J. V. Velikina, A. L. Alexander, and A. Samsonov, "Accelerating MR parameter mapping using sparsity-promoting regularization in parametric dimension," *Magnetic Resonance in Medicine*, vol. 70, no. 5, pp. 1263–1273, 2013.

[53] L. Feng, R. Otazo, H. Jung, J. H. Jensen, J. C. Ye, D. K. Sodickson, and D. Kim, "Accelerated cardiac T2 mapping using breath-hold multi-echo fast spin-echo pulse sequence with k-t FOCUSS," *Magnetic Resonance in Medicine*, vol. 65, no. 6, pp. 1661–1669, 2011.

[54] B. Zhao, F. Lam, and Z. Liang, "Model-based MR parameter mapping with sparsity constraints: Parameter estimation and performance bounds," *IEEE Transactions on Medical Imaging*, 2014.

[55] W. Li, M. Griswold, and X. Yu, "Fast cardiac T1 mapping in mice using a model-based compressed sensing method," *Magnetic Resonance in Medicine*, vol. 68, no. 4, pp. 1127–1134, 2012.

[56] B. Zhao, J. P. Haldar, C. Brinegar, and Z.-P. Liang, "Low rank matrix recovery for real-time cardiac MRI," in *IEEE International Symposium on Biomedical Imaging: From Nano to Macro, 2010.* IEEE, 2010, pp. 996–999.

[57] S. Gleichman and Y. C. Eldar, "Blind compressed sensing," *IEEE Transactions on Information Theory,*, vol. 57, no. 10, pp. 6958–6975, 2011.

[58] B. Zhao, W. Lu, and Z. Liang, "Highly accelerated parameter mapping with joint partial separability and sparsity constraints," in *Proceedings in International Symposium on Magnetic Resonance in Medicine*, vol. 2233, 2012.

[59] X. Li, E. T. Han, R. F. Busse, and S. Majumdar, "In vivo T1ρ mapping in cartilage using 3D magnetization-prepared angle-modulated partitioned k-space spoiled gradient echo snapshots (3D MAPSS)," *Magnetic Resonance in Medicine*, vol. 59, no. 2, pp. 298–307, 2008.

[60] U. Gamper, P. Boesiger, and S. Kozerke, "Compressed sensing in dynamic MRI," *Magnetic Resonance in Medicine*, vol. 59, no. 2, pp. 365–373, 2008.

[61] S. Vasanawala, M. Murphy, M. T. Alley, P. Lai, K. Keutzer, J. M. Pauly, and M. Lustig, "Practical parallel imaging compressed sensing MRI: Summary of two years of experience in accelerating body MRI of pediatric patients," in *IEEE International Symposium on Biomedical Imaging: From Nano to Macro, 2011.* IEEE, 2011, pp. 1039–1043.

[62] M. Aharon, M. Elad, and A. Bruckstein, "k-SVD: An algorithm for designing over-complete dictionaries for sparse representation," *IEEE Transactions in Signal Processing*, vol. 54, no. 11, pp. 4311–4322, 2006.

[63] P. C. Hansen and D. P. O'Leary, "The use of the L-curve in the regularization of discrete ill-posed problems," *SIAM Journal of Scientific Computing*, vol. 14, no. 6, pp. 1487–1503, 1993.

[64] M. A. Griswold, P. M. Jakob, R. M. Heidemann, M. Nittka, V. Jellus, J. Wang, B. Kiefer, and A. Haase, "Generalized autocalibrating partially parallel acquisitions (GRAPPA)," *Magnetic Resonance in Medicine*, vol. 47, no. 6, pp. 1202–1210, 2002.

[65] M. Lustig and J. M. Pauly, "SPIRiT: Iterative self-consistent parallel imaging reconstruction from arbitrary k-space," *Magnetic Resonance in Medicine*, vol. 64, no. 2, pp. 457–471, 2010.

[66] J. V. Velikina and A. A. Samsonov, "Reconstruction of dynamic image series from undersampled MRI data using data-driven model consistency condition (MOCCO)," *Magnetic Resonance in Medicine*, 2014.

[67] Y. Zhu, Q. Zhang, Q. Liu, Y.-X. J. Wang, X. Liu, H. Zheng, D. Liang, and J. Yuan, "PANDA-T1ρ: Integrating principal component analysis and dictionary learning for fast T1ρ mapping," *Magnetic Resonance in Medicine*, 2014.

[68] S. G. Lingala, E. DiBella, and M. Jacob, "Deformation corrected compressed sensing (DC-CS): a novel framework for accelerated dynamic MRI," *IEEE Transactions on Medical Imaging*, vol. 34, no. 1, pp. 72–85, January 2015.

[69] S. Ravishankar and Y. Bresler, "MR image reconstruction from highly undersampled k-space data by dictionary learning," *IEEE Transactions on Medical Imaging*, vol. 30, no. 5, pp. 1028–1041, 2011.

[70] S. G. Lingala and M. Jacob, "Blind compressed sensing with sparse dictionaries for accelerated dynamic MRI," in *IEEE 10th International Symposium on Biomedical Imaging (ISBI), 2013*, 2013, pp. 5–8.

[71] Y. Wang, Y. Zhou, and L. Ying, "Undersampled dynamic magnetic resonance imaging using patch-based spatiotemporal dictionaries," in *10th International Symposium on Biomedical Imaging, ISBI 2013 IEEE*, 2013, pp. 294–297.

[72] M. Protter and M. Elad, "Image sequence denoising via sparse and redundant representations," *IEEE Transactions on Medical Imaging*, vol. 18, no. 1, pp. 27–35, 2009.

[73] R. M. Kroeker and R. Mark Henkelman, "Analysis of biological NMR relaxation data with continuous distributions of relaxation times," *Journal of Magnetic Resonance Imaging*, vol. 69, no. 2, pp. 218–235, 1986.

[74] D. S. Gierada, J. J. Curtin, S. J. Erickson, R. W. Prost, J. A. Strandt, and L. R. Goodman, "Diaphragmatic motion: fast gradient-recalled-echo MR imaging in healthy subjects," *Radiology*, vol. 194, no. 3, pp. 879–884, 1995.

[75] S. Craighero, E. Promayon, P. Baconnier, J.-F. Lebas, and M. Coulomb, "Dynamic echo-planar MR imaging of the diaphragm for a 3D dynamic analysis," *European radiology*, vol. 15, no. 4, pp. 742–748, 2005.

[76] M. I. Polkey, D. Kyroussis, C.-H. Hamnegard, G. H. Mills, M. Green, and J. Moxham, "Diaphragm strength in chronic obstructive pulmonary disease," *American journal of respiratory and critical care medicine*, vol. 154, no. 5, pp. 1310–1317, 1996.

[77] W. Gold and H. Boushey, "Pulmonary function testing," *Textbook of respiratory medicine*, vol. 1, pp. 798–900, 2000.

[78] A. P. Gauthier, S. Verbanck, M. Estenne, C. Segebarth, P. T. Macklem, and M. Paiva, "Three-dimensional reconstruction of the in vivo human diaphragm shape at different lung volumes," *Journal of Applied Physiology*, vol. 76, no. 2, pp. 495–506, 1994.

[79] T. Kondo, I. Kobayashi, Y. Taguchi, Y. Ohta, and N. Yanagimachi, "A dynamic analysis of chest wall motions with MRI in healthy young subjects," *Respirology*, vol. 5, no. 1, pp. 19–25, 2000.

[80] P. Cluzel, T. Similowski, C. Chartrand-Lefebvre, M. Zelter, J.-P. Derenne, and P. A. Grenier, "Diaphragm and Chest Wall: Assessment of the Inspiratory Pump with MR Imaging—Preliminary Observations 1," *Radiology*, vol. 215, no. 2, pp. 574–583, 2000.

[81] S. Kiryu, S. H. Loring, Y. Mori, N. M. Rofsky, H. Hatabu, and M. Takahashi, "Quantitative analysis of the velocity and synchronicity of diaphragmatic motion: dynamic MRI in different postures," *Magnetic resonance imaging*, vol. 24, no. 10, pp. 1325–1332, 2006.

[82] H.-U. Kauczor, "MRI of the Lung," 2009.

[83] C. Plathow, S. Ley, C. Fink, M. Puderbach, M. Heilmann, I. Zuna, and H.-U. Kauczor, "Evaluation of chest motion and volumetry during the breathing cycle by dynamic MRI in healthy subjects: comparison with pulmonary function tests," *Investigative radiology*, vol. 39, no. 4, pp. 202–209, 2004.

[84] C. Plathow, S. Ley, C. Fink, M. Puderbach, W. Hosch, A. Schmähl, J. Debus, and H.-U. Kauczor, "Analysis of intrathoracic tumor mobility during whole breathing cycle by dynamic MRI," *International Journal of Radiation Oncology* Biology* Physics*, vol. 59, no. 4, pp. 952–959, 2004.

[85] C. Plathow, M. Schoebinger, C. Fink, S. Ley, M. Puderbach, M. Eichinger, M. Bock, H.-P. Meinzer, and H.-U. Kauczor, "Evaluation of lung volumetry using dynamic three-dimensional magnetic resonance imaging," *Investigative radiology*, vol. 40, no. 3, pp. 173–179, 2005.

[86] C. Plathow, C. Fink, A. Sandner, S. Ley, M. Puderbach, M. Eichinger, A. Schmähl, and H.-U. Kauczor, "Comparison of relative forced expiratory volume of one second with dynamic magnetic resonance imaging parameters in healthy subjects and patients with lung cancer," *Journal of magnetic resonance imaging*, vol. 21, no. 3, pp. 212–218, 2005.

[87] J. Blackall, S. Ahmad, M. Miquel, J. McClelland, D. Landau, and D. Hawkes, "MRI-based measurements of respiratory motion variability and assessment of imaging strategies for radiotherapy planning," *Physics in medicine and biology*, vol. 51, no. 17, p. 4147, 2006.

[88] J. Tokuda, M. Schmitt, Y. Sun, S. Patz, Y. Tang, C. E. Mountford, N. Hata, L. L. Wald, and H. Hatabu, "Lung motion and volume measurement by dynamic 3D MRI using a 128-channel receiver coil," *Academic radiology*, vol. 16, no. 1, pp. 22–27, 2009.

[89] S. G. Lingala, E. DiBella, G. Adluru, C. McGann, and M. Jacob, "Accelerating free breathing myocardial perfusion MRI using multi coil radial k- t SLR," *Physics in medicine and biology*, vol. 58, no. 20, p. 7309, 2013.

[90] A. Majumdar and R. K. Ward, "Causal dynamic MRI reconstruction via nuclear norm minimization," *Magnetic resonance imaging*, vol. 30, no. 10, pp. 1483–1494, 2012.

[91] A. Majumdar and R. K. Ward, "Exploiting rank deficiency and transform domain sparsity for MR image reconstruction," *Magnetic resonance imaging*, vol. 30, no. 1, pp. 9–18, 2012.

[92] M. Lustig, J. M. Santos, D. L. Donoho, and J. M. Pauly, "kt SPARSE: High frame rate dynamic MRI exploiting spatio-temporal sparsity," in *Proceedings of the 13th Annual Meeting of ISMRM, Seattle*, vol. 2420, 2006.

[93] H. Jung, J. Park, J. Yoo, and J. C. Ye, "Radial k-t FOCUSS for high-resolution cardiac cine MRI," *Magnetic Resonance in Medicine*, vol. 63, no. 1, pp. 68–78, 2010.

[94] D. Sun, S. Roth, and M. J. Black, "Secrets of optical flow estimation and their principles," in *Computer Vision and Pattern Recognition (CVPR), 2010 IEEE Conference on*. IEEE, 2010, pp. 2432–2439.

[95] W. N. Rom and S. B. Markowitz, *Environmental and occupational medicine*. Lippincott Williams & Wilkins, 2007.

[96] E. Dean, "Effect of body position on pulmonary function," *Physical Therapy*, vol. 65, no. 5, pp. 613–618, 1985.

[97] F. Moreno and H. A. Lyons, "Effect of body posture on lung volumes," *Journal of Applied physiology*, vol. 16, no. 1, pp. 27–29, 1961.